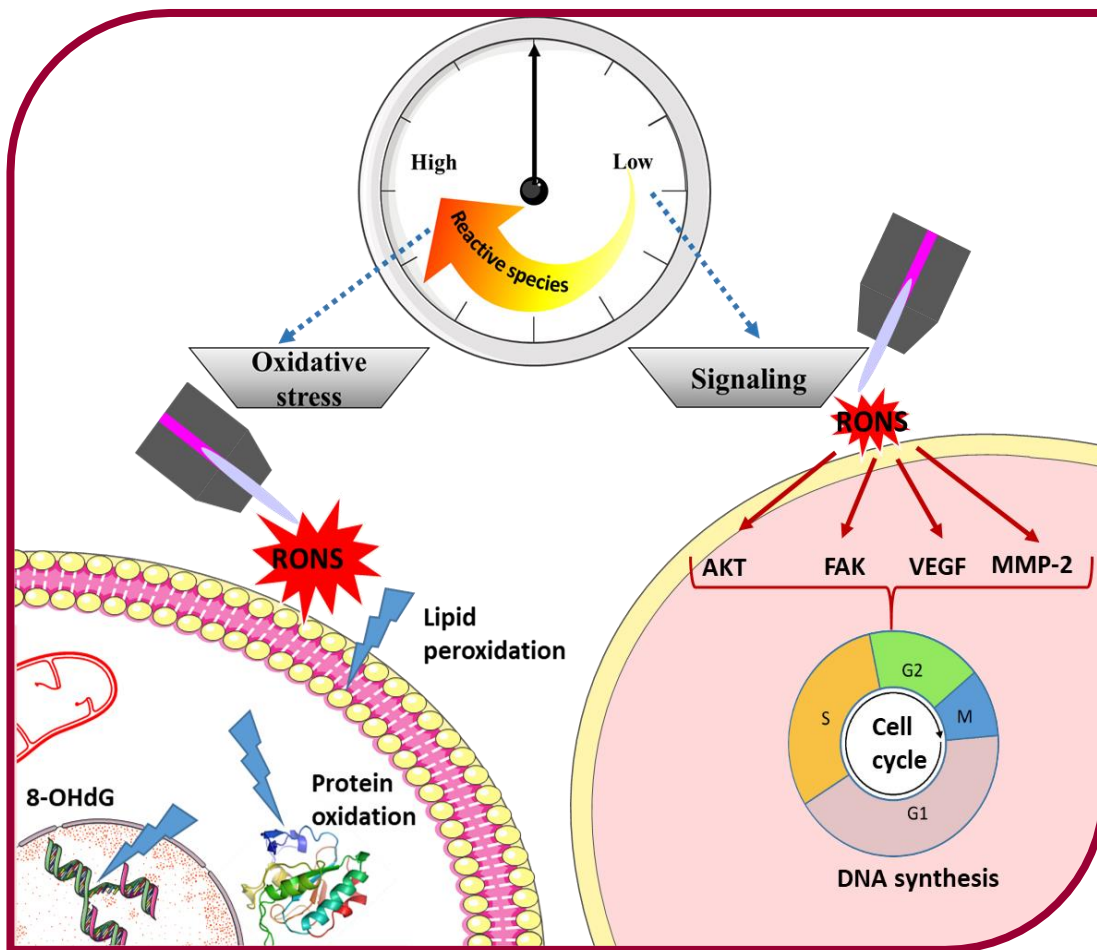


Dual action of reactive species as signal and stress agents in plasma medicine: Combined computational and experimental research

Priyanka Shaw



Promotor **prof. dr. Annemie Bogaerts**

Co-promotoren **prof. dr. Evelien Smits** | **dr. Angela Privat-Maldonado**

Proefschrift voorgedragen tot het behalen van de graad van doctor in de wetenschappen: chemie
Faculteit Wetenschappen | Antwerpen, 2021



**Universiteit
Antwerpen**



Faculteit Wetenschappen
Departement Chemie

Dual action of reactive species as signal and stress agents in plasma medicine: Combined computational and experimental research

Duale werking van reactieve deeltjes als signaal- en stress-agentia in plasmageneeskunde: Gecombineerd computationeel en experimenteel onderzoek

Proefschrift voorgelegd tot het behalen van de graad doctor in de wetenschappen: chemie aan de Universiteit Antwerpen te verdedigen door

Priyanka Shaw

Supervisor: Prof. Dr. Annemie Bogaerts

Co-supervisors: Prof. Dr. Evelien Smits & Dr. Angela Privat-Maldonado

Antwerpen 2021

MEMBERS OF THE JURY

SUPERVISOR:

Prof. Dr. Annemie Bogaerts
University of Antwerp

CO-SUPERVISORS:

Prof. Dr. Evelien Smits
University of Antwerp

Dr. Angela Privat-Maldonado
University of Antwerp

JURY:

Prof. Dr. Erik Neyts
University of Antwerp

Prof. Dr. Vera Meynen
University of Antwerp

Prof. Dr. Wim Vanden Berghe
University of Antwerp

Prof. Dr. Rodrigo Maghdissian Cordeiro
Universidade Federal do ABC, Brazil

Table of contents

Table of contents	1
Acknowledgements	5
List of abbreviations.....	9

I. BACKGROUND

Chapter 1: General introduction	13
1.1 Introduction to reactive species and oxidative stress.....	15
1.3 What is plasma?.....	17
1.4 Types of plasma sources.....	19
1.5 Administration of plasma treatment: Direct vs indirect CAP treatment.....	22
1.6 Reactive species in plasma medicine.....	24
1.7 Aim of this work.....	29

II. TECHNIQUES

Chapter 2: Computational methodologies	33
2.1 Introduction	35
2.2 Computer simulation methods.....	36
2.2.1 Classical Molecular Dynamics	37
2.2.2 Umbrella sampling (US) simulations	42
2.2.3 Molecular Docking	44
Chapter 3: Cell culture models	51
3.1 Introduction	53
3.2 Comparison of 2D vs 3D cell cultures.....	53
3.3 Multicellular spheroid model.....	55
3.4 Chick embryo chorioallantoic membrane (CAM) assay	58

III. RESUTS AND DISCUSSIONS

Chapter 4: Reactive species accelerate signaling in wound healing	63
4.1 Abstract.....	65
4.2 Introduction.....	65
4.3 Materials and Methods.....	67
4.4 Results.....	72
4.5 Conclusion	76
Chapter 5: Lipid peroxidation: reactive species enhance transdermal drug delivery by creating oxidative stress on lipids	77
5.1 Abstract.....	79
5.2 Introduction.....	79
5.3 Materials and Methods.....	80
5.4 Results and Discussion	88
5.5 Conclusion	100
Chapter 6: Protein oxidation: reactive species sensitize chemoresistant cells to lipid peroxidation-induced cell death	101
6.1 Abstract.....	103
6.2 Introduction.....	103
6.3 Materials and Methods.....	105
6.4. Results and discussion	112
6.5. Conclusion	125
Chapter 7: DNA damage: reactive species sensitize cancer cells to chemotherapy drugs due the formation of DNA oxidized compound	127
7.1 Abstract.....	129
7.2 Introduction.....	129
7.3 Materials and Methods.....	131
7.4. Results.....	138
7.5. Discussion.....	152
7.6. Conclusion	154

IV. SUMMARY

Chapter 8: Summary	157
Academic Curriculum vitae	169
References	175

Acknowledgements

Pursuing a PhD project in the PLASMANT and CORE research groups is both a challenging and enjoyable experience. It's just like climbing a high peak, step by step, accompanied with bitterness, hardships, frustration, encouragement, trust and with so many people's kind help. When I found myself at the top enjoying the beautiful scenery, I realized that it was, in fact, teamwork that got me there. Though it will not be enough to express my gratitude in words to all those people who helped me, I would still like to give my many, many thanks to all these people.

Firstly, I would like to give my sincere thanks to my honorific supervisor, **Prof. Dr. Annemie Bogaerts**, who accepted me as a PhD student. Thereafter, she offered me so much advice, patiently supervising me, and always guiding me in the right direction. I have learned a lot from her and from our biweekly meetings. She has been actively interested in my work and has always been available to advise me. I am very grateful for her patience, motivation, enthusiasm, and immense knowledge and experience, all together, a great mentor.

I especially want to thank my co-supervisor, **Prof. Dr. Evelien Smits** whose support and guidance made my thesis possible. I am very much grateful to **Dr. Angela Privat-Maldonado**, who helped me a lot to learn the three-dimensional tissue culture techniques for my research work and provided many tips to run experiments as an expert scientist. This PhD certainly was one of the most difficult things I have done in my life, but I can imagine that supervising me as a PhD student was not the easiest thing either. Thank you very much for all the guidance and effort during this work. I also want to thank **Late Prof. Dr. Sylvia Dewilde** and **Prof. Dr. Wim Vanden Berghe** from the Proteinchemistry, Proteomics & Epigenetic Signalling (PPES) laboratory for their valuable discussions and providing me the facilities for the experimental work.

I would like to say thank you to **Dr. Naresh Kumar** without whom I would not have started my research career. He offered me so much advice, patiently supervising me, and always guiding me in the right way for both my research and my life. He is the best person of my life and he has given me excellent suggestions for my research papers

and taught me several *in vitro* techniques. I was very happy to work with him and I had very exciting memories in both my personal as well as my professional life. **Dr. Maksudbek Yusupov** was not only the postdoc in our group, but also a very good friend that helped me with Molecular Dynamics simulations. He was like a big brother during my time in Belgium. I would also like to thank PhD student **Kenneth Goossens** from Medicinal Chemistry (UAMC) for helping me with the QM/MM calculations. I also want to thank **Dr. Charlotta Bengtson** for sharing her review material with us and spending quality time with me. Although I never got the chance to work under the supervision of **Prof. Dr. Erik Neyts**, I would like to thank him for giving me valuable suggestions during our group meetings as well as during the evaluation of my PhD. My sincere gratitude also passes to **Christophe Hermans**, who taught me immunohistochemistry and shared reagents and antibodies with me when needed. I also have to say a special word of thanks to **Prof. Dr. Eun Ha Choi**, my Master's degree mentor, long-time collaborator, and dear **Prof. Dr. Ihn Han** from the PBRC, Republic of Korea. Thank you so much for our fruitful collaborations. Of course, it is not possible to finish this study without the help of our technical and administration **Luc, Karel, Karen, Fabiana, Christine, and Ingrid**.

My time in the PLASMANT and CORE research groups was made enjoyable in large part due to the many friends. I am grateful for the time spent together, for my backpacking friends and our memorable trips to conferences and other beautiful places. I would like to thank Ph.D students **Joey De Backer and Emilie Logie** (PPES). They helped me a lot in my research work. Many thanks to all students and post-doc in PLASMANT and CORE who assisted me along the way, especially **Jamoliddin, Eline, Hanne, Ruben, Abraham, Elise, Pepijn, Rani, Sara, Elisabeth, Bart, Kristof, Claudia, Eduardo, Yannick, Yury, Hamid, Kevin, Parisa, Bjorn, Gregory, Colin, Ivan, Joachim, Joshua, Roel, Sean, Senne, Fanny, Edgar, Robin, Jinthe, Jorrit, Elly, Christophe, Celine, Delphine, Hannah, Tal, Astrid, Hasan, Andreas, Ho Wa, Maxim, Maxime**, and all the newest members of our group. I enjoyed so much the company of all the members of PLASMANT and CORE and I will miss you guys very much. I cherish the good memories created during this time.

Lastly, I would like to thank my family for all their love and encouragement. For my parents who raised me with a love of science and supported me in all my pursuits. And I especially thank my mom, dad, sisters and brothers. My hard-working parents have involved their best effort for better life and provided unconditional love and care. I love them so much and I would not have made it this far without them. Special love to the newest addition to my family, my son **Sourya Shah**, and now that he is exactly 6 years old, he is staying nearly 8000 km away from me. His cute smiling face bolsters me to complete this PhD thesis. The best outcome from these past eight years is finding my best friend, soulmate, and husband **Dr. Naresh Kumar**, who is out there for me. There are no words to convey how much I love him. He has been a true and great supporter and has unconditionally loved me during my good and bad times. I am so thankful and faithful to him for his support during the final stages of this PhD course.

Hartelijk bedankt voor uw ontelbare momenten van hulp en vriendelijke ondersteuning!

Priyanka Shaw

University of Antwerp
2021

List of abbreviations

ADT	AutoDock Tools
ARG	Arginine
ATCC	American Type Culture Collection
ATP	Adenosine triphosphate
BSA	Bovine serum albumin
BTK	Bruton's tyrosine kinase
CAM	Chick chorioallantoic membrane
CAP	Cold atmospheric plasma
CHARMM	Chemistry at Harvard Macromolecular Mechanics
COM	Center-of-mass
CPU	Central processing unit
CYS	Cysteine
DAB	3,3'-diaminobenzidine
DAPI	4',6-diamidino-2-phenylindole
DBD	Dielectric barrier discharges
H2DCFDA	2',7'-dichlorodihydrofluorescein diacetate
DFO	Deferoxamine
DMEM	Dulbecco's Modified Eagle Medium
DMSO	Dimethyl sulphoxide
DNA	Deoxyribonucleic acid
ECM	Extracellular matrix
ELISA	Enzyme-linked immunoassay
ESI	Electrospray ionization
FAK	Focal adhesion kinase
FBS	Fetal Bovine Serum
FEP	Free energy profile

GBM	Glioblastoma multiforme
GFP	Green fluorescent protein
GPF	Grid parameter file
GPX4	Glutathione peroxidase 4
GROMACS	GRONingen MACHine for Chemical Simulations
GSH	Glutathione
GSSG	Glutathione disulfide
HGF	Human gingival fibroblasts
HMOX	Heme Oxygenase 1
IACUC	Institutional Animal Care and Use Committee
IBR	Ibrutinib
LPM	Litres per minute
LTE	Local thermal equilibrium
LYS	Lysine
MDA	Malondialdehyde
MEL	Melittin
MET	Methionine
MMP	Matrix metalloproteinase
MTT	3-(4,5-dimethylthiazol-2yl)-2,5-diphenyltetrazolium bromide
NAC	N-Acetyl-L-cysteine
NADPH	Nicotinamide adenine dinucleotide phosphate
NOS	Nitric oxide synthase
NOX	NADPH oxidases
PBC	Periodic boundary condition
PBS	Phosphate buffered saline
PDAC	Pancreatic ductal adenocarcinoma
PDB	Protein Data Bank
PLB	Phospholipids bilayer

PME	Particle mesh Ewald
POPC	Palmitoyl-oleoyl-phosphatidylcholine
PTL	Plasma-treated liquids
PTM	Post-translational modifications
PTW	Plasma-treated water
PUFA	Polyunsaturated fatty acids
RMSD	Root mean square deviation
RMSF	Root mean square fluctuations
RNS	Reactive nitrogen species
RONS	Reactive oxygen and nitrogen species
ROS	Reactive oxygen species
RPMI	Roswell Park Memorial Institute
SASA	Solvent accessible surface area
SEM	Standard error of the mean
SOD	Superoxide dismutase
SPC	Simple point charge
TBA	Thiobarbituric acid
TMZ	Temozolomide
ULA	Ultra-low attachment
V_{RMS}	Root mean square of voltage
WHAM	Weighted histogram analysis method

Chapter 1: General introduction

Adapted from:

Priyanka Shaw, Naresh Kumar, Maxime Sahun, Angela Privat-Maldonado, Evelien Smits, Annemie Bogaerts, Targeting the keepers of redox balance: key for oxidative stress-inducing therapies. (*In preparation*)

1.1 Introduction to reactive species and oxidative stress

Reactive oxygen and nitrogen species (RONS) are very important intracellular messengers⁴ and can modulate a wide range of mechanisms within the biological system, including various disease pathogenesises^{5,6}. In mammalian cells, RONS are mainly generated in mitochondria when oxygen is reduced along the electron transport chain during aerobic respiration, or by oxidoreductase enzymes and metal-catalyzed oxidation throughout the lifetime of the cell cycle⁷. RONS function as a double-edged sword in cells⁷ (Figure 1.1). Low levels of RONS play an important role in supporting cellular life cycles, such as proliferation and homeostasis. They act as cellular signaling messengers by reversibly oxidizing protein thiol groups, thereby modifying the protein structure and function. More importantly, RONS generation has long been recognized as one of the key factors that protect our body from invading organisms in disease-resistance, cell mediated immunity, and microbiocidal activity⁷.

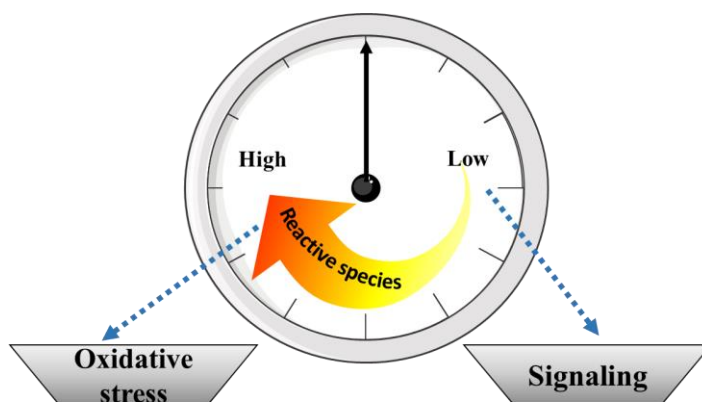


Figure 1.1: Low levels of reactive species play an important role in cell signaling whereas high levels of them induce oxidative stress.

Cells have a variety of defensive mechanisms to regulate the balance between the formation and elimination of RONS, and thus controlling oxidants at a moderate level for normal cellular functioning. However, the imbalance between RONS generation and detoxification could generate oxidative stress with high levels of RONS in the cell. This

would result in oxidative damage to cellular constituents (e.g., proteins, lipids, and DNA), apoptosis or necrosis, and probably the promotion of several diseased conditions such as diabetes mellitus, neurodegenerative disorders (Parkinson's disease-PD, Alzheimer's disease-AD and Multiple sclerosis-MS), cardiovascular diseases (atherosclerosis and hypertension), respiratory diseases (asthma), cataract development, rheumatoid arthritis and various types of cancers (colorectal, prostate, breast, lung, bladder cancers, etc.)^{8,9}.

From recent studies, it is established that RONS have the ability to play a crucial role in various therapies, specifically destroying cancer cells by means of enhanced oxidative stress through a variety of mechanisms^{9,10}. Cancer cells exhibit increased levels of intracellular ROS due to their hypermetabolism, compared to normal cells. An excess of ROS can damage biomembranes and propagate lipid peroxidation chain reactions, and eventually the other biocompartments can also be affected¹⁰. Thus, by modulating the level of intracellular RONS, we can make use of RONS for therapeutics, mainly due to the production and degradation of RONS by external or internal sources (see Figure 1.2). It is very important to analyse and control the level of RONS required to instigate the desired effect.

1.2 Source of reactive species

Reactive oxygen species (ROS) and reactive nitrogen species (RNS) can be derived from both endogenous and exogenous sources. Endogenous free radicals are generated during immune cell activation, inflammation, mental stress, excessive exercise, ischemia, infection, cancer, and aging, among others. Exogenous RONS result from air and water pollution, cigarette smoke, alcohol, heavy or transition metals (Cd, Hg, Pb, Fe, As), certain drugs (cyclosporine, tacrolimus, gentamycin, bleomycin), industrial solvents, cooking (smoked meat, used oil, fat), and radiation¹¹⁻¹⁴ (see Figure 1.2). After penetration into the body by different routes, these exogenous compounds are decomposed or metabolized into free radicals. These free radicals can cause the oxidation of molecules such as nucleic acids, lipids, and proteins; thereby altering the normal redox status and leading to increased oxidative stress.

An antioxidant is a species/substance that either prevents oxidant formation or scavenges oxidants, thereby forming less damaging or innocuous species and reducing oxidative stress. The most important free radicals produced during metabolic reactions are radicals derived from oxygen, such as hydroxyl (OH^\bullet), superoxide anions ($\text{O}_2^{\bullet-}$), peroxynitrite (ONOO^-), nitrite (NO_2^-), and nitric oxide (NO^\bullet). The other non-radical oxidant that can easily lead to free radicals in living organisms is hydrogen peroxide (H_2O_2). The oxidants are derived either from normal human metabolic processes or from external physical or chemical sources, as a consequence of enzymatic and non-enzymatic reactions.

It is possible to enhance the oxidative stress levels to target nucleic acids, lipids, and proteins using exogenous sources via RONS, the oxidative stress induced by these external sources has a biological effect in cells, as RONS can alter the mitochondrial membrane permeability, activate NADPH oxidase¹⁴, and further alter the overall cellular antioxidant status. Some of the current exogenous sources of RONS include chemical treatments such as drugs, and physical modalities such as ionizing radiation, photodynamic therapy, lasers, UV radiation, and cold atmospheric plasma.

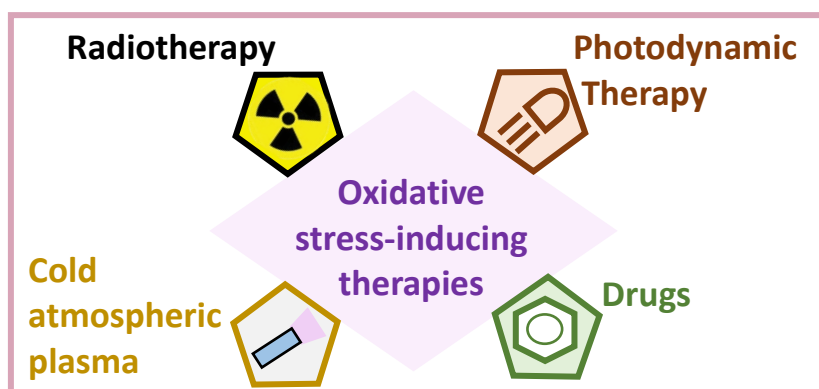


Figure 1.2: External sources of reactive oxygen and nitrogen species.

1.3 What is plasma?

Plasma, a (partially) ionized gas, is considered to be the fourth state of matter, following the more familiar states of solid, liquid and gas. It constitutes more than 99 % of the visible universe. It is created by applying high energy to a gas, leading to a

chemically reactive medium that consists of a large number of different species, such as electrons, atoms, molecules, radicals, excited species and ions, but also ultraviolet (UV), visible and infrared (IR) radiation, and an electromagnetic field, as shown in Figure 1.3.

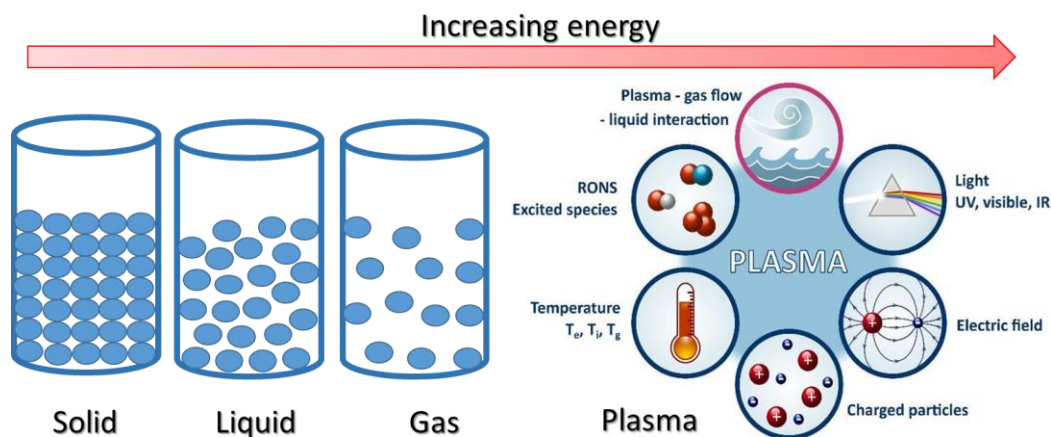


Figure 1.3: Generation of plasma upon increasing the energy of matter. Figure adapted from.^{1, 2}

Broadly speaking, plasmas can be classified as high and low temperature plasmas. High temperature plasma are, for instance, used for fusion research. Low temperature plasma is further subdivided into (i) thermal plasma, also called (quasi-) equilibrium plasma, which is in a local thermal equilibrium (LTE) state, and (ii) non-equilibrium or non-thermal plasma or cold plasma. Thermal plasmas are characterized by equilibrium or near equilibrium (in terms of energy, or temperature) between electrons, ions and neutrals. However, for most technological applications, the high temperature characteristic of thermal plasmas is neither required nor desired, and in some cases, it even becomes prohibitive. In such application areas, cold plasmas become more suited.

Non-thermal plasmas, or cold plasmas, refer to the plasmas where most of the coupled electrical energy is primarily channelled to the electrons, instead of heating the entire gas stream. Hence, the plasma ions and neutral components remain at or near room temperature. Because the ions and the neutrals remain relatively cold, this characteristic

allows its use on heat-sensitive materials, including polymers and biological tissues. Recently, cold atmospheric plasma (CAP), a rising new biomedical tool, has shown great potential as it can induce oxidative stress^{9,10,15}. Oxidative stress created by CAP-derived RONS induces a variety of biological effects, such as blood coagulation¹⁶, sterilization^{15,17}, wound healing¹⁷⁻²¹, cancer cell death^{9,10,22-25}, activation of immune cells^{26,27} and virus inactivation²⁸⁻³⁰.

1.4 Types of plasma sources

Recently, a wide range of different CAP sources has been developed for the use of biomedical applications. CAP sources are used in various areas of medicine, such as biological decontamination (i.e., the decomposition or removal of bacteria, spores, fungi, viruses, endotoxins and harmful proteins such as prions) and therapeutic applications (i.e., treatment of skin diseases, wound healing, cancer treatment, etc). Different types of CAP sources have been developed in various laboratories and some of them are currently available in the market for wound healing and bacterial decontamination. Some of these devices are the kINPen IND, kINPen MED (Neoplas GmbH, Germany)^{31,32}, PlasmaDerm (Cinogy GmbH)^{33,34}, SteriPlas (AdTec Ltd., Japan)^{35,36}, Plasma One (Medical Systems GmbH, Germany). CAP sources can be divided mainly into two different types: (i) Cold atmospheric plasma jets (or simply plasma jets) and (ii) Dielectric barrier discharges (DBD)

(i) Cold atmospheric plasma jets

The schematic diagram of a plasma jet source is illustrated in Figure 1.4a. In a plasma jet, a feed gas (working gas) is led between two electrodes, which are usually separated by a few millimetres in distance, depending on the size of the electrodes (e.g., the electrodes can be in any shape, such as hollow needle, ring, etc.). The voltage applied on the high voltage (HV) electrodes will accelerate the electrons in the discharge gap, which leads to ionization of the working gas and hence, it generates plasma. After passing through the discharge zone (inside the source), the generated plasma is transported out of the source into the surrounding atmosphere by (a) the flow rate of the working gas and (b) the propagation of the ionization front.

The object to be treated is thereby placed at a certain distance from the tip of the plasma jet (so-called nozzle), with typical treatment distances in the range of millimetres to centimetres. The working gases are usually noble gases, such as helium (e.g., the COST jet)³⁷, argon (e.g., the kINPen IND)^{19,31,32}, or a mixture of different gases like air, nitrogen or oxygen mixed with noble gases.

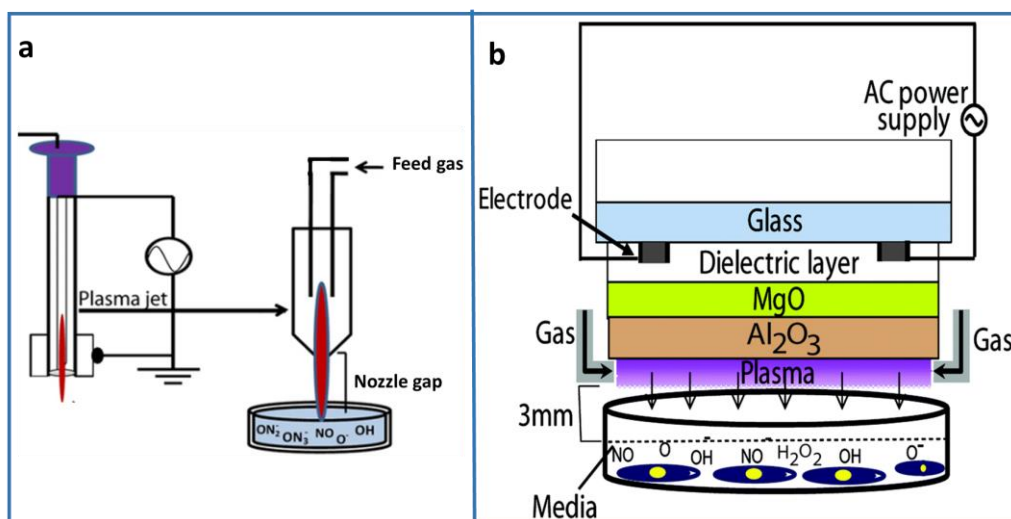


Figure 1.4: Schematic diagram of plasma sources: (a) Plasma jet (adapted from ¹⁶) and (b) DBD ²⁴.

(ii) Dielectric barrier discharges (DBD)

In DBD plasma sources (Figure 1.4b), two parallel electrodes are separated by an isolating layer (i.e., dielectric material) and the substrate to be treated is placed underneath the powered electrode. The use of an isolating layer in between the gap of the two electrodes limits the discharge current and avoids formation of an arc. The electron density generated by a DBD is higher than that of a plasma jet³⁸ by 2 to 3 orders of magnitude. The discharge gap of DBD sources also varies between 0.1 to 10 mm, depending on the geometry of DBD sources, such as in the sliding discharge³⁹, microcavity plasma array^{40,41}, capillary plasma electrode discharge⁴², and piezoelectric transformer⁴³. Both plasma configurations have advantages and disadvantages that are listed in Table 1.

Table 1: Advantages and disadvantages of plasma jet vs DBD.

Plasma sources	Advantages	Disadvantages
Plasma Jet	<ul style="list-style-type: none"> • Suitable for spot-like targeted treatments • Can treat very narrow substrates • Light-weight and compact device • Due to high etch rate, it can remove microorganisms from surfaces • The operational parameters are tuneable to modulate ROS production • Feeding gas helps the plasma propagate outside the device • The composition of ROS is less dependent on the local environmental conditions, unlike the DBD 	<ul style="list-style-type: none"> • Not ideal for large surface areas
DBD	<ul style="list-style-type: none"> • Capable to cover a larger surface area • Plasma discharges in ambient air • Expensive noble gases not required 	<ul style="list-style-type: none"> • HV electrode and target tissue must be close to each other • Difficult to reach a small area inside the human body • Reactive species highly depend on local conditions as it discharges on the ambient air

		<ul style="list-style-type: none"> • Less acceptable to the biomedical applications due to its bulky size
--	--	--

1.5 Administration of plasma treatment: Direct vs indirect CAP treatment

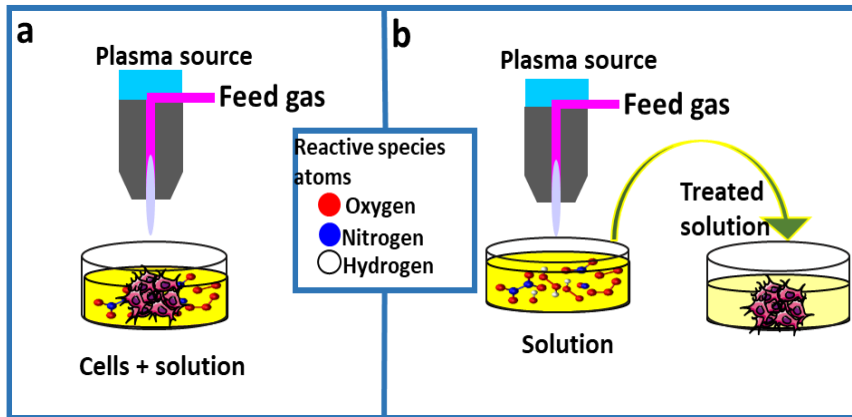


Figure 1.5: Schematic illustration for the use of CAP as (a) Direct treatment, and (b) Indirect treatment.

Generally, there are two ways to administer CAP treatments in biomedicine (Figure 1.5). One method is the direct CAP treatment in which the substrate is treated directly by CAP. All the plasma components, such as electrons, atoms, molecules, radicals, excited species and ions, as well as (UV, visible, IR) radiation and electromagnetic fields, will have the chance to affect the cells in some way. In *in vitro*, the cells are covered with either cell culture media or other biological solutions (e.g. deionized water⁴⁴, buffer solutions^{9,10}, ringer's lactate^{45,46}). However, in *in vivo* it can be used directly (where there is no liquid), like for wound healing. The presence of a liquid solution facilitates the generation of other type of long-lived species when the plasma interacts with the liquid surface^{10,47}. The long-lived species H_2O_2 , NO_2^- , NO_3^- , and $ONOO^-$, together with other components of plasma, have been demonstrated to be the key factors to inhibit tumor growth in most cases¹⁰. However, the chemistry of reactive species becomes more complex when they interact with a liquid solution. This is the reason why it is difficult to understand why there are different cellular responses to

different solutions treated with the same device. The biochemical pathways involved need to be better understood.

The indirect CAP treatment is performed by treating solutions with CAP (such as cell culture media, deionized water⁴⁴, buffer solutions^{9,10}, ringer's lactate^{45,46}), where ROS are delivered from plasma and induce the formation of secondary RONS in the liquid. The main effect of CAP-treated solutions is mediated by the long-lived reactive species present (discussed in [Chapter 7](#)) and the other products formed after the reaction of CAP and the components of the original solution. The important feature of CAP-treated solutions (i.e., indirect treatment) is that they can be stored under certain conditions over a long time⁴⁸. This unique feature of indirect treatment allows CAP to be used as a pharmacological method. CAP-treated solutions possess multiple advantages over direct treatment, but also some drawbacks that are discussed in Table 2.

Table 2: Advantages and disadvantages of direct treatment over indirect CAP treatment.

Method	Advantages	Disadvantages
Direct	<ul style="list-style-type: none"> • Applicable for surface treatments • More cytotoxic than the indirect CAP treatment • Contains both long-lived and short-lived species along with other components of CAP 	<ul style="list-style-type: none"> • ROS cannot be stored
Indirect	<ul style="list-style-type: none"> • Can be stored • Can be injected into a patient • Can reach distant targets • Exact composition of ROS before administration can be calculated 	<ul style="list-style-type: none"> • It contains only long-lived species • Less effective than direct treatments

1.6 Reactive species in plasma medicine

CAP devices are effective in producing large fluxes of reactive plasma species and energetic charged particles at low gas temperature. In the past two decades, CAP has made a revolutionary appearance. The versatility of plasma interactions with various surfaces was the inspiration for a completely new application that is plasma medicine. Plasma can affect bacterial and mammalian cells without inflicting thermal damage to nearby objects in many fields of medicine, such as sterilization^{15,25}, treatment of mammalian and cancerous cells^{9,10}, blood coagulation¹⁶, wound healing^{17,20,21} and dental treatments⁴⁹⁻⁵¹.

(i) Decontamination of infectious agents

CAP-derived RONS inactivate microorganisms including spores, gram-negative bacteria, gram-positive bacteria, biofilm-forming microorganisms, yeast, mould, mycobacterium, and viruses^{15,28-30}. Significantly, the bactericidal ability of plasmas has been comprehensively established against some of the deadliest or/and most resistant microorganisms such as *Bacillus subtilis*⁵², *Escherichia coli*⁵² (K12 and O157), *Staphylococcus aureus*¹⁵, and *Candida albicans*⁵³. These data highlight a real and significant opportunity for plasmas to be developed as a medical decontamination technology of surgical instruments, medical devices, and hospital wards (see Figure 1.6¹²). Medical contamination occurs not only by microorganisms but also by biomolecules such as proteins, DNA, and lipids. The obvious example is the contamination of the mis-folded prion proteins, widely regarded as the etiologic agent of spongiform neurodegenerative pathologies such as bovine spongiform encephalopathy, scrapie, and Creutzfeldt-Jakob diseases⁵⁴. Prion proteins are resistant to all current sterilization strategies including autoclaving, ionizing radiation, ethylene oxide, and formaldehyde⁵⁵, and as a result have forced the unsustainably expensive option of single-use surgical instruments. Recent studies suggest that plasmas are also capable of prion protein destruction^{56,57}.

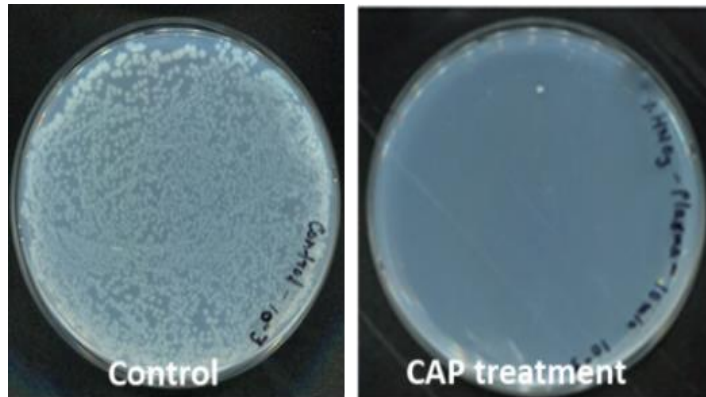


Figure 1.6: Colony of E. coli inactivation after plasma treatment compared to control (untreated) (Figure adapted from¹²).

(ii) Wound healing

Wound healing is an important issue in medicine. CAP is used in particular in wound surgery where CAP-derived RONS allow achieving cell differentiation and proliferation without any thermal effects. CAP-derived RONS are also crucial in trauma wound processes, as they can modulate the activity of endothelial nitric oxide synthase (eNOS)⁵⁸. The activity of eNOS is substantially increased during the inflammatory and proliferative phases of the healing process of trauma wounds, burn wound tissues, bone fracture site tissues, and others. Activation of eNOS was also discovered in the cultivation of wound fibroblasts. Macrophage activation in wounds, cytokine synthesis and proliferation of fibroblasts, epithelization, and wound healing processes are all linked with the activity levels of eNOS⁵⁵. Exogenous delivery of CAP-derived NO donors to the wound promotes and speeds up healing processes in animals with complicated wounds and in animals with inhibited eNOS⁵⁸. As CAP provides relatively high NO concentrations, it has a significant therapeutic effect in wound healing and tissue regeneration^{59,60}. It is reported that the KINPen MED¹⁹ and other devices are used nowadays for wound healing of patients with positive results.

In silico studies (Chapter 4) have revealed that CAP can modify the structure and activity of essential proteins involved in wound healing. The oxidation of the highly reactive amino acids, Cysteine and Methionine, by CAP leads to conformational changes and a higher structural flexibility of the focal adhesion kinase protein (FAK), see Figure 1.7. FAK is a non-receptor tyrosine kinase that provides signaling and is involved in the regulation of turnover of adhesion sites, a process that is crucial in the control of cell migration or proliferation.

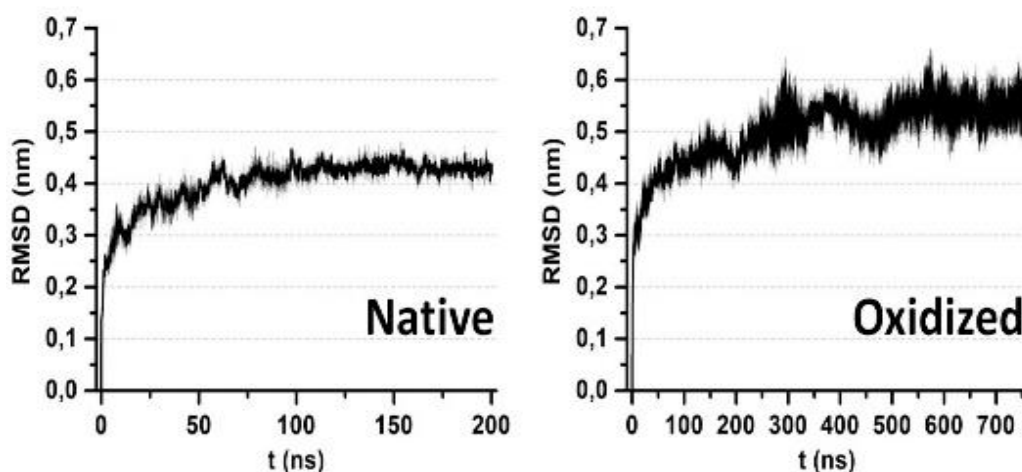


Figure 1.7 Average root mean square deviation (RMSDs) of the alpha carbons of the native and oxidized kinase domain (KD) of FAK.

(iii) Drug delivery

Drug delivery means to transfer pharmaceutical compounds to the cell interior by passing the cell membrane barrier. Drug delivery is essential for the treatment of certain pathologies such as cancer. However, it is known that patients with different types of cancer can develop resistance to drug treatment. *In silico* studies of CAP-induced oxidation of the phospholipid bilayer (PLB) in cell membranes demonstrated that cell membranes with higher fractions of cholesterol (i.e., typical for normal cells) were protected from pore formation. In contrast, when lower concentrations of cholesterol were present (i.e., typical for most cancer cells), the cell membrane was more vulnerable to oxidative stress and it favoured pore formation⁶¹. The pores generated in the cell

membrane facilitated the pass of plasma-generated ROS into the intracellular compartment^{62,63}, where they could exert further oxidative damage to cells. In addition, the lipid oxidation affects the integrity of the PLB and helps in the transport of drugs and peptides into the cell. This is the case of Melittin (MEL), an anticancer polypeptide which translocation across the PLB is improved after CAP treatment, as it decreases the free energy barrier (Figure 1.8; Chapter 5). Hence, the probability of MEL permeation to the cell interior increases, so that lower doses of MEL can provide cytotoxic effects. As cancer cells are more sensitive to oxidative stress than normal cells due to the high levels of steady-state RONS produced⁶⁴, anticancer treatments (such as the one described here) that increase the oxidative stress levels beyond the RONS threshold could aid to the elimination of cancer cells without damaging the normal cells⁶⁵. Overall, it indicates that the lipid oxidation helps in the penetration of any drug (as big as MEL peptide) to:

- (a) Disrupt the fluidity and integrity of the cell membrane.
- (b) Facilitate their access into the intracellular compartment.
- (c) Damage the intracellular components of cancer cells to induce cell death.

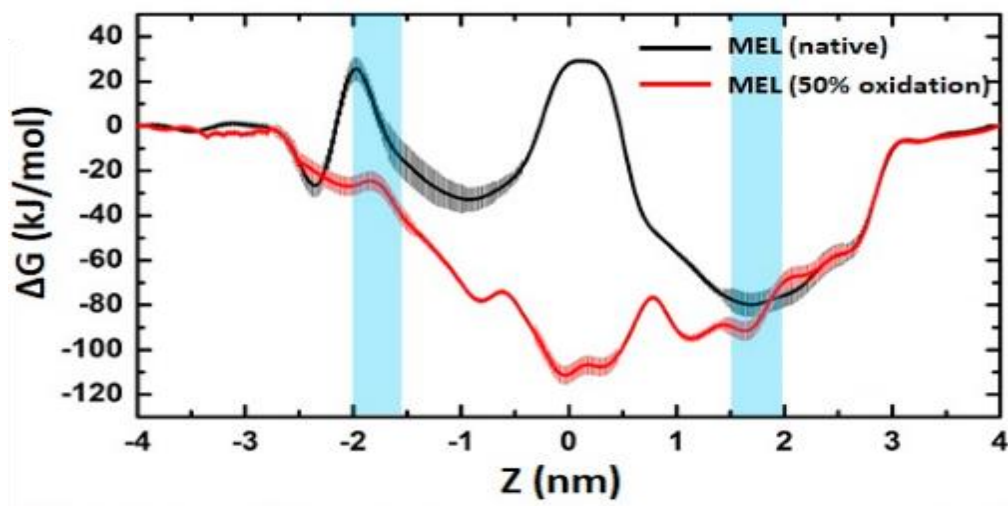


Figure 1.8 Penetration of drug (Melittin) is higher after lipid oxidation.

(iv) Cancer treatment

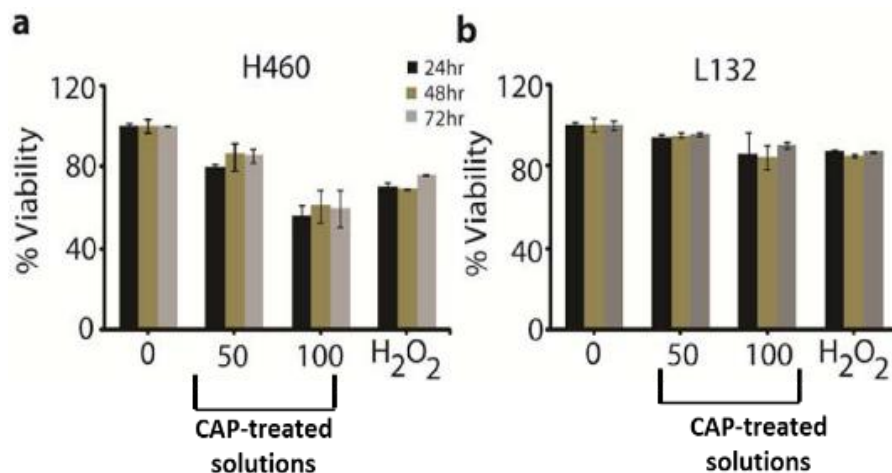


Figure 1.9 Reduction of the cell viability of (a) H460 lung cancer cells, and (b) L132 normal lung cells after treatment with 30 μM of H_2O_2 and CAP-treated solutions.

The selective elimination of cancerous cells has been a big challenge for the medical sciences⁶⁶. In spite of the presence of an innate antitumor barrier, cancer continues to be a leading cause of death. Improving selective cancer cell death is a big leap forward in cancer treatment^{67,68}. Still, there are some restrictions to induce selective apoptosis in cancer cells (Figure 1.9²⁵). The enhancement of RONS such as $\text{H}_2\text{O}_2/\text{OH}^\cdot$ is one of the efficient alternative biochemical treatments of cancer therapy^{59,69}. As explained above, CAP produces various RONS^{59,70}. The OH radicals are one of the most unstable ROS with a half-life of about 10^{-9} s⁷¹, indicating that they will quickly react with other species under most physiological conditions. By contrast, superoxide radicals carry a negative charge that restricts its membrane permeability to anion channels. It can be easily converted into H_2O_2 and NO^\cdot that can readily pass-through membranes⁷¹⁻⁷⁵. H_2O_2 and NO^\cdot can alter the intracellular redox state which may lead to the elimination of cancer cells^{76,77}.

Apart from selective treatment of cancer cells, another major contributor to the poor clinical outcome of current cancer therapies is the prominent development of resistance to treatment, developed by the ability of cells to escape apoptosis. This has fueled the

search for therapeutic strategies targeting alternative (non-apoptotic) types of programmed cell death, such as necrosis/necroptosis or ferroptosis⁷⁸. Cancer cells exhibit an increased iron demand compared with normal, non-cancer cells to enable growth. This iron dependency can make cancer cells more vulnerable to iron-catalyzed necrosis, referred to as ferroptosis. CAP-generated RONS can be converted to H_2O_2 by superoxide dismutase (SOD) on the cell membrane. When H_2O_2 diffuses into the cell, it subsequently yields highly toxic OH radicals in the presence of reduced iron (Fe^{2+}) through the Fenton reaction (see Figure 1.10), which further increases the intracellular ROS pool. Further increase of ROS levels will progressively impair the antioxidant defense mechanisms (see Chapter 6 and 7) and cause ferroptotic cell death (Figure 1.10).

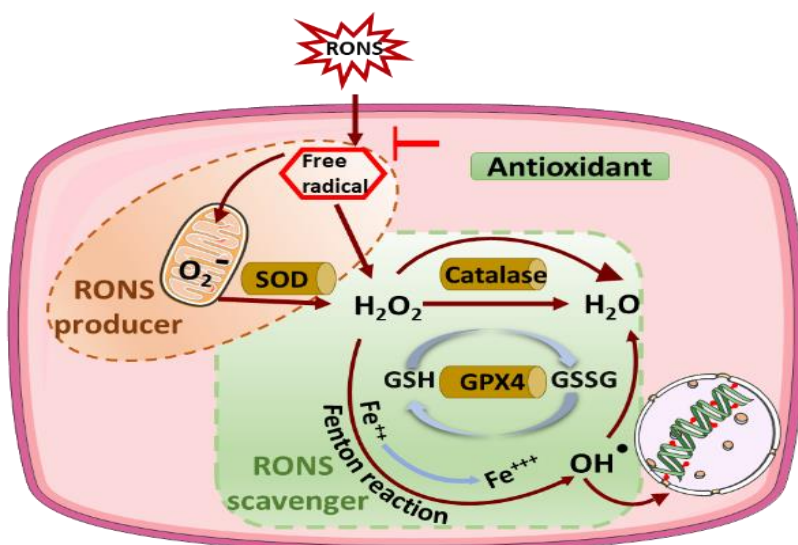


Figure 1.10 Ferroptotic cell death, a consequence of the Fenton reaction.

1.7 Aim of this work

Reactive species play an important role in maintaining the redox homeostasis in biological systems. These RONS have double-sidedness, which means that at short exposure times or low dosages they stimulate cell viability, proliferation, and migration, but a long exposure or a high dosage they induce cell senescence or apoptosis by oxidative damage to DNA, proteins, and lipids^{30,76}, see Figure 1.11. Hence, I hypothesize

that CAP can modulate the redox state of cells to induce a strong and effective oxidative stress-mediated cellular response. Overall, the primary objective of this research is to have a clear overview of the interaction of RONS with biomolecules (lipids, proteins and DNA, as shown in Figure 1.11) from the atomic scale to the macro scale, and their biological significance. Thus, complementary to experiments, I performed computer simulations to elucidate the underlying mechanism with nano-scale precision.

To test my hypothesis, in [Chapter 4](#), I investigated the treatment of human gingival fibroblasts (HGFs) with low doses of CAP-generated RONS. This treatment demonstrated that it can inhibit colony formation but does not induce cell death, induce the expression of metalloprotease proteins, induce extracellular matrix degradation, and promote cell migration, which could result in enhanced wound healing. Computer simulation indicates that the oxidized Kinase domain (KD) of focal adhesion kinase (FAK) becomes slightly more flexible than the native KD, which is due to the conformational changes in the protein. Thus, oxidation results in a slight increase in structural flexibility, thus affecting its stability. This in turn might affect the FERM-KD binding, thereby disrupting this interaction.

In contrast, at high concentrations, RONS can disrupt the cell membrane integrity and induce cancer cell death through oxidative stress-mediated pathways. In [Chapter 5](#), we discovered how oxidation of the cell membrane (lipid-peroxidation) can facilitate the access of a drug (Melittin) into cancer cells, and in this way, reduce the required therapeutic dose of MEL in A375 melanoma and MCF7 breast cancer cells (demonstrated using *in vitro*, *in ovo* and *in silico* approaches). Furthermore, in [Chapter 6](#), we studied how excessive lipid-oxidation in chemoresistant pancreatic cancer cells (PANC-1 and BXPC3) promotes ferroptotic cell death. This was due to the stimulation of the iron-dependent Fenton reaction by targeting a HMOX1-GPX4 specific signaling network. However, upon oxidative stress, cells protect themselves via a sophisticated intracellular antioxidant system that involves the regulation of glutathione/glutathione peroxidase 4 (lipid repair enzyme). Cancer cells exhibited increased levels of intracellular RONS due to their hyper metabolism, leading to high expression of anti-oxidant systems. In [Chapter 7](#), I therefore focus on the effect of reactive species on the intracellular anti-oxidant

system and corresponding DNA damages in both temozolomide-sensitive as well as temozolomide-resistant glioblastoma spheroids, in a 3-dimensional tumor model with a more complex tumor microenvironment than cell monolayers.

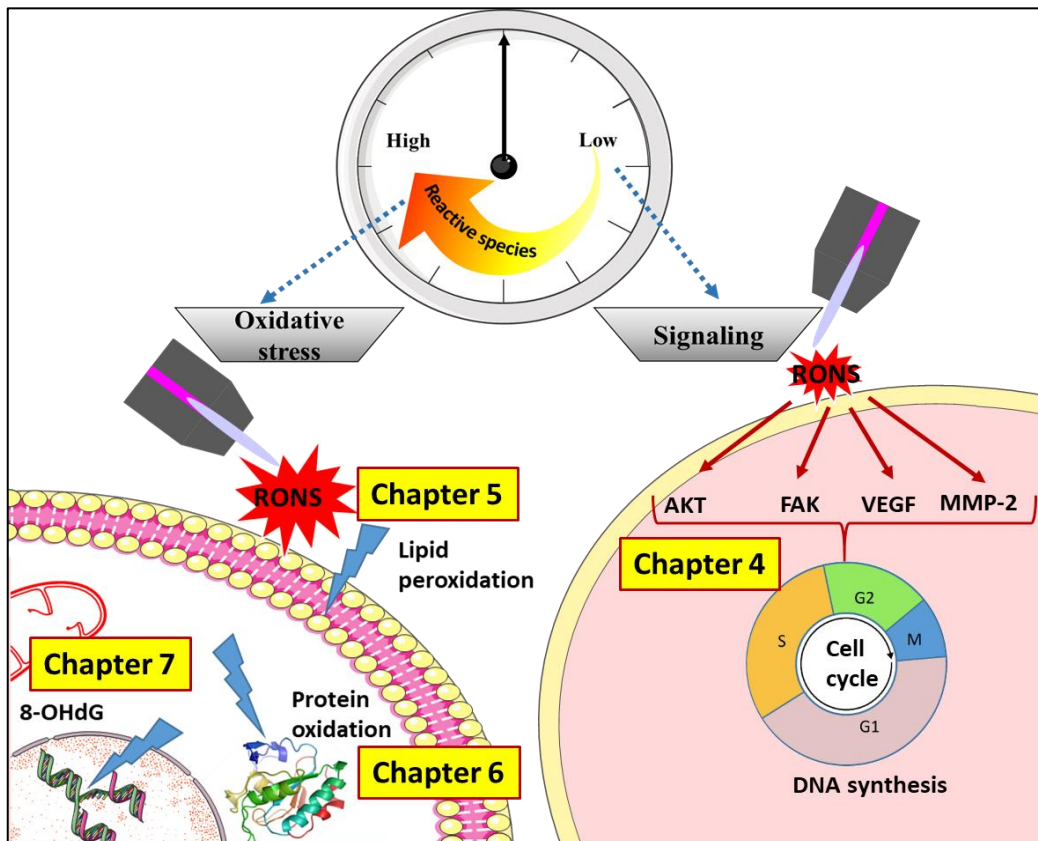


Figure 1.11 Overview of the outline of the thesis. Abbreviations: RONS, reactive oxygen and nitrogen species; G1, Gap 1; G2, Gap2; S, synthesis; M, Mitosis; VEGF, vascular endothelial growth factor; MMP-2, matrix metalloproteinase mTOR; FAK, focal-adhesion kinase; 8-OHdG, 8-hydroxydeoxyguanosine.

Chapter 2: Computational methodologies

2.1 Introduction

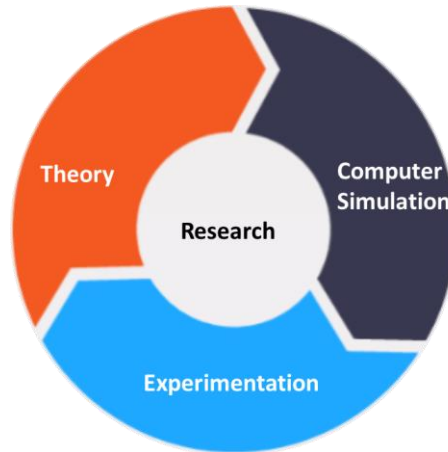


Figure 2.1 Computer simulations bridge a gap between theory and experiment.

Nowadays, computer simulations are a powerful technique to obtain insight in real systems into various research fields such as physics, chemistry, biology, engineering, etc. that might be difficult or impossible to obtain in real experiments. The specific advantage of computer simulations is that it has the ability to ‘bridge’ theory and experiment (Figure 2.1). It often allows comparison with real experiments, such as the ones mentioned in the previous [Chapter](#). Moreover, computer simulations are performed based on the experimental conditions and hence the obtained results can be compared directly with experimental observations. This makes computer simulation studies an important tool to understand the underlying mechanism of experimental data with nanoscale precision, and thereby, it can overcome the limitations of experiments. Nevertheless, it has to be noted that these simulation models are always an approximation (i.e., a subset of the actual situation). Hence, the conclusions drawn from the obtained computer simulations depend on the assumptions made in the development of the system or running the simulations. Therefore, it is important to combine both approaches for more in-depth studies.

Computer simulations are mainly used to understand the dynamic behaviour of systems and are quite useful to predict how the functioning of an entire system may be affected by altering individual components within that system. However, more advanced simulations, such as those that emulate dynamic patterns or the behaviour of

macromolecule systems (lipids, proteins or nucleic acids), are usually performed on powerful workstations or supercomputers (several CPUs are connected to achieve fastest high-performance systems with very large storage capacity). This, in turn, makes the computer simulations expensive. Additionally, at the atomic level, computer simulations are often limited with respect to time and length of the system. For a clear overview on computer simulations, some important features are listed in Table 2.1.

Table 2.1 Advantages and disadvantages of Computer simulations.

Advantages	Disadvantages
<ul style="list-style-type: none"> • Helps to explain the experimental data at nanoscale precision • Predicts the action of drugs • Avoid danger and loss of life • Cost-effective compared to experiments • Critical situations can be investigated without risk • Simulations can be explicitly slowed down to study behaviour of the system more closely • Waste can be removed, which is not possible in experiments 	<ul style="list-style-type: none"> • Need to use supercomputer for longer calculations • Thorough understanding is needed of all the factors involved in the system • Always an approximation of the real situation

2.2 Computer simulation methods

We have carefully chosen the type of computer simulation techniques in this thesis to provide fundamental or atomistic-level insight to my experimental data occurring on biomolecules in response to CAP-derived reactive species. A wide variety of computer simulation methods exist with its own specific advantages and limitations. Two main families of simulation methods can be identified in plasma medicine: Classical

Molecular Dynamics and Molecular Docking. In this PhD work, I applied both techniques, and they will be discussed in the following sections.

2.2.1 Classical Molecular Dynamics

Molecular Dynamics (MD) is the most widely used computer simulation technique to describe the interactions between particles (atoms and molecules) in biological systems. In MD simulations, the system always contains a fixed number of particles (atoms and molecules) and they interact to each other for a certain period under equilibrium conditions. The interaction between all atoms and the potential energy (U) of particles is computed based on the force fields. Therefore, a force field defines the force (F_i) acting on all particles ($i = 1, 2, 3, \dots, N$) by the following equation (Eq. 2.1):

$$F_i = -\nabla_{r_i} U, \text{ where } r_i \text{ is the position of the atoms} \quad (2.1)$$

The trajectories of the particles of the system are captured by using Newton's equation of motion (Eq. 2.2)

$$m_i \frac{d^2 r_i}{dt^2} = F_i \quad (2.2)$$

where m_i is the mass of the atoms at the corresponding time t

Each particle moves based on the above equation and a subsequent iteration of the integration is performed. In this thesis, I used the Verlet algorithm for the integration of Newton's equation of motion. Under the ergodic hypothesis, the MD simulations can be averaged to represent the thermodynamic properties of a system with macroscopic precision. Moreover, the choice of the algorithm determines the validity of the simulation results. Thus, it is crucial to carefully choose a system algorithm with the most suitable ensemble for equilibration, the best boundary conditions, and specific thermostat and barostat to use. This thermostat and barostat ensure the MD calculations to generate in a certain way for the statistical ensemble at a predefined temperature and pressure. The exact setup used in the MD simulations performed in this thesis can be found in [Chapters 4, 5 and 6](#). The simulation procedure is usually constructed as follows (Figure 2.2):

1. Initialize the system so that there will be zero total momentum
2. Compute the trajectories of each particle based on the force field used to describe the system
3. Integrate the Newton's equation of motion on each or group of particles
4. Repeat steps 2 and 3 for a certain period of time
5. Run the analysis based on the type of data needed to collect from the system



Figure 2.2: Workflow for MD calculations.

In this thesis, MD simulations are composed of only 10^2 - 10^5 atoms which is negligible compared with the number of atoms contained in a real case. This means the number of particles in the system is much smaller than the macroscopic material. However, to simulate a material of only 1 mole (6.022×10^{23} atoms) with the simplest interatomic potential, it would take 10 years. This inherent problem of MD simulations can be avoided by using boundary conditions. Thus, by applying specific periodic boundary conditions (PBC) during MD calculations (Figure 2.3), it is possible to calculate the macroscopic parameters of the system, while the system contains fewer particles. In other words, even though the size of the system is finite, it will be treated as

infinite after applying PBC. In PBC, the particles are enclosed in a pre-assigned box and copies of themselves surround the original box (see Figure 2.3). In this way, the atoms at the edge of the system can interact with the nearest one (with the image from the opposite side) while keeping the same velocity. Moreover, PBC does not have any influence on the course of the simulation and the trajectory of the particles in the main box is recorded for further analysis.

Furthermore, the choice of the force field used in MD calculations is crucial. In the past⁷⁹, many types of force fields have been developed and also verified against a certain set of molecules. Depending on the desired properties that need to be studied, the force field can be ‘reactive’ or ‘non-reactive’. In case of reactive force fields, molecular bonds can be broken or created during the simulation runs. Thus, a reactive force field is used to investigate the chemical reactions where the connectivity between each atom needs to be recalculated on every integration time step, which increases the computation load. On the other hand, in a non-reactive force field, molecular bonds cannot be broken or formed throughout the simulations, and thus the atomic connectivity remains the same. This means there is no need to recalculate the atomic connectivity at every time step and that is why non-reactive simulations are faster and better equipped to perform calculations with big system (an example of such system is discussed in [Chapter 4, 5 and 6](#)). However, non-reactive simulations cannot provide as much insight in the reaction chemistry as reactive calculations.

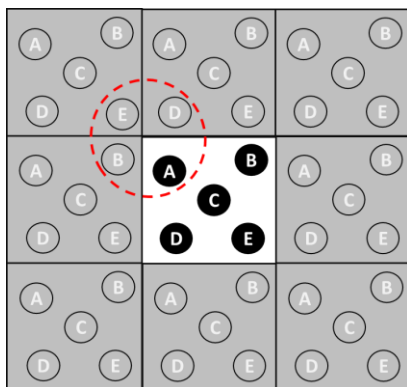


Figure 2.3: Periodic boundary condition of atom 'A' with its images.

For this thesis, I used only non-reactive force fields. In non-reactive simulations, the interatomic potential energy is the sum of bonded (U_B) and non-bonded (U_{N-B}) energy, as shown in Figure 2.4.⁸⁰⁻⁸². The bonded interaction potential (U_B) depends on the certain number of covalently bonded atoms such as bond stretching (U_l , in two atoms), bond angle (U_θ , in three atoms) and dihedral angle (U_w , in four atoms). The non-bonded interaction potential is further sub-divided into Lennard-Jones (U_{LJ}) and Coulombic interactions (U_C). Hence, from the above discussion, the total potential energy is defined by Eq. 2.3 and 2.4:

$$U = U_B + U_{N-B} \quad (2.3)$$

$$\therefore U = U_l + U_\theta + U_w + U_{LJ} + U_C \quad (2.4)$$

There exist different types of non-reactive force fields based on the level of detail at which individual particles are described. Either each atom is described separately, and this leads to the generation of 'all atom' force fields (such as Amber⁸³, CHARMM⁸⁴, or OPLS⁸⁵) or multiple atoms can be grouped into one particle, which are connected through pseudo-bonds. Further, based on the number of atoms used to create such a particle, 'united atom' and 'coarse-grained' force fields can be distinguished and they can handle a large system. These force fields typically group 3-4 or 12-15 atoms in each particle, respectively (Figure 2.5). Briefly, in case of 'united-atom' force fields, such as GROMOS⁸⁶, some typical atoms are grouped to make one particle. Usually, aliphatic hydrogens are combined with their respective carbon atoms to form one effective '-CH₂' particle and all heavy atoms are treated separately. Consequently, a 'united atom' force field reduces the total number of particles in a system and thereby, it also reduces the computational load. Another alternative to speed up the simulations is by making use of coarse-grained models where small groups of atoms (the number of atoms is more than in the 'united atom' force field) are treated as larger particles, enabling the access of longer time and length scales. We can say that the 'united atom' calculations are the lowest-level 'coarse grained' calculation. The difference mainly lies in the number of particles that is combined: in a 'united atom' force field, typically only the atoms in a methylene group or a methyl group are combined, whereas in a 'coarse grained' force field, entire functional groups or structural units are treated as a single particle. Further, this allows 'united atom'

force fields to handle a bigger system on a larger time scale (nanoseconds to even microseconds) unlike ‘all-atom’ force fields. However, it should be noted that the grouping of atoms into particles reduces the level of detailed insight of the system. Thus, it is very important to choose the force field carefully, and this decision must be based on the exact point of interest of the study.

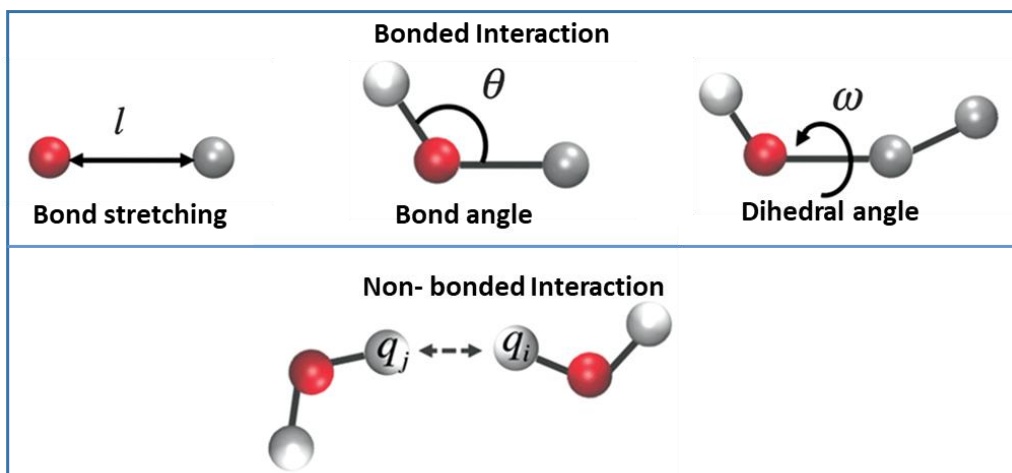
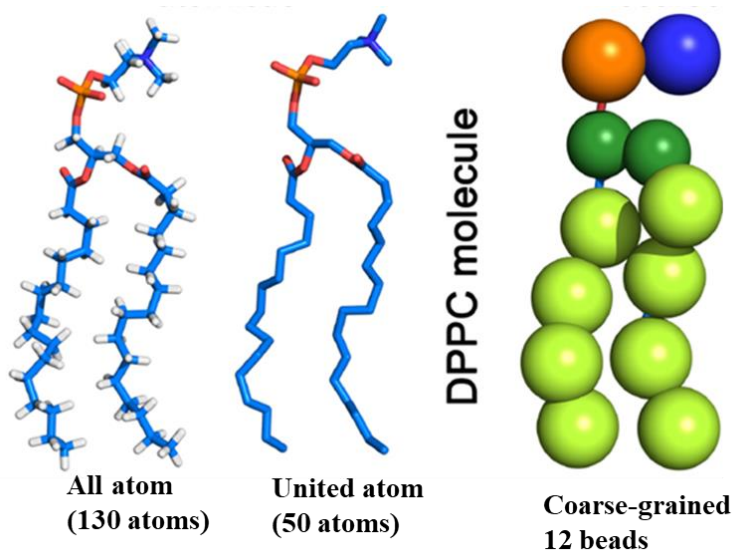


Figure 2.4: Illustration of interatomic parameters. Figure adapted from¹.

In this thesis, I used a ‘united atom’ force field (i.e., GROMOS (GRONingen MOlecular Simulation))⁸⁶ to investigate (i) the effect of CAP-derived oxidation on the stability and conformation of the catalytic kinase domain of Focal Adenosine Kinase (FAK) (in Chapter 4) by analysing the stability of protein structures; (ii) how lipid-oxidation increases the penetration of a chemical drug (Chapter 5) by calculating the free energy barrier (by Umbrella sampling) of penetration of this drug across the lipid bilayer; and (iii) how protein-oxidation causes conformational changes in the catalytic active pocket GPX4 (Chapter 6). Since in this thesis, the MD simulations are done only with non-reactive force field, the oxidation parameters are taken as an input of the system.



*Figure 2.5: Different representations of a DPPC (1,2-dipalmitoyl-*sn*-glycero-3-phosphocholine) lipid in an all atom, united atom or coarse-grained force field. Figure was adapted from³.*

2.2.2 Umbrella sampling (US) simulations

The calculation of free energy differences or dissociation free energy is one of the main challenges in the field of computational biology. Precisely, the free energy contains the entropy that is a measure for the available space, and to map the available space in a bigger system like for biomolecules is also quite challenging, and thus, extensive sampling is required. In this regard, US is one of the powerful computational techniques to calculate the free energy differences across the reaction coordinate (RC) in a system bigger than a few atoms. During US simulations, it is ensured that efficient sampling is performed across an entire RC by applying a bias potential. The sampling across the RC can be executed either in one simulation or in different simulations (windows) where the distributions overlap. The bias potential connects the energetically separated regions in phase space and gives rise to the name “umbrella sampling”. The mathematical description of how this bias potential is applied can be found elsewhere⁸⁷. US simulations calculate the FEP using the weighted histogram analysis method (WHAM).

In addition, US is widely employed to compute the interaction between protein-protein, protein-lipid, protein-drug, and drug-membrane under an external perturbation. These umbrella sampling windows run in independent simulations. Figure 2.6 illustrates these principles. The top image illustrates the pulling simulation, conducted to generate a series of windows along with the RC. These windows are extracted after the simulation is complete (dashed arrows in between the top and middle images). The middle image corresponds to the independent simulations conducted within each sampling window, with the center of mass of the free objects (Melittin in our case, Chapter 5) restrained in that window by an umbrella biasing potential. These series of windows are separated by a fixed distance between the considered molecules. The bottom images show the ideal result as a histogram of configurations, with neighbouring windows overlapping such that a continuous energy function can later be derived from these simulations.

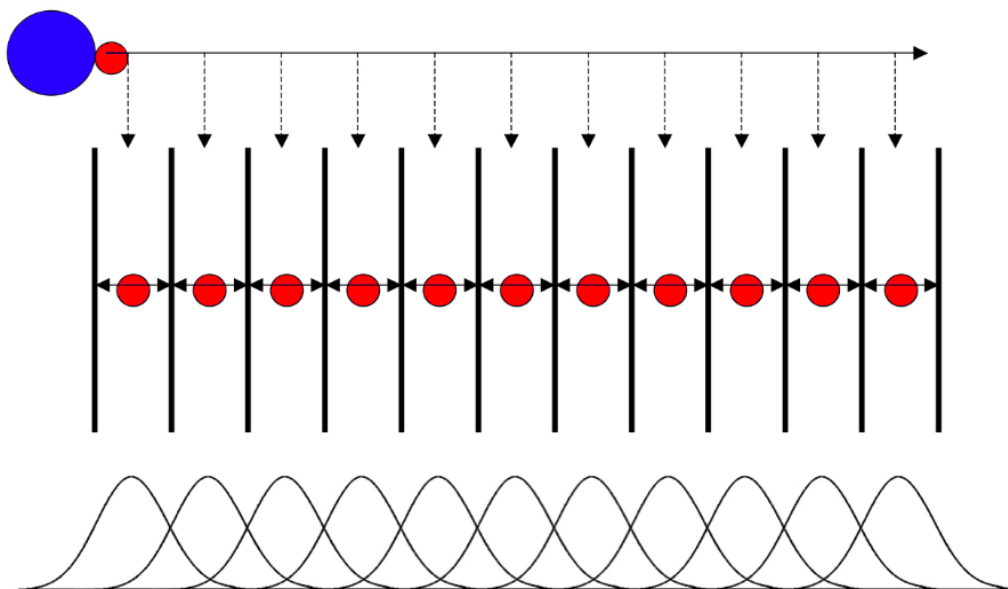


Figure 2.6: Illustration of the US simulation set-up. Figure was adapted from http://www.mdtutorials.com/gmx/umbrella/01_pdb2gmx.html

2.2.3 Molecular Docking

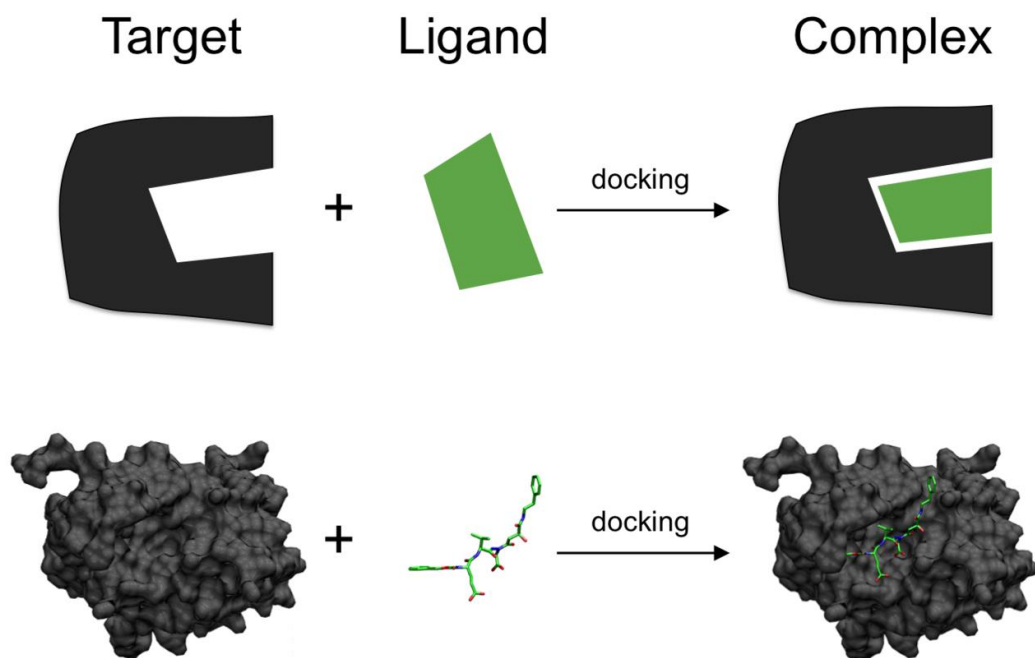


Figure 2.7: Schematic illustration of docking a small molecule ligand (green) to a protein target (black) producing a stable complex. Figure was adapted from Wikipedia.org

Molecular docking is a powerful tool in molecular modeling and computer-aided drug design. The goal of molecular docking is to predict the preferred orientation of one molecule (protein or nucleic acids) with another molecule (a ligand, e.g., drug) to form a stable complex structure. This is a very useful method in pharmacy, as it helps in the rational design of drugs that tightly bind to the targets, for example, affecting the cellular signal transduction. Molecular docking can be considered as a methodology of "lock and key", where the ligand (key) wants to find a correct orientation so that it can fit into the key hole of the lock (protein). Hence, molecular docking is an optimisation process to describe the 'best-fit' orientation of a drug to bind a specific protein of interest by adjusting their conformations, as shown in Figure 2.7. The process of adjusting the orientation between protein and ligand is finished once the free energy of the overall

system is minimized and this is approximated by the scoring function. The scoring function helps to discriminate putative correct binding conformations from non-binders based on the conformations created by the sampling engine. The higher scoring functions can be considered as a potential binding conformation of the ligands for further analysis.

Different types of molecular docking packages for protein-drug interaction have been developed, such as Autodock^{88,89}, Haddock⁹⁰, and Zdock^{91,92}. Each docking software has its own advantages or limitations, so which docking software is most suited will always depend on the exact point of interest of the study at hand. Indeed, before actually deciding a molecular docking simulation, one has to know how the ligand binds to the target. Recently, there has been a resurgence of interest in inhibitors (drugs) that bind covalently to their targets⁹³ (Figure 2.8). This type of drugs has very tight binding, allowing design of drugs with small molecular mass but with very high potency. As mentioned in the previous [Chapter](#), the problem with selectivity of therapy have been a concern for many diseases and that motivates the development of covalent inhibitors. However, only one third of the currently approved drugs act through covalent mechanisms. The major approach to reducing toxicity of chemotherapy drugs is to improve the selectivity of the drugs, by optimizing the non-covalent interactions with the protein-binding site.

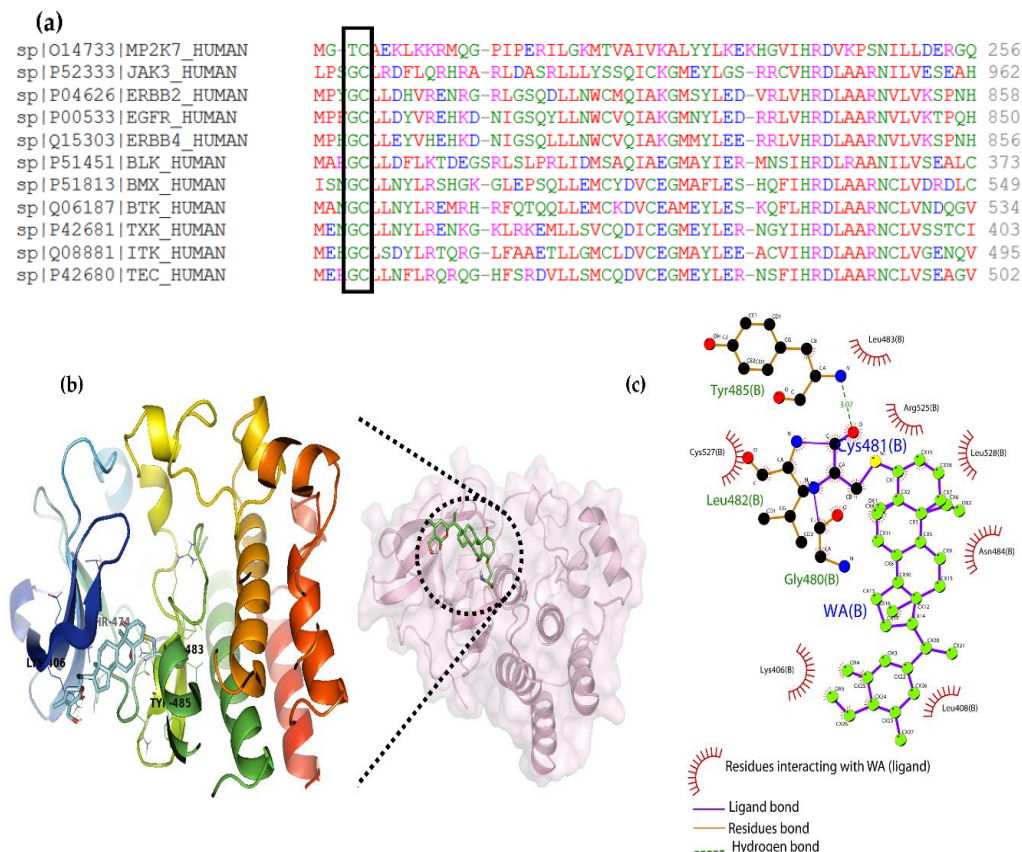


Figure 2.8: (a) Multiple sequence alignment of Hinge 6 domain type kinases. The conserved GC-motif between different orthologs is indicated. (b) Crystal structure of BTK (PDB id: 6TFP) in complex with WA (PubChem CID: 26537) covalently bound to Cys481. (c) Interaction between WA and BTK structure visualized using Ligplot² showing covalent bond formation of the C4-OH group of WA with the SH group of Cys481 from BTK.

Molecular covalent docking provides an effective computational way to evaluate the interaction of a trial covalent inhibitor (drug) with a target. Novel covalent kinase inhibitors, such as the clinically approved Bruton's tyrosine kinase (BTK), inhibitor ibrutinib (IBR) and the preclinical phytochemical withaferin A (WA), have, therefore, gained pharmaceutical interest. WA-induced cell death involves covalent cysteine targeting of Hinge-6 domain type tyrosine kinases of the kinase cysteinome classification, including inhibition of the hyperactivated BTK. For the covalent interaction between

BTK and WA, I performed flexible side chain Covalent docking (discussed below) to confirm that WA-induced cell death involves covalent cysteine. This was done by targeting the Hinge-6 domain type tyrosine kinases of BTK⁹⁴, as shown in Figure 2.8, using Autodock4 (v4.2.6, University of California, Berkeley, CA, USA). The obtained docking solutions were evaluated based on their scoring, and the generated poses were clustered based on the ligand's cluster ranks. Finally, the clusters were differentiated based on the covalent bond lengths and prime energies. Final docking results were visualized with LIGPLOT (v.4.5.3, University College London, UK)².

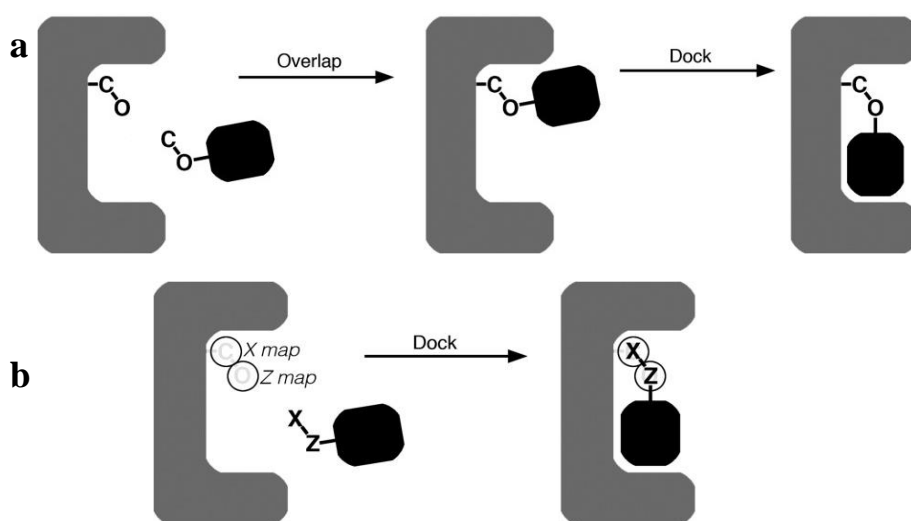


Figure 2.9: Covalent docking using auto dock: (a) Flexible side chain methods and (b) Two-point attractor (Figure is adapted from⁹⁶).

Two different approaches have been used in covalent docking⁹⁵, which differ in the way the ligand is modelled for the simulation: (i) flexible side chain method, and (ii) two-point attractor method. In case of *flexible side chain method* in AutoDock simulation, the fully flexible ligand is attached in an arbitrary conformation with its target, and then they form a stable complex. In this method (see Figure 2.8a), the ligand overlaps with the protein residue and then the complex conformation is optimized by AutoDock. In contrast, in *two-point attractor method*, a free ligand molecule is designed and then the potential is applied to bring together the covalently bound portions of ligand and target.

Figure 2.9b calculates two energetically attractive maps (shown with circles) at the site of covalent attachment in the protein (in gray), and uses two dummy atom (X and Z) types to target the ligand (in black) to the site.

Generally, both type of covalent docking methods need different input preparation protocols. Target structures were obtained from the protein data bank (PDB) or the results of molecular dynamics simulations. In the flexible side chain method (see Figure 2.10), the ligand file was created by adding two receptor atoms to the ligand coordinates in ideal chemical geometry, and then using this file to superimpose the ligand on the appropriate residue in the target protein. ADT was used to add hydrogens⁹⁵, calculate Gasteiger charges, and generate a modified flexible ligand, using default methods. The resulting side chain–ligand structure is treated as flexible during the docking simulation, sampling torsional degrees of freedom to optimize the interaction of the tethered ligand with the rest of the protein. Grid maps were calculated following the standard AutoDock protocol for flexible side chains⁹⁵. The torsions of the flexible residue have been randomized using AutoDock Vina.

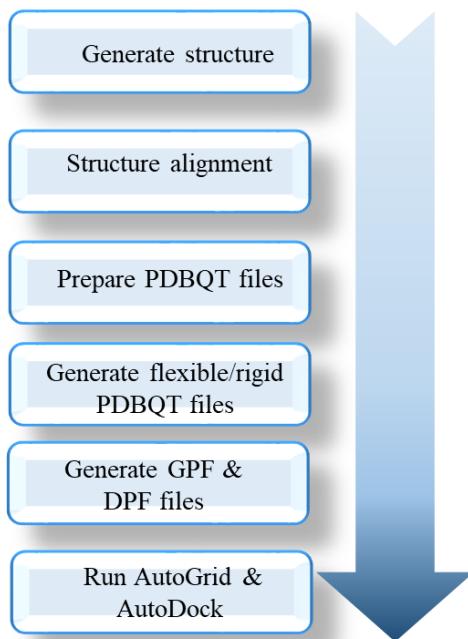


Figure 2.10: Workflow for flexible side chain covalent molecular docking

For the two-point attractor method, the ligand is extracted from the PDB file and modified by adding two extra atoms X and Z, corresponding to the two side chain terminal atoms. Hydrogens and charges were added, and to prevent any bias toward the known input ligand configuration, the resulting PDBQT coordinates were randomized (orientation, translation, and torsions) using AutoDock Vina⁹⁵. The grid parameter file (GPF) was modified to include the definition of the two Z-potentials for atoms X and Z. The potential centers were defined on the original coordinates of the residue atoms, and the grid map was calculated following the standard AutoDock protocol for ligand docking.

Chapter 3: Cell culture models

3.1 Introduction

Cell culture is an important and necessary technique in cancer research, stem cell research, drug discovery, and research pertaining to other types of diseases. Most of the studies are carried out on cells propagated in two dimensions (2D) on flat surfaces (i.e., cell monolayers). While useful, they have limitations, such as the lack of cell-to-cell and cell-to-ECM (extra cellular matrix) interactions, absence of the tumor microenvironment, and they are often not representative of the cells present in tumors. New and improved methods that implement three-dimensional (3D) cell culturing techniques suggest better architecture of organ tissue, and are therefore more popular today. A 3D cell culture creates an artificial environment in which biological cells are permitted to grow or interact with their surroundings in all three dimensions. With 3D techniques, the cell environment can be manipulated to mimic that of a cell *in vivo* and provide more accurate data about response to stimuli, drug metabolism, cell-to-cell interactions, tumor kinetic characteristics, metabolic profiling, etc. for different types of diseases. All of these characteristics are made possible by the 3D cultures' capability to resemble the architecture and interactions of a tumor *in vivo* while being cultured *in vitro*. Therefore, these unique features make a 3D culture a potential tool to provide alternative ways to study organ behaviour and it is expected to eventually bridge the gap between *in vitro* (2D cell culture) and animal models.

3.2 Comparison of 2D vs 3D cell cultures

Recently, 3D culture techniques have been widely used in research projects for predicting drug activity, metabolism and toxicity *in vivo*. Cells in 3D, as compared to 2D, have both advantages and disadvantages that are listed in Table 3.1.

Table 3.1 Advantages and disadvantages of 2D and 3D cell culture.

Culture	Advantage	Disadvantage
2D	<ul style="list-style-type: none"> • Cells in the cultures receive same amount of growth factors and nutrients • Cells can stay in the same stage of the cell cycle • Higher cell proliferation rate • Cheaper and faster than 3D cultures • Cells can go into apoptosis very easily by drugs • Highly replicable • Better for long-term cultures 	<ul style="list-style-type: none"> • Cell gap junctions are less common and less accurately present real junctions • Poor cell differentiation • Cells show less resistance to drugs and provide a false success of treatments • Drugs are not well metabolized • Genes and protein expression are often different • Cells cannot experience gravity nor polarity
3D	<ul style="list-style-type: none"> • Nutrients, growth factors and oxygen gradients similar to those in real tumors • Natural cell shape as well as cell growth are maintained • Possible to mimic the behavior and structure of a real tumor • Cell gap junctions are common • Cell-to-cell communication • Cells are well differentiated • Better drug metabolism than in 2D • Proliferation rates are realistic (and can be low or high depending on technique) • Genes and protein expression resemble those of animal models • Can be used to reduce the use of animals in research 	<ul style="list-style-type: none"> • Core cells often remain inactive due to less nutrients and hypoxia • More expensive than 2D cultures • Extraction of all cells for analysis is difficult • Difficult optimization of the assays (such as dose-dependent cell viability, cell migration etc.) • Requires more controlled culturing conditions than 2D cultures

There are several methods for 3D cultures depending on the type of experiment being performed, such as scaffold-based techniques, organoids, 3D bio-printed tumors, spheroids, and the CAM (tumor chorioallantoic membrane) model. Among these 3D cultures, the spheroid (Chapter 7) and CAM (Chapter 5 and 6) model are used commonly for cancer drug discovery and they are discussed below.

3.3 Multicellular spheroid model

To model solid tumors more effectively, several 3D culture systems have been established. Of these, the multicellular spheroids (organotypic cultures) model is the most suitable and widely used for the study of anticancer treatments^{10,96,97}. Tumor spheroids are heterogeneous cellular aggregates of about 300-500 μm diameter and they can reproduce many key features of solid tumors (as in *in vivo*) such as cell-cell communication and signaling pathways, deposition of extra cellular matrix (ECM) components, gene and protein expression. Spheroids can be formed within a few days using most of the cancer cells of the same type (homotypic) or in combination with endothelial cells, fibroblasts, or immune cells (heterotypic). By modulating the ratio of cancer to stromal or endothelial cells, it is possible to mimic part of the cellular heterogeneity of solid tumors. Large tumor spheroids with a diameter greater than 500 μm normally consist of three layers, i.e., proliferating, quiescent regions and a necrotic core, as shown in Figure 3.1a. Proliferating cells that have access to nutrients and oxygen, provide the driving force for tumor growth. It is a target of interest for tumor studies, since a lot of activities occur in this region. Quiescent cells have no growth or active motion but still consume nutrients. The necrotic core is comprised of dead cells which are regarded only as viscoelastic material without living activities. When the nutrient environment changes, proliferating cells may become quiescent cells and eventually die due to the limited distribution of oxygen and nutrients. In addition, quiescent cells may convert to the proliferating type if these cells received sufficient nutrients, which leads to heterogeneous situations within the spheroid core.

Spheroids treated either with drugs or radiation can present cell death, DNA damage, failure of the defense mechanism, and hindered cell proliferation (Chapter 7). Cell death due to external stimuli is observed mainly in the outer region of the spheroid

(i.e., proliferating region) whereas in the spheroid core, there is cell death due to lack of nutrients and oxygen. Hence, the 3D spheroid model is therefore considered a valid model to recapitulate features of tumor microregions, intervascular domains or micrometastases⁹⁸⁻¹⁰⁰. This 3D technique can increase the utility and predictive value of preclinical drug discovery studies, as shown in Figure 3.1.b.

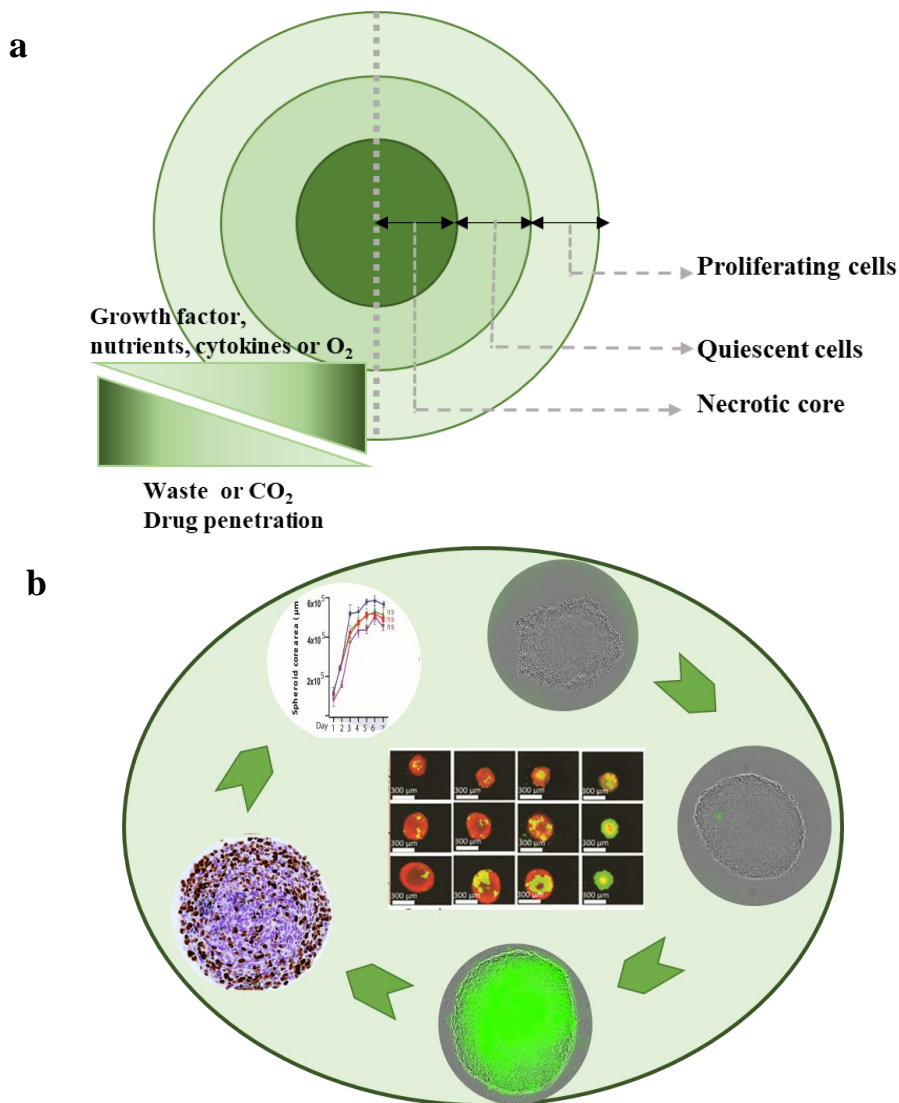


Figure 3.1 (a) Proliferating, quiescent regions and a necrotic core of 3D spheroid models; (b) Generation of 3D spheroids for the assessment of drug dose.

3.3.1 Protocol for formation of 3D spheroid model

Spheroids can be grown in many ways but not all cancer cell types can form spheroids. For this PhD work (in [Chapter 7](#)), we used the non-adherent spheroid technique to generate spheroids of 450-500 μm diameter in ultra-low attachment round-bottomed 96 well-plates (ULA Corning 7007). These microtissues grow in three dimensions, as cells adhere to each other rather than to the well plate (the workflow is shown in Figure 3.2).

Cells were transduced with the Nuclight Red Lentivirus reagent (Essen Biosciences, Ann Arbor, MI, USA) using their standard transduction protocol. The plates were incubated in the IncuCyte Live-Cell Analysis System (Sartorius, Ann Arbor, Michigan, MI, USA) and spheroid growth was followed during seven days after treatment. Data were analysed with the IncuCyte ZOOM version 2016B (Essen BioScience) as well as ImageJ software to collect the following metrics: (1) spheroid core area, corresponding to the proliferative region only; (2) total spheroid area; and (3) quantifications of dead cells.

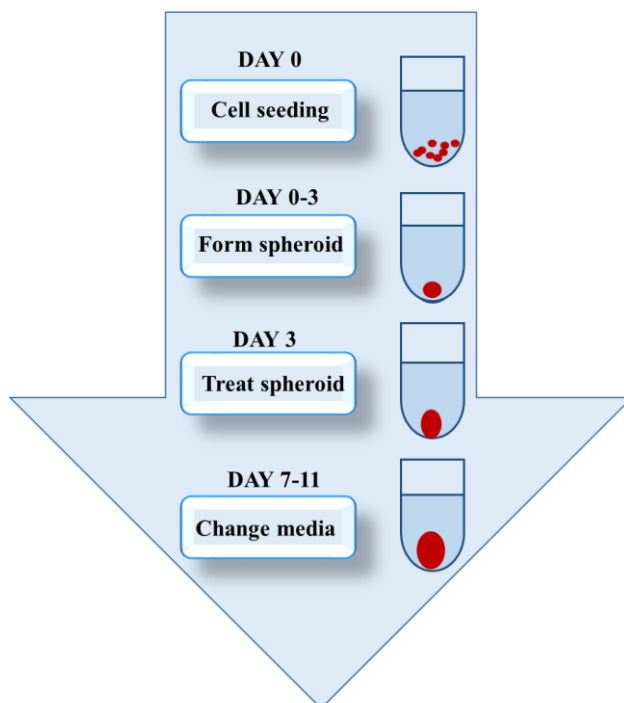


Figure 3.2 Workflow for 3D spheroid model.

3.4 Chick embryo chorioallantoic membrane (CAM) assay

In vivo studies are particularly relevant in some critical diseases such as cancer. However, conventional *in vivo* animal experiments are time-consuming, expensive, and they face ethical issues. Hence, an attractive alternative to the *in vivo* model is the chicken chorioallantoic membrane (CAM) assay. During the development of a chicken embryo, the CAM is formed by fusion of the mesodermal layer of the allantois with the mesodermal layer of the chorion. The CAM is the outermost extra-embryonic membrane, and due to its high vasculature, it is used in angiogenesis studies. Tumor cells rapidly form three-dimensional (3D) tumors, infiltrate the surrounding tissue and can even metastasize to different organs of the embryo. Well-developed vascular tissue (as shown in Figure 3.3) of CAM assay provides a technically simple way to study a complex biological system. However, only a limited number of studies have used the CAM assay to assess cancer invasion and metastasis¹⁰¹. The CAM assay is also a suitable model for acute toxicology studies of various drugs^{9,44,101,102}.

The CAM model has been clinically accepted for the testing of irritational potential of chemicals¹⁰³⁻¹⁰⁵. The National Institute of Health, USA, the Institutional Animal Care and Use Committee (IACUC), and the Association of New England Medical Center and Tufts confirm that a chick embryo that has not reached the 14th day of its gestation period cannot experience any type of pain. Therefore, a chick embryo of up to 14 days old can be used for the experimentation without ethical restrictions, and this can simplify the planning process.

Further advantages of the CAM assay are high reproducibility, cost effectiveness and short incubation times. However, the CAM assay has also several methodological challenges when used as an *in vivo* model in oncology research, such as inconsistent chick viability of chick embryo, inconsistent and low and delayed or slow tumor growth that are listed in Table 3.2.

Table 3.2 Advantages and disadvantages of mouse model vs CAM assay.

Model	Advantages	Disadvantages
Mouse	<ul style="list-style-type: none"> • Longer observation period (weeks to months) • Biologically and physically well known • Defined genetic background • Immune system is more mature than in the CAM model 	<ul style="list-style-type: none"> • Longer experimental length (months to years) • Costly • Animals need to be restrained • Difficult to calculate IC50 value of therapeutic agents, as the dose depends on body weight
CAM	<ul style="list-style-type: none"> • No need for approval of ethical committee (if experiments < 14 days) • Experimental assays are shorter (days) • Cost effective • Experiments can be reproduced easily • Naturally immunodeficient, so easy control of therapeutics agents • Multiple tests can be done in a single egg • Animals are not restrained • Can use primary and established human cell lines • Allows assessment of small quantities of therapeutic agents 	<ul style="list-style-type: none"> • Short observation period (days) • Cannot analyse cell-cell interactions • Morphology changes rapidly • Limited number of antibodies for the characterisation of chicken tissues

3.4.1 Protocol for CAM assay

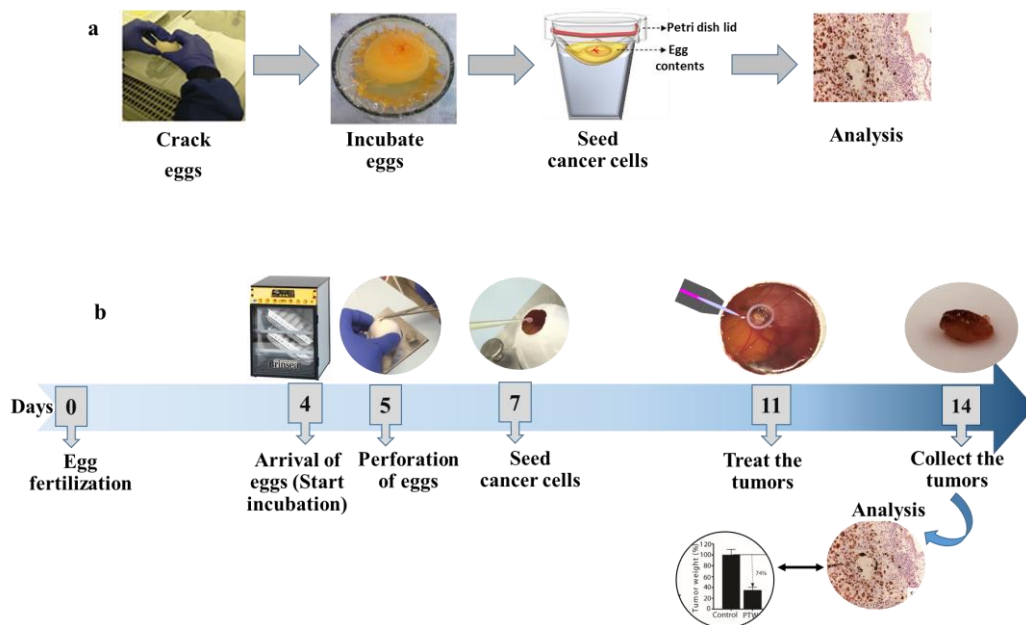


Figure 3.3 Workflow of (a) *ex ovo*, and (b) *in ovo* CAM assay.

The CAM assay has a more complex protocol than the spheroid model, because it requires the eggs to grow outside their natural environment. There are two common ways to use the CAM assay (shown in Figure 3.3) i.e., (a) *ex ovo* setup on a plastic cup or in a petri plate, or (b) *in ovo* setup by making a window on the egg.

The *ex ovo* methods (Figure 3.3a) are easy to control and require minimal handling expertise. This method has provided higher surface accessibility for the treatment (or analysis) and requires less expertise, but is not a preferred method due to the higher mortality rate. The embryo mortality is around 70–80% mainly because of the container used: (a) when using petri dishes, the high surface tension in the egg causes the rupture of the egg yolk; (b) when using a glass, although the surface tension is lower, there is a vigorous movement of the embryo (egg content) and thus the discs (that contains drugs or cells) placed are sunken, leading to no favourable outcome. These drawbacks eventually lead to overall low efficiency of *ex ovo* methods.

In contrast to the *ex ovo* methods, *in ovo* methods (Figure 3.3b) demand high expertise during handling. This assay requires high precision to create a window on the eggshell without disrupting the embryonic membrane, which is found to be the major reason leading to mortality of the embryos in this setup. Additionally, there are fewer accessible surface areas for manipulation during experimentation. However, it has a very low embryonic death (around 5-15%). For this study (Chapter 5 and 6), we used *in ovo* methods as depicted in Figure 3.3b and the details of the assay are described in Chapter 5 and 6.

Chapter 4: Reactive species accelerate signaling in wound healing

This Chapter is under review:

Ihn Han, In-Seok Song, Seung Ah Choi, Taebok Lee, Suk Ji, Maksudbek Yusupov, Priyanka Shaw, Annemie Bogaerts, Eun Ha Choi, and Jae Jun Ryu Enhanced Migration of Human Gingival Fibroblast by Non-Thermal Biocompatible Dielectric Barrier Discharge Plasma, *Cell Death and Differentiation*, 2021.

4.1 Abstract

This study hypothesized that the application of low-dose cold atmospheric plasma (CAP) to human gingival fibroblasts (HGFs) inhibits colony formation but not cell death and induces matrix metalloproteinase (MMP) expression, extracellular matrix (ECM) degradation, and subsequent cell migration, which can result in enhanced wound healing. HGFs treated with CAP for 3 min migrated to each other across the gap faster than those in the control and 5-min treatment groups at days 1 and 3. The phosphorylation of migration-related proteins focal adhesion kinase (FAK) and protein kinase B (AKT), FAK-mediated attenuation of wound healing or actin cytoskeleton rearrangement, and plasma-mediated reversal of this attenuation supported the migratory effect of CAP. We performed computer simulations to investigate the effect of oxidation on the stability and conformation of the catalytic kinase domain of FAK. We found that the oxidation of highly reactive amino acids, Cys427, Met442, Cys559, Met571, Met617, and Met643, changes the conformation and increases the structural flexibility of the FAK protein and thus modulates its function and activity, which is in qualitative agreement with the experimental results. In conclusion, low-dose CAP induces host cell cycle arrest, ECM breakdown, and subsequent migration, thus contributing to enhanced wound healing.

4.2 Introduction

The process of wound healing comprises three consecutive phases: inflammation, formation of new tissue and formation of the fibrotic scar¹⁰⁶. The whole process is influenced by mechanical forces that are transmitted to the cell through mechanoreceptors, such as integrin, ion channels, growth factor receptors, and G-protein coupled receptors¹⁰⁶. Mechanical forces can activate several signalling pathways that can regulate cell migration, proliferation, orientation, survival, etc. In the skin, fibroblasts and keratinocytes are key mechanosensitive cells, and the mechanical signals are transmitted via integrins that activate focal adhesion complexes containing the focal adhesion kinases (FAK)¹⁰⁷. FAK is a critical protein in cell mechanotransduction, which makes it a suitable target for drug therapy. It has been reported that the elevation of wound tension in response to FAK-mediated signaling caused a pro-fibrotic phenotype and hypertrophic scar formation¹⁰⁸. Additionally, mice deficient in FAK were found to be

significantly delayed in wound healing, and decreased thermal thickness due to over-activation of matrix metalloproteinase 9 (MMP9) enzyme¹⁰⁹.

FAK is recruited to the focal adhesions, where it binds to the cell membrane and other proteins such as talin and paxillin¹⁰⁸. FAK is composed of a FERM domain and kinase domain (KD). The KD contains the catalytic part of FAK and controls its enzymatic activity. FAK maintains its auto-inhibited conformation by a strong interaction of FERM with KD, and in this state, FAK protects the activation loop from phosphorylation by Src kinase family PTK, which further cause phosphorylation of FAK at Tyr₉₂₅. In this way, it creates a binding site for the SH2 domain of the Grb2 adaptor protein¹¹⁰⁻¹¹². It is observed that FAK acts similarly as it is done by the growth factor to recruit Grb2 to the plasma membrane and initiate a Ras/MAP kinase pathway^{113,114}. Further, the FAK/Src complex has been shown to phosphorylate additional substrates including paxillin and p130cas^{115,116}, which have also been proposed to mediate downstream functions of FAK to regulate cell migration in wound healing or tissue regeneration.

Disruption of the FERM-KD interaction leads to auto-phosphorylation of Tyr₃₉₇ (situated in the FERM-KD linker), resulting in full catalytic activation of the FAK protein¹¹⁷, which is crucial for many biological mechanisms, including adhesion signaling. After the disruption of FERM-KD, the auto-inhibited state is released (ATP-binding sites in KD) and then FERM domain of FAK protein can binds with extracellular matrix compound such as integrins and growth factors, underlying the important role of FAK in integrating diverse cellular signaling pathways. Thus, FAK plays an important role in regulating wound healing events, where the continual modulation of the interaction between the cell and the underlying extracellular matrix are necessary.

CAP is defined as an ionized gas consisting of charged particles (electrons and ions), radicals, atoms and molecules, and visible and UV photons^{10,17,21,27-30,45,49,50,58,65,118-120}. Recently developed biocompatible CAP, which uses ambient air and is conducted at a temperature lower than 40 °C, can be used in various biomedical applications, for example, for killing bacteria, viruses, and fungi, and even cancer cells^{10,26,27,45,65,119,120},

sterilising wounds^{15,121,122}, and enhancing wound healing^{17-21,35,58-60,123}. It is also widely used for oral bacterial inactivation and tooth whitening^{50,55,70}.

CAP has been successfully applied in patients with chronic wounds, such as chronic venous ulcers^{17,33}, and is thought to primarily act by killing bacteria and blocking bacteria-driven delayed wound healing. Furthermore, a few studies have dealt with the effects of CAP on the acute wound healing process and unveiled a clear signaling mechanism for wound healing^{17,19-21,35,58,60,123}. However, whether this effect is primarily due to a decrease in bacterial colonisation or direct stimulating effects on cells is still unclear.

In this Chapter, it is investigated whether CAP supplied with room air can play a positive role in the wound healing process, where FAK protein is key. To support the *in vitro* experiments (that is done by our South Korean collaborator from Plasma Bioscience Research Center (PBRC)), I performed only computer simulations to investigate the effect of oxidation on the stability and conformation of the KD of the FAK protein. To support the experiments and to study the effect of oxidation on the FAK protein at the atomic level, we performed molecular dynamics (MD) simulations. Specifically, we focused on the catalytic domain of the FAK protein, i.e., the KD, which is mainly responsible for initiating the kinase signaling in the FAK protein¹²⁴. Any modification in the KD (e.g., mutation or oxidation of its residues) can lead to a disruption of its interaction with the FERM (Four-point-one, ezrin, radixin, moesin) domain, which results in the phosphorylation of Tyr₃₉₇, eventually leading to a full catalytic activation of the enzyme^{125,126}. Our *in silico* results revealed that the oxidation of highly reactive amino acids Cys427, Met442, Cys559, Met571, Met617 and Met643 leads to conformational changes and a higher increase in the structural flexibility of the FAK protein, thereby changing its function.

4.3 Materials and Methods

Cell viability

The cell viability was measured by MTS assay (Promega, Madison, WI), following the manufacturer's instruction. The HGF cells were seeded into culture plates at a

concentration of 2×10^5 cells/35 mm culture dish in 2 ml of alpha-MEM media, and cultured over-night. After treatment by DBD plasma at a different time, the cells were incubated for 24 h, and then MTS reagent was added for 4 h. All supernatant sample was transferred to 96-well plate and read at 490 nm using a microplate reader (Biotek, VT, USA). For the ATP activity assays, cells were plated in 35 mm culture dish in the same condition with MTS assay. After 24 h, cells were lysed with CellTiter-Glo Luminescent Cell assay kit (Promega), and luminescence was read by a microplate reader (Biotek).

Colony formation assay

The isolated cells from HGF were firstly investigated by colony formation assay, using the method described in the previous work¹⁵. The cells plated at a density of 1×10^2 cells per mm^2 tissue culture dish were maintained for 15 days at 37 °C. The DBD plasma was applied at 2 L/min for 3 min at each time on the cells of experimental group. Then, the cells were fixed and stained in 4 % paraformaldehyde solution for 10 min, washed with phosphate buffer solution and then stained with 0.1 % crystal violet for 10 min, respectively. It was considered as colony forming units-fibroblast when more than 50 cells with a fibroblast phenotype were aggregated. The absorbance of crystal violet was read on a microplate reader, SynergyTMHT (BioTek) at 375 nm.

In vitro wound-healing assay

An initial 4×10^5 cells were seeded on both wells of 35 μm -dish (ibidi[®] Culture-Insert 2 Well, GmbH, Martinsried, Germany) for two-dimensional invasion assays. After 24 h in culture medium (dMEM), serum was starved, and immediately after cells were time-dependently treated with non-thermal DBD plasma for 3 and 5 min. After 24 h incubation, both confluent plates of HGF cells were removed, and the cells invading the gap (500 μm) were monitored under a microscope (Nikon Eclipse Ti, Japan). Thereafter, the wound closure rate was determined by measuring the area of the open wound at each time point relative to the area of the wound at the time of wounding using the TScratch[®] software program (CSElab, Zurich, Switzerland)¹²⁷.

Confocal fluorescence imaging of HGF morphology

HGF cells were seeded on sterilized cover glass and treated with plasma for 3 min with or without FAK inhibitor, and cultured for 72 h. After this period, cells were fixed using 4% paraformaldehyde. The localization of F-actin was determined using Phalloidin Alexa-488 (Abcam, Germany), cell nuclei was stained with Hoechst 33342 (Bio-Rad, CA, USA) according to manufacturer's instruction. Representative images were taken using the biological confocal laser scanning microscope OFV10-ASW (Olympus, Hamburg, Germany).

Computational setup

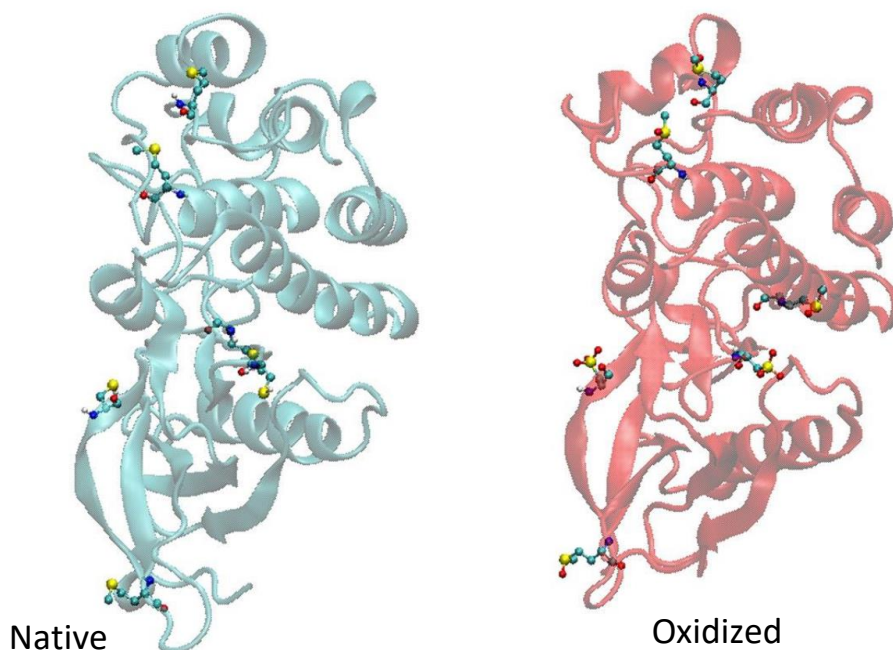


Figure 4.1. Schematic illustration of the native and oxidized KD of the FAK protein, together with its six amino acids (Met and Cys residues) selected for oxidation. The residues shown in the left and right figure are those before and after oxidation, respectively (see also Table 4.1).

We carried out molecular dynamics (MD) simulations to study the effect of oxidation on the kinase domain (KD) of the FAK protein (PDB ID: 4K9Y¹¹⁷). For this purpose, we prepared two model systems, i.e., the native KD and its oxidized form, illustrated in Figure 4.1. Specifically, we placed these model systems in a cubic box with

dimensions $\sim 8.5 \times 8.5 \times 8.5 \text{ nm}^3$ and solvated them by adding SPC^{128,129} water molecules together with a physiological (150 mM) concentration of NaCl. Afterwards, the systems were energy minimized using the steepest descent method, followed by a series of equilibration runs with positional restraints: (a) positional restraints on the KD backbone atoms, force constant equal to $10000 \text{ kJ}\cdot\text{mol}^{-1}\cdot\text{nm}^{-2}$, NVT ensemble (i.e., constant number of particles, volume and temperature), 2 ns; (b) the same as in (a) but in NPT ensemble (i.e., constant number of particles, pressure and temperature); (c) the same as in (b) but force constant equal to $1000 \text{ kJ}\cdot\text{mol}^{-1}\cdot\text{nm}^{-2}$; and (d) the same as in (b) but force constant equal to $200 \text{ kJ}\cdot\text{mol}^{-1}\cdot\text{nm}^{-2}$, 6 ns. In this manner, we were able to slowly equilibrate the systems without strong disturbances to their original structures. Subsequently, we carried out final equilibration simulations using again the NPT ensemble for 200 ns (in the case of native KD) and 750 ns (in the case of oxidized KD), without any positional restraints. All simulations were performed at 310 K and 1.0 bar, employing the V-rescale thermostat with a time constant of 0.1 ps¹³⁰ and Parrinello-Rahman barostat with a time constant of 2.0 ps¹³¹. A cutoff of 1.4 nm was used for non-bonded (i.e., van der Waals and Coulomb) interactions and the electrostatics were treated with the reaction field method¹³². In all simulations, a time step of 2 fs was used and the MD trajectories were saved every 100 ps. Periodic boundary conditions were applied in all directions. Using these conditions, we prepared three replicas of the native and oxidized KD systems with different initial velocities. Thus, in total six structures were prepared. These model systems were utilized to calculate the average root mean square deviation (RMSD) of the alpha carbons of the KD protein before and after oxidation. We also used these systems to determine the secondary structure of the native and oxidized KD protein, employing the last 50 ns of the equilibration. Moreover, using the last 50 ns of the equilibration, we calculated the solvent accessible surface area (SASA) of each amino acid (AA) residue in the native KD, to find out the highly exposed AAs to the solvent. These AAs are then considered to create the oxidized KD structure. Specifically, we applied oxidation to the KD system through modification/oxidation of the Met and Cys residues that have higher SASA and are highly reactive according to literature^{118,133} under plasma treatment (see Tables 4.1 and 4.2).

All MD simulations were carried out by the GROMACS 5.1.2 package¹³⁴, employing the GROMOS 54A7 force field¹³⁵. The parameter set of oxidized Met and Cys residues used in the oxidized KD was obtained from¹³⁶. For calculation of the SASA and the secondary structure of the native and oxidized KD proteins, we employed the *gmx sasa* and *gmx do_dssp* tools of GROMACS, respectively, by using the data obtained from 500 snapshots of the MD trajectory taken at every 100 ps from the last 50 ns and averaging over three replicas.

Table 4.1. Met and Cys residues of the kinase domain (KD) of the FAK protein. Rows highlighted with light blue color show the residues that have higher SASA and are hence chosen for oxidation.

AA residue	Residue number	SASA (nm ²)
CYS	427	0.59 ± 0.14
MET	442	0.94 ± 0.16
CYS	456	0.04 ± 0.04
CYS	459	0.03 ± 0.03
MET	475	0.18 ± 0.10
MET	499	0.05 ± 0.05
CYS	502	0.02 ± 0.02
CYS	559	0.32 ± 0.09
MET	571	0.46 ± 0.16
MET	589	0.04 ± 0.04
MET	607	0.03 ± 0.03
CYS	611	0.02 ± 0.02
MET	612	0.02 ± 0.02
MET	617	0.44 ± 0.09
MET	643	0.99 ± 0.16
CYS	647	0.14 ± 0.08
MET	655	0.00 ± 0.00
CYS	658	0.00 ± 0.00

4.4 Results

Effects of DBD plasma on the viability and colony formation ability of HGF

The effect of CAP on the viability of HGFs was assessed according to the

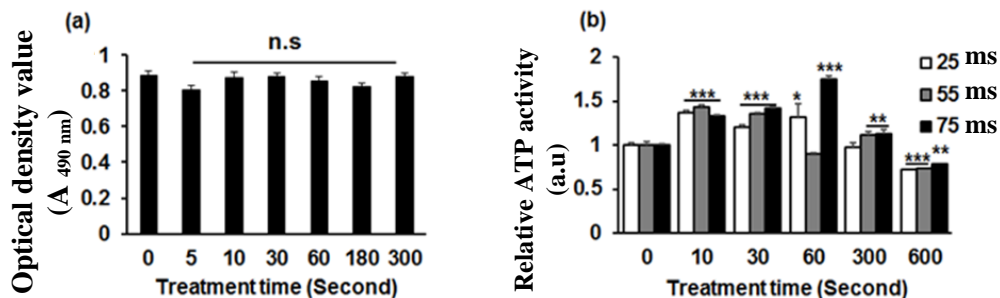


Figure 4.2. (a) Cell viability of HGFs after the exposure to CAP for 10 to 300 s. (b) The metabolic activity of HGFs was slightly elevated or stable as the exposure time increased from 10 to 300 s in the ATP activity assay, where * = $p \leq 0.05$, ** = $p \leq 0.01$, *** = $p \leq 0.001$.

exposure time via the MTS tetrazolium assay. The HGFs were stable in their viability with up to 300 s of air-plasma treatment at 2 L/min, 25 ms on-time, and 150 ms off-time. Later, the effect of CAP on HGFs was confirmed by the adenosine triphosphate (ATP) assay. The results showed that ATP as the energy currency of HGFs was elevated until 60 s, and it was stable as the exposure time increased from 10 to 300 s in 25, 50, and 75 ms on-time, respectively. However, the number of viable cells significantly decreased after the application of CAP for 600 s (Figure 4.2(a)). It was found that CAP treatment did not affect the HGF viability up to 300 s at a low exposure time of CAP (Figure 4.2(b)).

CAP induces FAK-related migration in HGF cells

HGF were assessed for migration activity after CAP treatment with basal medium. We treated HGF with CAP for 3 min (2 L/min, 25 ms plasma on-time, and 150 ms off-time) with or without the presence of FAK inhibitor and took a picture on day 0 and day 3 after treatment. HGF cells were stained with crystal violet at day 0 and day 3. The treatment with CAP facilitated the gap closure in HGF cells, whereas that with FAK inhibitor attenuated it (Figure 4.3).

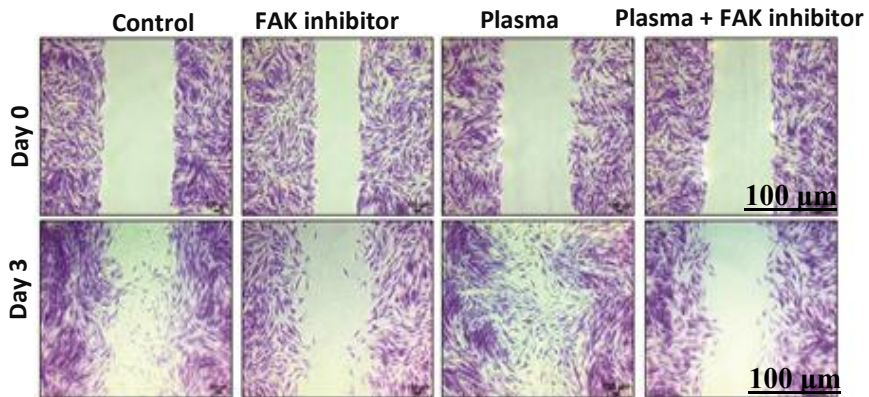


Figure 4.3. CAP induces FAK-related migration in HGF cells (cells were stained with crystal violet at day 0 and day 3). Scale bar = 100 μ m.

Plasma treatment rearranged the stress fiber of HGF cells

Plasma treatment enhanced the rearrangement of HGF cell's actin cytoskeleton, which facilitated cell migration. On the other hand, FAK inhibitor attenuated the plasma effect of actin cytoskeleton rearrangement and shortened actin fibers, indicating plasma-enhanced cell migration through the FAK-related cell signaling pathway (Figure 4.4).

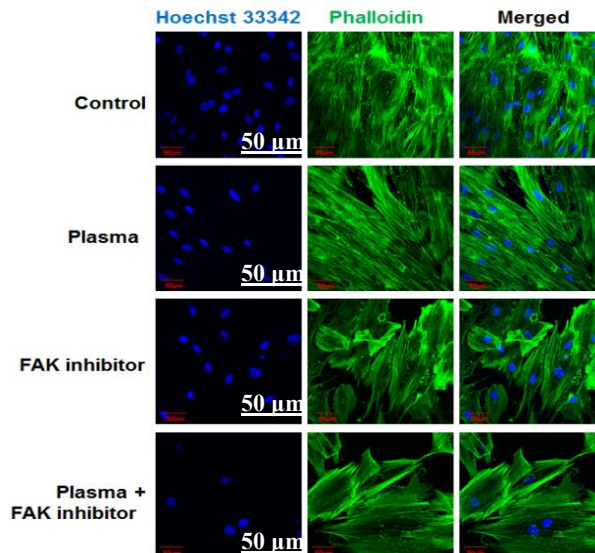
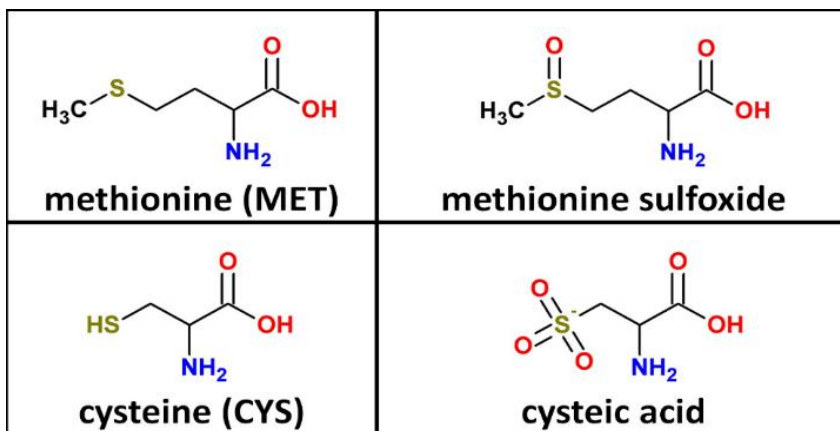


Figure 4.4. Cells were treated with plasma for 3 min, with or without FAK inhibitor. Actin staining with Alexa Fluor 488-phalloidin (green) and nuclei were counterstained with Hoechst 33342 (blue). Scale bar = 50 μ m.

Molecular Dynamics simulations

Table 4.2. Chemical structures of Met and Cys and their oxidized forms used for the creation of the oxidized KD of the FAK protein



Experimentally, it is demonstrated that the FAK protein expression is clearly activated at 3 min (low dose) of plasma exposure. To understand the effect of plasma oxidation on the KD of FAK, we oxidized specific amino acids (AAs), based on the chemical reactivity and modification^{118,133} as well as the solvent accessible surface area (SASA) of these AAs calculated in our simulations. Thus, we oxidized six residues of the KD (i.e., Cys₄₂₇, Met₄₄₂, Cys₅₅₉, Met₅₇₁, Met₆₁₇ and Met₆₄₃) that are highly reactive and have a higher accessibility to solvent (see table 4.1). To oxidize these AAs, we modified the Cys residues to cysteic acids and the Met residues to methionine sulfoxides (see table 4.2) based on^{118,133}. Figure 4.5 illustrates the time evolution of the root mean square deviations (RMSDs) of the alpha carbons of the native and oxidized KD, averaged over three simulations for each protein system. It is clear that the native KD is equilibrated after 100 ns and stays stable in the rest of the simulation time, yielding an RMSD fluctuating around 0.43 nm. In contrast, the oxidized KD stabilizes only at around 500 ns, at a higher RMSD value, fluctuating around 0.55 nm. Thus, oxidation leads to higher fluctuations of the RMSD, indicating that the oxidized KD becomes slightly more flexible. This is due to the conformational changes in the protein domain. Indeed, the results of the secondary structure analysis show slight alterations in secondary structure

of the KD after oxidation. Upon oxidation, the percentage of the random coil structure in the KD increases and the α -helix structure decreases by approximately 2-3 %, whereas other conformations stay more or less unchanged (see table 4.3). Thus, oxidation results in a slight increase in the structural flexibility, thereby affecting the protein stability. Note that the oxidation degree used in our simulations is low, which is aimed to correspond to the short plasma treatment time (3 min) used in our experiments. Therefore, it does not lead to drastic conformational changes. However, it is most likely sufficient to change the function of the FAK protein, thereby affecting its catalytic activity.

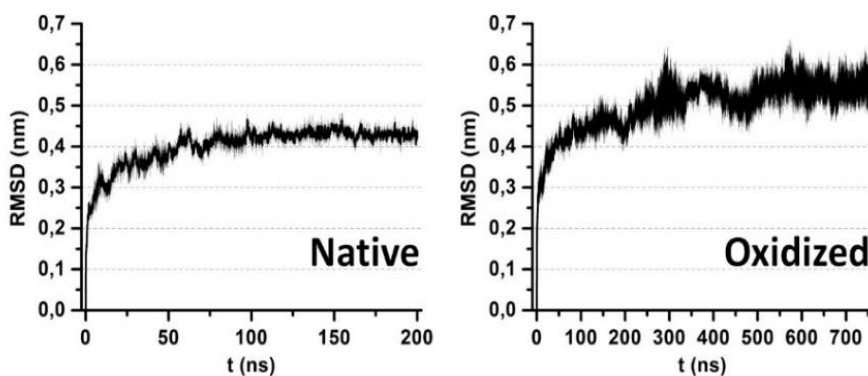


Figure 4.5. Average RMSDs of the alpha carbons of the native and oxidized KD of FAK.

Table 4.3. Secondary structure analysis of the native and oxidized KD of the FAK protein.

System	Coil	β -sheet	β -bridge	Bend	Turn	α -helix	3-helix
Native	0.22 \pm	0.15 \pm	0.01 \pm	0.13 \pm	0.12 \pm	0.35 \pm	0.02 \pm
	0.02	0.00	0.00	0.01	0.01	0.02	0.01
Oxidized	0.25 \pm	0.14 \pm	0.01 \pm	0.13 \pm	0.11 \pm	0.33 \pm	0.02 \pm
	0.01	0.01	0.00	0.01	0.01	0.01	0.01

4.5 Conclusion

In the present Chapter (our collaborators from PBRC did the experiment, and I performed the simulations), it is shown that low-dose of CAP treatment did not inhibit HGF proliferation. The migratory effect could be supported by new vessel formation and ECM breakdown. Overall, these synergistic actions of CAP could establish favourable wound beds and result in enhanced wound healing. Attenuation of cell migration or actin cytoskeleton rearrangement by FAK inhibitor indicated that CAP enhanced cell migration through the FAK-related cell signaling pathway.

A few studies demonstrated that ROS induce tyrosine phosphorylation of FAK through a variety of cellular signaling pathways^{137,138}. However, none of them explained the cause of FAK activation or discussed the oxidation-related changes in the conformation of this protein at the atomic level. In our MD simulations, we showed that oxidation of the KD of FAK, the degree of which most likely corresponds to a short plasma treatment time (3 min), results in a higher RMSD value (Figure 4.5). This indicates that the oxidized KD becomes slightly more flexible than the native KD, which is due to the conformational changes in the protein. Thus, oxidation results in a slight increase in structural flexibility, thus affecting its stability. This in turn might affect the FERM-KD binding, thereby disrupting this interaction, resulting in the phosphorylation of Tyr₃₉₇. Subsequently, this can change the function of the FAK protein, ultimately leading to an increase of its catalytic activity.

Chapter 5: Lipid peroxidation: reactive species enhance transdermal drug delivery by creating oxidative stress on lipids

This Chapter is published as:

Priyanka Shaw, Naresh Kumar, Dietmar Hammerschmid, Angela Privat-Maldonado, Sylvia Dewilde, Annemie Bogaerts “Synergistic effects of melittin and plasma treatment: A promising approach for cancer therapy” *Cancers* 11(8), p1109, 2019.

5.1 Abstract

As explained before, Cold atmospheric plasma (CAP) treated solution, such as PT-PBS solution are rich in reactive oxygen and nitrogen species (RONS) can disrupt the cell membrane integrity and induce cancer cell death through oxidative stress-mediated pathways. Thus, PT-PBS can be used in combination with anti-tumor drugs to facilitate their access into cancer cells and to reduce the required therapeutic dose. The aim of this chapter is to determine the reduction of the effective dose of Melittin (MEL, bee venom that has anti-cancer activity at very high dose) required to eliminate cancer cells by its combination with PT-PBS. For this purpose, we have optimized the MEL threshold concentration and tested the combined treatment of MEL and PT-PBS on A375 melanoma and MCF7 breast cancer cells, using *in vitro*, *in ovo*, and *in silico* approaches. We investigated the cytotoxic effect of MEL and PT-PBS alone and in combination to reveal their synergistic cytological effects. To support the *in vitro* and *in ovo* experiments, we showed by computer simulations that plasma-induced oxidation of the phospholipid bilayer leads to a decrease of the free energy barrier for translocation of MEL in comparison with the non-oxidized bilayer, which also suggests a synergistic effect of MEL with plasma-induced oxidation. Overall, our findings suggest that MEL in combination with PT-PBS can be a promising combinational therapy to circumvent the non-specific toxicity of MEL, which may help for the clinical applicability of drug delivery in the future.

5.2 Introduction

Melittin (MEL) is a water-soluble cationic amphipathic 26 amino acid α -helical peptide obtained from the honeybee (*Apis mellifera*) venom¹³⁹. It is a very non-specific cytolytic peptide that rapidly associates with phospholipid cell membranes. Several studies have demonstrated that MEL has inhibitory effects on the proliferation of various cancer cells *in vitro* via induction of apoptosis, necrosis and cell lysis¹⁴⁰. MEL can target a range of cancer cells, including those in leukemia, lung, renal, liver, bladder and prostate cancer, via activation of a caspase-dependent pathway¹⁴¹⁻¹⁴⁴. However, despite the convincing efficacy data against various cancers, its clinical applicability is precluded

due to the non-specific toxicity shown at high doses and thus, it is considered as a limiting factor for its use in cancer therapy ¹⁴⁵. Nevertheless, to reduce the nonspecific toxicity, several combinations of MEL with chemotherapeutic drugs and nanotechnology have been reported ¹⁴⁶⁻¹⁴⁹. However, these combinations still remain challenging ¹⁵⁰. Thus, further studies aiming to reduce the therapeutic dose of MEL and its associated unspecific cytolytic activity are needed. In this context, we propose the combination of MEL with PT-PBS, to overcome the current limitations of MEL. It is believed that CAP-produced RONS can enhance the fluidity of the cell membrane through lipid peroxidation, which eventually affects the intracellular biochemical signaling pathways ^{23,151}. In addition, it has been shown that CAP facilitates the uptake of nanoparticles and enhance their therapeutic action in cells ¹⁵².

In the present Chapter, *in vitro*, *in ovo*, and *in silico* approaches are used to study the ability of PT-PBS to reduce the nonspecific toxicity of MEL and to induce cell death in A375 melanoma and MCF7 breast cancer cells.

5.3 Materials and Methods

Reagents and cell lines

The following reagents and kits were used in this study: MTT (3-(4,5-dimethylthiazol-2yl)-2,5-diphenyltetrazolium bromide) (Sigma-Aldrich), DMSO (dimethyl sulphoxide) (Sigma-Aldrich), Annexin V-FITC apoptosis detection kit (BD Biosciences), Image-iT (Thermo Fisher Scientific), ProLongTM Gold Antifade Mountant with DAPI (Thermo Fisher Scientific), Lipid Peroxidation (MDA) Assay Kit (abcam). Melittin 85% (HPLC) was purchased from Sigma-Aldrich. The human breast adenocarcinoma (MCF7) and human malignant melanoma (A375) were obtained from the American Type Culture Collection (ATCC).

Plasma type and sample preparation

To make a PT-PBS solution, the kINPen® IND plasma jet (INP Greifswald/neoplas tools GmbH, Greifswald, Germany) was used ^{19,48}, as shown in Figure 5.1. For the plasma treatments, the plasma source was fed by argon gas for 9 min

to treat 2 mL PBS (pH 7.3) in a 12-well plate. MEL 85% (HPLC) was purified from bee venom and reconstituted in sterile PBS to form a stock solution of 1mg/ml before storage at -20°C. In this study, the abbreviations MEL-10, MEL-5, MEL-2.5, MEL-1.2, and MEL-0.6 are used for the MEL concentrations of 10 µg/ml, 5 µg/ml, 2.5 µg/ml, 1.2 µg/ml, and 0.6 µg/ml, respectively.

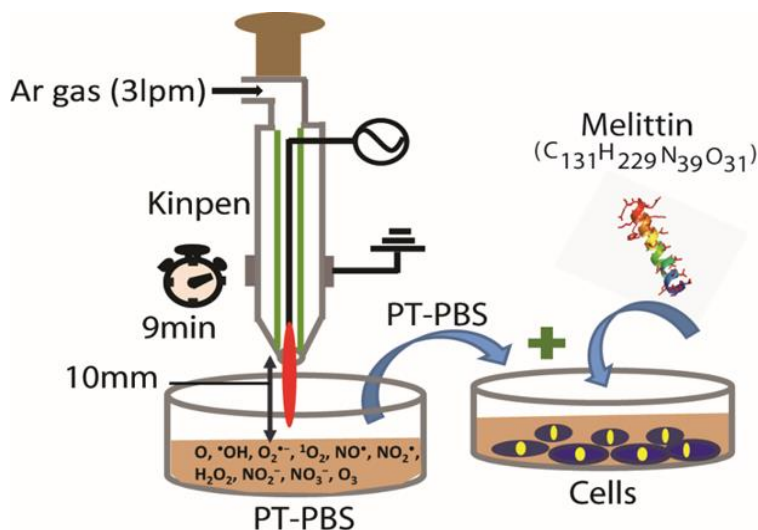


Figure 5.1. Experimental setup.

Analysis of cell cytotoxicity

The cytotoxicity of PT-PBS and MEL on breast adenocarcinoma (MCF7) and human malignant melanoma (A375) was evaluated. Both cell lines were cultured in Dulbecco's Modified Eagle Medium (DMEM; Life Technologies) supplemented with 10% (v/v) foetal bovine serum (Life Technologies) and 1% (v/v) penicillin and streptomycin (Life Technologies). The cell cultures were maintained at temperature of 37 °C in a humidified incubator containing 5% (v/v) CO₂. 2 × 10⁵ cells/well were seeded into 24-well plates to grow in complete media. After 24 h for the single treatment with PT-PBS and MEL, the medium was removed and immediately replaced with media supplemented with different percentages of PT-PBS, i.e., 20, 10, 5, 2.5 and 1.2 %, and different concentrations of MEL, i.e., MEL-10, MEL-5, MEL-2.5, MEL-1.2, and MEL-0.6. Subsequently, to obtain the synergetic effect of both treatments, the optimized doses of the single treatments (PT-PBS and MEL) were combined. A total volume of 1000 µL

per well was maintained after addition of the respective percentages of PT-PBS and MEL, the. In this study, the abbreviations PT-PBS -20, PT-PBS -10, PT-PBS -5, PT-PBS -2.5 and PT-PBS -1.2 will be used for the percentages of 20, 10, 5, 2.5 and 1.2 % of PT-PBS, respectively. The cells were placed in an incubator and their viability was monitored for 24 h post PT-PBS and MEL treatment. To check the viability, the MTT assay was performed after 24 h. In this assay, 50 μ l MTT (3-(4,5- dimethylthiazol-2yl)-2,5-diphenyltetrazolium bromide) solution (5 mg/ml in PBS) was added to each well. After 3 h incubation, the purple formazan precipitates in each well were released in the presence of 1000 μ l DMSO (dimethyl sulphoxide). The absorbance was measured using a microplate reader (BIO-RAD iMark Microplate reader) at 540 nm and the cell viability was assessed as the absorbance ratio between the treated and control sample, which was directly proportional to the number of metabolically active cells. To detect cell death, we used the Annexin V-FITC apoptosis detection kit. The treated/untreated cells were washed with 1 mL of cold 1 \times binding buffer after 3 h incubation and were subsequently trypsinized. Annexin V-FITC (0.5 mg/mL) was added to each sample. After incubation for 15 min at room temperature, the cells were again washed with PBS, stained with 0.3 mg/mL of PI (Propidium Iodide) and analysed using flow cytometry (Attune NxT Flow Cytometer, Brussels, Belgium).

Estimation of lipid peroxidation

After standardisation of the optimal dosages of PT-PBS, MEL alone and in combination through the MTT and flow cytometry analysis, we investigated the peroxidation of membrane lipids by fluorescence microscopy. We seeded 10^5 cells on cover glass. After 24 hr incubation, the cells were exposed to PT-PBS, MEL alone or to the combination of PT-PBS 10 and MEL-1.5. After treatment for 3h, the cells were incubated with 10 μ M Image-iT (lipid peroxidation) molecular probe for 30 min and fixed in 4% paraformaldehyde (in PBS) for 20 min and then permeabilized in cytoskeleton buffer (pH 6.8, 50 mM NaCl, 150 Mm sucrose, 3 mM MgCl₂, 50 mM Trizma-base, 0.5% Triton X-100). After permeabilization, the cells were washed thrice with PBS and subsequently Gold Antifade DAPI was used to mount the cells. The cells were imaged with Zeiss AxioImager Z1 microscope (Carl Zeiss, Göttingen, Germany)

equipped with an AxioCam MR ver.3.0 using a 40X objective, using filters for green fluorescent (GFP), red (Texas Red) and blue fluorescent (DAPI) channels. Next, flow cytometry was used to quantify the fluorescence intensity, after 3 h incubation with PT-PBS, MEL alone and in combination, at 37°C in a 5% CO₂ atmosphere. The treated/untreated cells were incubated with 10 µM Image-iT molecular probe for 30 min, and then harvested by trypsinization, washed twice with PBS, and finally the cells were resuspended in PBS to detect the fluorescence intensity by flow cytometry. To quantify the fluorescence intensity, we used Texas Red® (590 nm) and FITC (510 nm) emission filters, and we calculated the ratio of intensity in the Texas Red® channel to the intensity in the FITC channel. Moreover, for all treatments we also measured the malondialdehyde (MDA) concentration by the MDA assay kit, following the standard protocol according to the manufacturer's instructions. This method is based on the reaction of free MDA (present in the sample) with thiobarbituric acid (TBA) to generate a MDA-TBA adduct and its quantification is generally used as marker for lipid peroxidation.

Chicken Chorioallantoic Membrane Assay (CAM Assay)

Four-days old fertilized chicken eggs were incubated in horizontal position for 1 day at 37.7 °C and 65 % humidity in an egg incubator with automatic turning function (Ova-Easy 100, Brinsea). On day 5, the upper pole was disinfected and pierced with a 20G sterile needle (BD) and sealed with medical tape (Leukosilk S, Bsn medical). The eggs were incubated in vertical position (turning function off) to promote the relocation of the air cell. On day 7, the egg shell was cut to expose the chicken chorioallantoic membrane (CAM). A 1x1mm filter paper soaked in diethyl ether (Fisher) was briefly applied on a vascularized region of the CAM and a sterile silicone ring (ID=5 mm, OD=6 mm) was placed. A pellet of A375 cells (2 x 10⁶ cells per egg) was mixed with 15 µl growth reduced factor Matrigel (8.6 mg/ml, Corning) and loaded into the ring. The eggs were sealed with Tegaderm (3D) and placed back in the incubator for 4 days. On day 11, the Tegaderm was cut and a sterile plastic ring (ID=7mm, OD=8.5mm) was placed around the tumor. 100 µl of untreated PBS, MEL 1.5 µg in 100 µl PBS, 10% of PT-PBS and its combination (MEL + PT-PBS) were loaded into the ring. The eggs were sealed with Tegaderm and incubated until the end of the experiment. The cytotoxic effect of the

treatments was assessed on day 14 when tumors were excised and weighed in a precision balance (Mettler Toledo). All steps outside the incubator were carried out using a heat block (set at 37.7 °C) with a custom-made egg-shaped aluminum adapter.

Immunohistochemical Analysis for Ki-67

After weighing, the tumors were fixed with 4% paraformaldehyde for 14 h at 37 °C prior to paraffin embedding. Sections of 5 µm were cut, deparaffinized, rehydrated and stained with 1:1 hematoxylin and 0.5% eosin (HE) solution for histological analysis. For Ki-67 staining, antigen retrieval was performed with citrate buffer (10 mM, pH 6), at 96 °C for 20 min. Sections were permeabilised in 0.1% Tween-20 and blocked with 3% H₂O₂ in PBS (10 min, RT) and 2% BSA (30 min, RT). The primary antibody incubation was 40 min at RT (1/75 dilution; Mouse Anti-Human Ki-67 Antigen, Clone MIB-1, Agilent, Santa Clara, California, USA), followed by incubation with the secondary antibody (30 min at RT; Envision Flex HRP). Diaminobenzidine was used to visualize positive staining and haematoxylin to counterstain. Sections were imaged with Zeiss AxioImager Z1 microscope (Carl Zeiss, Göttingen, Germany) equipped with an AxioCam MR ver.3.0.

Computational analysis: Simulation setup

To support the experiments, we performed MD simulations to study MEL translocation across native and oxidized PLBs. We chose the PLB as the model system for the cellular membrane, as it provides the structural framework for the cell membrane. The PLB considered in this study consists of palmitoyl-oleoyl-phosphatidylcholine (POPC) lipids (see Figure 5.2). To study the effect of plasma-induced oxidation of the phospholipids on the translocation of MEL through the PLB, we assumed aldehyde oxidation products (POPC-ALD, see Figure 5.2b), which are found to be one of the key oxidation products¹⁵³. The simulations were carried out using the GROMACS package (version 5.1)¹⁵⁴, applying the GROMOS 54A7 force field¹⁵⁵. The force field parameters of the aldehyde product of the oxidized POPC (POPC-ALD) were obtained from¹⁵⁶. To generate initial configurations of the intact (or native) and oxidized POPC systems, we applied the Packmol package¹⁵⁷. Each system consists of 20,000 water molecules together with 128 phospholipids organized in two layers (i.e., 64 lipids with

corresponding water layer at the top, and 64 at the bottom, see Figure 5.2a). MEL has an α -helical configuration and was placed on the upper side of the PLB, i.e., in the water phase at about 1.5 nm above the head group region of the bilayer (see Figure 5.2a, and below for more details). To evaluate the effect of plasma-induced oxidation of the native POPC, we replaced randomly 64 POPC molecules with POPC-ALD (i.e., 32 at the top and 32 at the bottom), corresponding to 50% oxidation. Thus, we studied two model systems, i.e., native (0% oxidation) and 50% aldehyde-oxidized PLBs. We assumed 50% oxidation, which is enough to clearly investigate the effect of translocation of MEL across the bilayer, but low enough to avoid pore formation within the simulation¹⁵⁸.

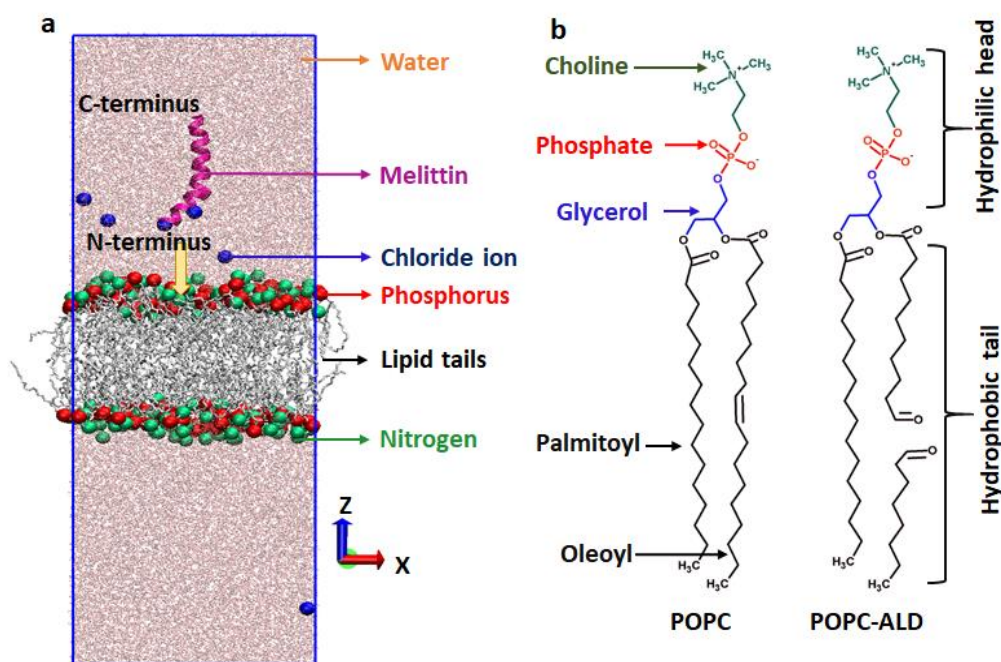


Figure 5.2. (a) Intact (or native) POPC PLB, together with MEL in the water region. For the sake of clarity, the N and P atoms of POPC are shown with bigger beads and the lipid tails are in grey. The yellow arrow indicates the pulling direction of MEL. (b) Schematic illustration of native (POPC) and oxidized (into aldehyde; POPC-ALD) phospholipids. The head group consists of choline, phosphate and glycerol, whereas the lipid tails are two fatty acid chains.

In order to obtain the average free energy profile (FEP) of MEL translocation across each system (see section below), we created three model systems for both native

and 50% oxidized PLB. In each system we changed the position of MEL in the xy-plane, keeping the distance between MEL and the center-of-mass (COM) of the bilayer constant in the z-direction (reaction coordinate). Moreover, to neutralize the system, we added 6 Cl⁻ ions, because of the +6 charge of MEL. After construction of the hydrated membranes with equilibrated MEL at the top, all the systems were energy-minimized using the steepest descent algorithm. Further, all structures (i.e., three native and three oxidized PLBs) were equilibrated for 200 ns (for the native case) and 300 ns (for the oxidized case) in the NPT ensemble (i.e., at constant number of particles, pressure and temperature), at 310 K and 1 bar, employing the semi-isotropic Parrinello-Rahman barostat¹³¹ with a compressibility and coupling constant of $4.5 \times 10^{-5} \text{ bar}^{-1}$ and 1 ps, respectively, as well as Nose-Hoover thermostat¹⁵⁹ with a coupling constant of 0.2 ps. For the non-bonded interactions, a 1.2 nm cut-off was applied. Periodic boundary conditions were applied to all systems in all Cartesian directions. The long-range electrostatic interactions were described by the particle mesh Ewald (PME) method¹⁶⁰, using a 1.2 nm cut-off for the real-space interactions. The SPC/E (extended simple point charge) model was used to represent the water molecules surrounding the membrane and MEL. In all simulations, we used a time step of 2 fs.

Umbrella Sampling

In order to determine the FEPs of MEL translocation through the native and 50% oxidized PLBs, we applied umbrella sampling (US) simulations. To avoid disturbances in the hydrophobic part of the bilayer, we kept MEL perpendicular to the surface (as shown in Figure 5.2a), also called the transmembrane state (T state), which is the stable state of MEL when it begins to diffuse inside the membrane¹⁶¹. Furthermore, to avoid the formation of the U-shaped conformation of MEL, we pulled the COM of the first three residues of the N-terminus of MEL towards the bilayer (see arrow indicated in Figure 2a).

For each FEP, we extracted 95 windows along the z-axis, which were separated by 0.1 nm. These windows were obtained by pulling the COM of the first three residues of the N-terminus of MEL in the z-direction (as mentioned above), applying a harmonic bias between MEL and the COM of the PLB, with a force constant of $2000 \text{ kJ.mol}^{-1} \text{ nm}^{-2}$

² and a very slow pulling rate of 0.001 nm.ps⁻¹. Each US simulation lasted for 200 ns, and the last 50 ns were used to collect the US histograms and to calculate the FEPs. A periodic version of the weighted histogram analysis method (WHAM) ¹⁶² implemented in GROMACS, was applied to construct the FEPs. The final energy profiles were obtained by averaging over three FEPs for each system, which differ from one another based on their starting structure, to allow for some statistical variations.

Mass Spectrometry Analysis

To detect the conformational change in MEL by native mass spectrometry (MS), 1 mg of MEL was dissolved either in 1 mL untreated PBS (control) or in 1 mL PT-PBS (i.e., 100% of PT-PBS). Each sample (50 μ L) was buffer exchanged to a MS compatible 100 mM ammonium acetate solution using a Micro Bio-Spin 6 column (Bio-Rad, Hercules, CA, US). MS experiments were conducted on a Synapt G2 HDMS (Waters, Manchester, UK) instrument. For this purpose, 3 μ L of sample was loaded into an in-house produced gold-coated borosilicate capillary and mounted onto the instrument. The sample was ionized by nano-electrospray ionization (nESI) and the generated ions were drawn into the vacuum of the instrument. The crucial parameter settings were 1.2 kV capillary voltage, 10 V sampling cone, 1 V extractor cone, 10 V and 2 V collision energy in the trap and transfer cell, respectively. Pressures throughout the instrument were set to: 2.75 mbar backing pressure, 4.55×10^{-3} mbar in the source region, and 2.5×10^{-2} mbar in the trap and transfer collision cells.

Statistical analysis

Data was analysed using the Student's t-test comparison analysis. The data was considered significantly different when * = $p \leq 0.05$, ** = $p \leq 0.01$, *** = $p \leq 0.001$. All values represent experiments done in triplicates. Data shown as mean \pm standard deviation (SD). Prism (Graphpad Software Inc.) and Excel Software (Microsoft Inc.) was used to compare the groups.

5.4 Results and Discussion

Effects of PT-PBS and MEL on cell viability and dose optimization

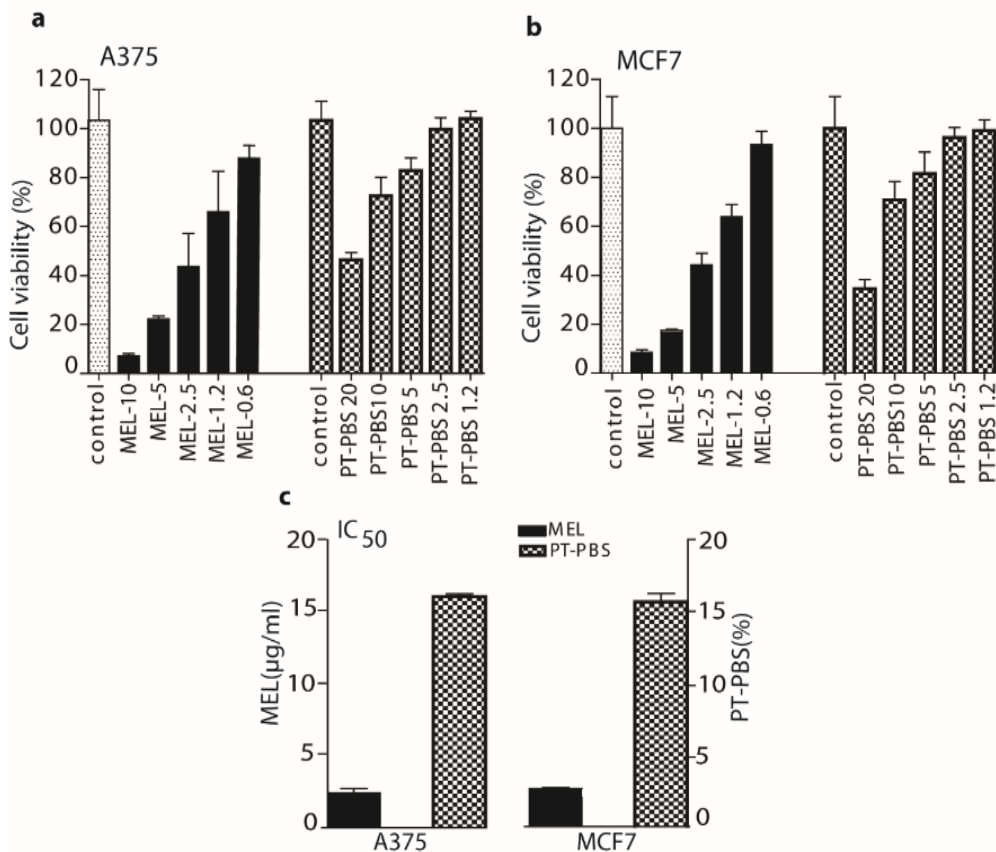


Figure 5. 3. Estimation of optimal doses of MEL and PT-PBS alone, for the cytotoxicity of A375 and MCF7 cells. We measured the cell viability of (a) A375 cells, and (b) MCF7 cells, at different doses of MEL and PT-PBS, after 24 h incubation. (c) Half maximal inhibitory concentration (IC₅₀) values of MEL and PT-PBS.

To verify the effect of MEL, PT-PBS alone and its synergy on the growth of melanoma and breast cancer cells, we analyzed the cell viability using the MTT assay. Treatments by MEL and PT-PBS alone exerted a concentration-dependent cytotoxic effect on both cell lines (Figure 5.3a and 5.3b). Up to 2.5 µg/ml of MEL shows significant ($P \leq 0.01$) decrease in viability in both cell lines. In addition, PT-PBS 20 and PT-PBS 10 also show significant inhibitory effect on both cell lines ($P \leq 0.05$) after incubation for

24h. For the controls, 20% and 10% non-treated PBS in the culture media were used for the MTT assay for the A375 and MCF7 cells, respectively, and 10% non-treated PBS in culture media for the cell death analysis and lipid peroxidation analysis in both cell lines.

The half maximal inhibitory concentrations (IC_{50}) of MEL and PT-PBS are shown in Figure 3c. The IC_{50} values of MEL in A375 and MCF7 cells were 2.5 and 2.8 $\mu\text{g/ml}$, respectively, while they were 16.4 and 16.5 %, respectively, for PT-PBS. Based on the IC_{50} values, we performed the combined treatment of MEL and PT-PBS, to investigate the synergy between both. For this purpose, we fixed the concentration of PT-PBS to a value lower than its IC_{50} values (i.e., we fixed it at 10 %) and we varied the concentrations of MEL in a range lower than its obtained IC_{50} values (i.e., 2, 1.5, 1 and 0.5 $\mu\text{g/ml}$).

As shown in Figure 5.4a and 5.4b, PT-PBS 10 alone yielded 65% viability for both A375 and MCF7 cells, while MEL-2, MEL-1.5, MEL-1 and MEL-0.5 alone resulted in ca. 50%, 60%, 77% and 90% cell viability for the A375 cells, and ca. 55%, 70%, 80% and 95% for the MCF7 cells, respectively. However, the combination of both showed a significant ($p < 0.001$) decrease, to ca. 8%, 15%, 32% and 60% for the different MEL concentrations in the A375 cells, and to ca. 10%, 17%, 34% and 64% for the different concentrations in the MCF7 cells.

To determine the synergistic cytotoxic effect of the combination of PT-PBS and MEL, the combination index (CI) value was calculated based on ¹⁶³. It is generally accepted that CI values < 0.1 indicate very strong synergism, CI = 0.1–0.3 strong synergism, CI = 0.3–0.7 synergism, CI = 0.7–0.9 slight synergism and CI = 0.9–1.1 nearly additive, while CI = 1.1–1.45 refers to slight to moderate antagonism ^{163,164}. As illustrated in Figure 4c, the CI analysis on A375 cells shows a synergistic cytotoxic activity for the combination of PT-PBS 10 with the following concentrations of MEL-2 (CI = 0.384), MEL-1.5 (CI = 0.412), MEL-1 (CI = 0.812), and MEL-0.5 (CI = 1.012). For the MCF7 cells, the CI values are very similar, i.e. MEL-2 (CI = 0.372), MEL-1.5 (CI = 0.426), MEL-1 (CI = 0.846), and MEL-0.5 (CI = 1.02). The combination of PT-PBS 10 with MEL-2 or MEL-1.5 clearly yields synergism, indicating that this combination can reduce the toxicity dose of MEL, and thus avoid the side effects related to higher doses of MEL. However, literature shows that MEL concentrations of up to 2 $\mu\text{g/ml}$ do not significantly inhibit cell viability in melanoma and lung cancer ¹⁶⁵⁻¹⁶⁷. Thus,

we performed our further experiments with a low dose, i.e., MEL-1.5, in combination with PT-PBS 10, as optimal combination for both cells.

Influence of PT-PBS and MEL on Cell Death

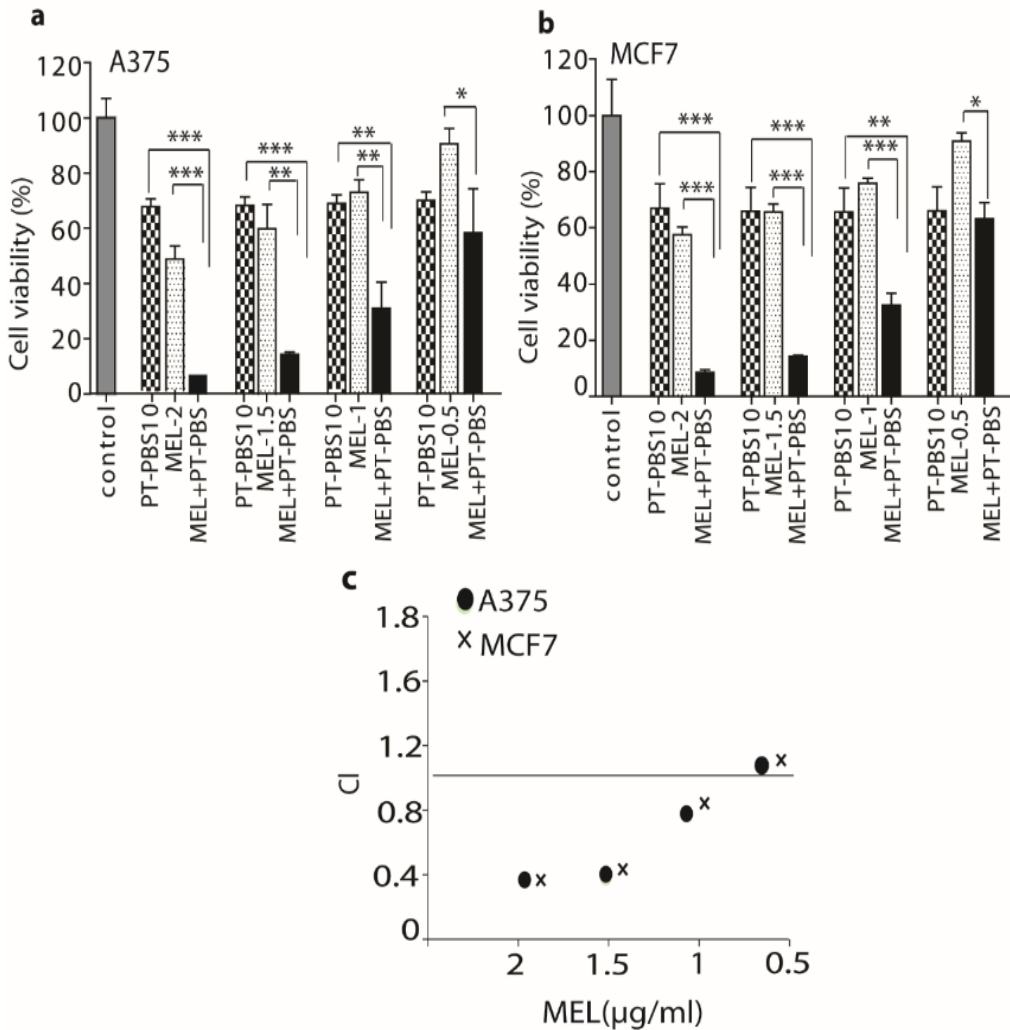


Figure 5.4. Analysis of cell viability of (a) A375 and (b) MCF7 cells treated with a fixed dose of PT-PBS (10%), and varying doses of MEL (i.e., 2, 1.5, 1 and 0.5 μg/ml) alone and in combination, 24h after treatment. (c) Combination index (CI) of PT-PBS (10%) with MEL (at 2, 1.5, 1 and 0.5 μg/ml), in A375 and MCF7 cells (see text). All values are expressed as mean ± SD; * = p ≤ 0.05; ** = p ≤ 0.01; *** = p ≤ 0.001.

To further demonstrate the synergism, and for clearer observation of cancer cell death after treatment with PT-PBS and MEL alone and in combination, we performed flow cytometry analysis. We also analyzed the degree of apoptosis/necrosis after treatment of both cell types. FITC Annexin V and PI negative cells are considered as viable; if the cells are FITC Annexin V positive and PI negative that cells are considered as early apoptotic; however, if cells are both FITC Annexin V and PI positive that cells are considered as late apoptotic or already dead (by necrosis). Hence, this assay does not differentiate between apoptotic and necrotic cell death as both populations are positive for both FITC Annexin V and PI. Therefore, in the current experiments, Annexin V and PI positive staining represent late apoptotic combined with necrotic cell death¹¹⁹.

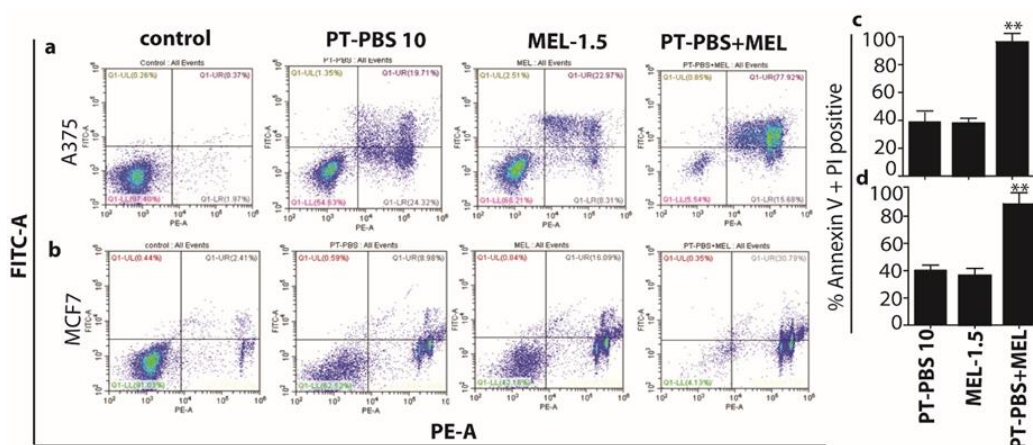


Figure 5.5. Flow cytometry analysis of (a) A375 and (b) MCF7 untreated controls, or cells treated with PT-PBS 10, MEL-1.5, and combined treatment (PT-PBS 10 and MEL-1.5), where * = $p \leq 0.05$, ** = $p \leq 0.01$, *** = $p \leq 0.001$.

As shown in Figure 5.5a,c for A375 cells, PT-PBS 10 and MEL-1.5 alone induced 38% and 35% late apoptosis/necrosis (Annexin V positive, PI positive), respectively, while the combined exposure induced 96% late apoptosis/necrosis ($p \leq 0.01$). In a similar way, PT-PBS 10 and MEL-1.5 alone induced 37% and 30% late apoptosis/necrosis in MCF7 cells, respectively, while their combination induced 92% late apoptosis/necrosis ($p \leq 0.01$, Figure 5.5b,d). These results indicate that the combined action of PT-PBS 10 and MEL-1.5 on both cancer cell lines is more than the sum of their individual effects, which is in agreement with the CI values shown above (Figure 5.4c). Altogether, these

findings support the synergistic cytotoxic action of PT-PBS 10 and MEL-1.5 in cancer cells.

Effect of PT-PBS and MEL on lipid peroxidation

Lipid peroxidation generally refers to the oxidative degradation of cellular lipids by reactive oxygen species. Peroxidation of unsaturated lipids affects the cell membrane properties¹⁶⁸ and signal transduction pathways¹⁶⁹. Thus, to evaluate the change in membrane integrity upon treatment with PT-PBS and MEL, we estimated the lipid peroxidation with the MDA assay and fluorescent probe. As shown in Figure 6a, the A375 cells incubated with PT-PBS 10 and MEL-1.5 alone yielded ca. 5.2 μM and 4 μM peroxidation product (malondialdehyde; MDA), respectively, while in combination they exhibited a significant formation of MDA (ca. 15 μM , $P \leq 0.01$). Likewise, for the MCF7 cells, PT-PBS-10 and MEL-1.5 alone produced ca. 4.5 μM and ca. 4 μM MDA respectively, while their combined exposure shows a significantly higher MDA production (ca. 10.5 μM , $P \leq 0.01$). In addition, lipid peroxidation following PT-PBS-10, MEL-1.5 and combined exposure was quantified in both cancer cells, using the ratio of green and red fluorescence intensities, as shown in Figure 6b. The ratios increased significantly in both cancer cells, when we applied the combined treatment ($P \leq 0.05$).

Figure 5.6c and Figure 5.6d show the fluorescence images of the A375 and MCF7 cells stained with lipid peroxide detection reagents, after addition of PT-PBS-10, MEL-1.5 alone and in combination. Compared with the separate treatments, the combined exposure shows most of the signal is in green channel, which indicates lipid peroxidation. we also detected lipid peroxidation products around the membrane, indicating a change in the physical properties of the cellular membranes. This can cause covalent modification of proteins and nucleic acids, which might eventually be critical mediators of oxidative stress-mediated cell death¹⁶⁹. Thus, the combined treatment with PT-PBS 10 and MEL-1.5 induces lipid peroxidation in both cancer cell lines, which correlates with the cytotoxic effect of the combined treatment observed above.

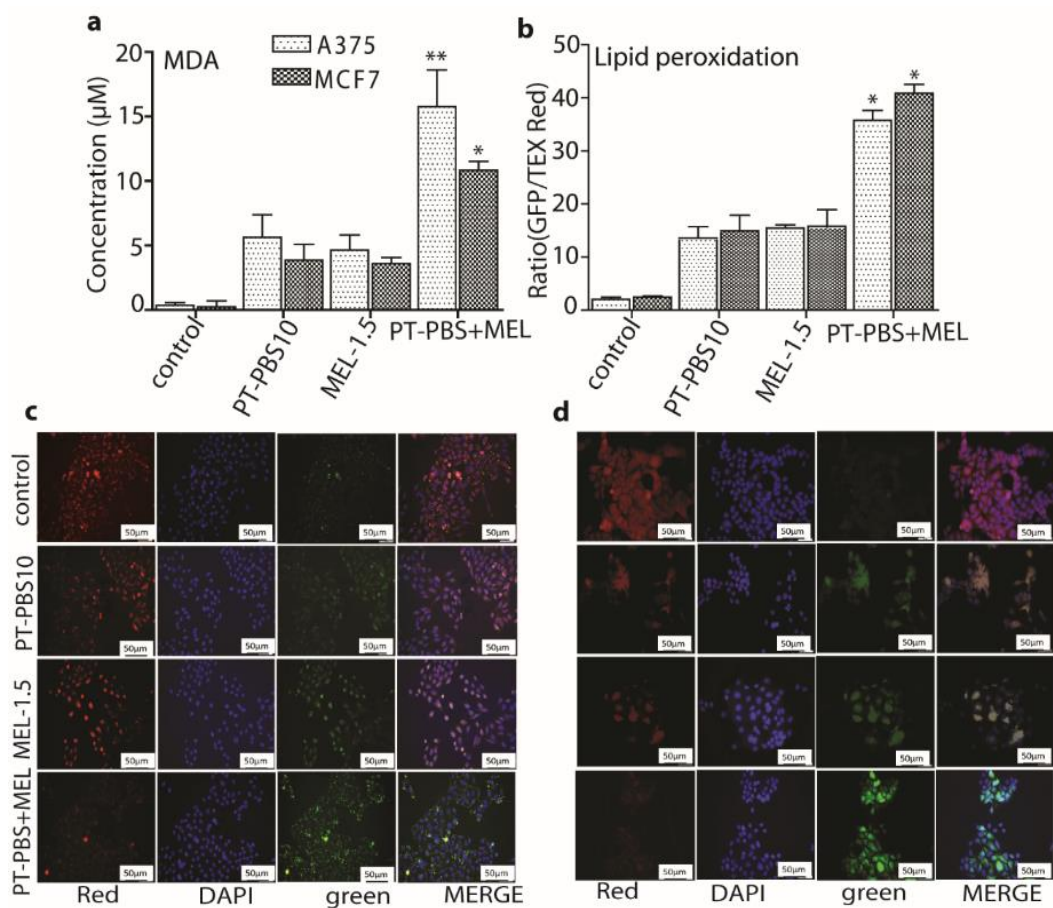


Figure 5.6. Change in membrane integrity upon PT-PBS-10, MEL-1.5 and combined treatment in both cancer cell lines, by (a) measurement of the concentration of the peroxidation product malondialdehyde (MDA), and (b) flow cytometry analysis. All values are expressed as \pm SD; * = $p \leq 0.05$; ** = $p \leq 0.01$. Fluorescence images of (c) A375 and (d) MCF7 cells, stained with lipid/lipid peroxide detection reagents. Red fluorescence represents non-oxidized membrane lipids, DAPI (blue) represents the nuclear counterstain and green represents the oxidized membrane lipids. Scale bars = 50 μm .

Effect of PT-PBS and MEL on malignant melanoma cancer tumors of the CAM model

Malignant solid tumors were analyzed macroscopically by using HE and Ki-67 staining. The stained tumor tissue sections displayed changes in morphology upon all treatments. Interestingly, the combined treatment induced more cellular shrinking and presence of pyknotic dark small nuclei as a result of chromatin condensation, compared to the PT-PBS 10 and MEL-1.5 treatments alone (Figure 5.7a). In contrast, untreated (control) cells presented a more prominent malignant phenotype with mitotic activity (HE staining, Figure 5.7a). To assess the proliferative state of cells in the treated tumors, tissue sections were stained for the proliferation marker Ki-67. The untreated tumors presented the highest levels of Ki-67 positive cells. We observed that tumors exposed to the combined treatment presented the lowest number of Ki-67 positive cells, followed by tumors treated with PT-PBS 10 and MEL1.5 alone (Figure 5.7b). These results suggest that the combined treatment of MEL+PT-PBS has a detrimental effect on cell proliferation, as it reduced the number of Ki-67 positive cells more efficiently than the sum of the individual treatments.

In agreement with the histological analysis of tumor specimens, the tumor weight also demonstrated a reduction of tumor size upon treatment (Figure 5.7c and 5.7d). The combined treatment significantly reduced the tumor weight by approx. 76%, whereas the tumors treated with PT-PBS 10 and MEL- 1.5 showed a reduction in weight of approx. 30% and 35%, respectively (Figure 7c). Hence, these results indicate that the combined treatment induced a synergistic reduction of cell proliferation, as its effect on tumor weight (76% reduction) was approx. 11% higher than the sum of both treatments (reductions of 30% + 35%). These findings are in agreement with the *in vitro* results shown above.

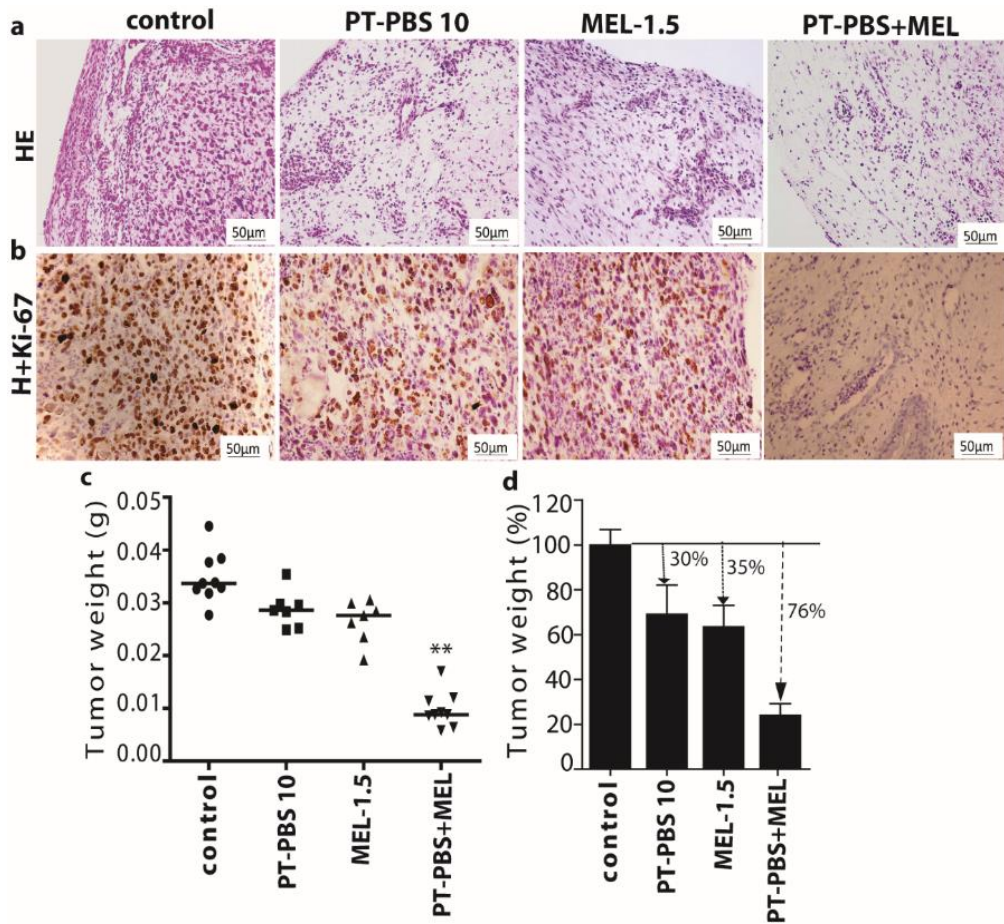


Figure 5.7. The combined treatment reduced the tumor size and expression of the proliferative marker ki67 in melanoma cancer tumors in ovo. (a) Representative images of HE and (b) Ki-67 staining of tumors exposed to PT-PBS-10, MEL-1.5 or combined treatment. Scale bars represent 50 μm . (c) Weight reduction upon treatments in tumors in ovo. Each dot represents one tumor. (d) Quantification of tumor weight in percentage (treated/control*100%) after treatment (PT-PBS 10, MEL-1.5 or combined treatment). Vertical arrows indicate reduction in tumor weight. All values are expressed as \pm SD; ** = $p \leq 0.01$.

Plasma Oxidation of MEL: Mass Spectrometry Analysis

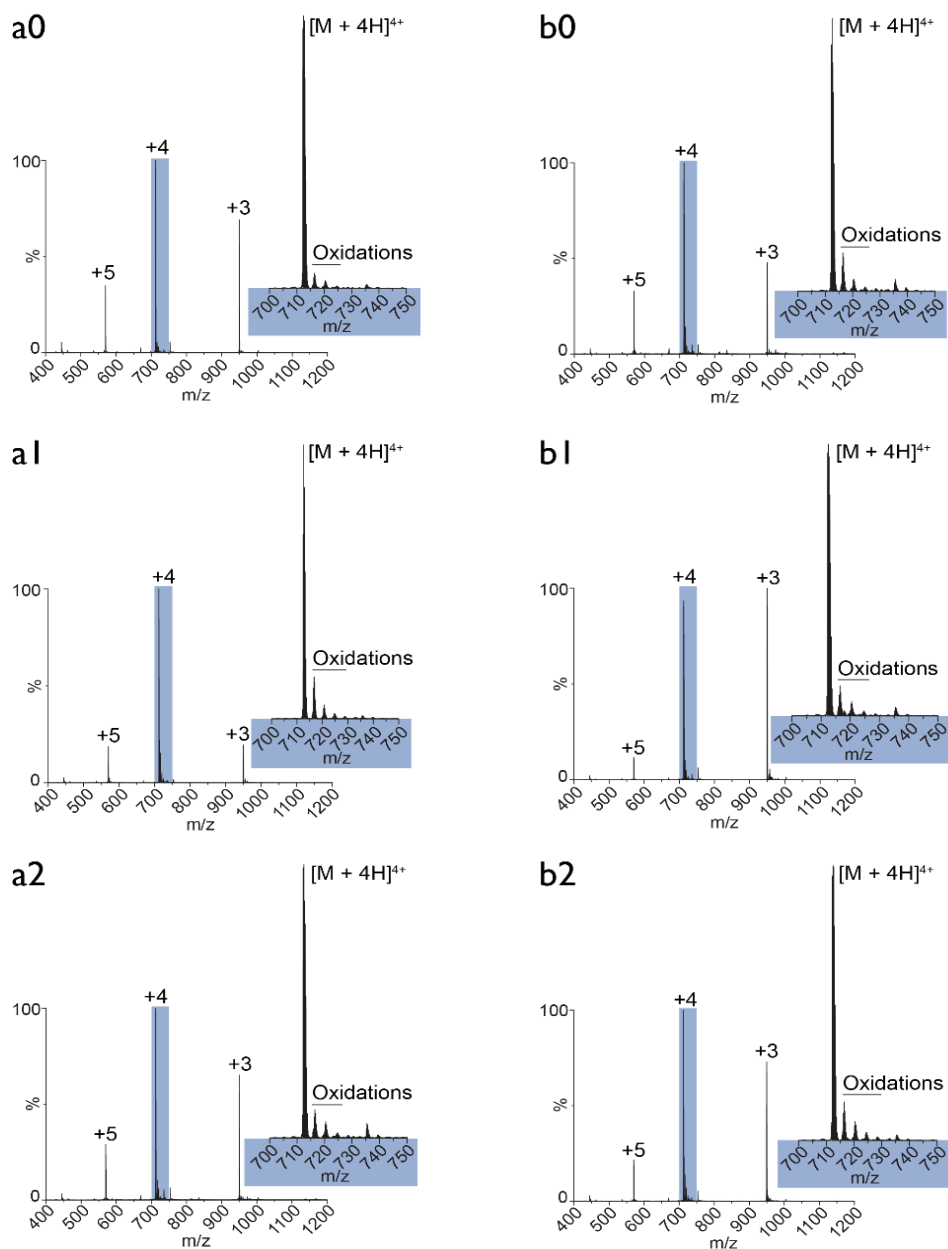


Figure 5.8: Native MS of MEL. The figure shows an overview of native MS spectra of MEL solubilized either in untreated (a) or plasma-treated PBS buffer (b) after different time points of incubation (0: 1 min; 1: 60 min; 2: 120 min).

To better understand the synergistic effect of PT-PBS and MEL, we investigated the effect of plasma treatment on the oxidation level of MEL. For this purpose, we dissolved MEL either in untreated (control) or in PT-PBS buffer and we incubated the solution for 1, 60, or 120 min. Figure 8 shows the native MS measurements of the control (a) and the plasma-treated (b) samples. The indices refer to the different time points of incubation (0: 1 min, 1: 60 min, 2: 120 min). As illustrated, the comparison between control and plasma treatment reveals no differences in the oxidation level of MEL. The observed oxidations (700–750 m/z) may originate from the electrospray ionization¹⁷⁰, as indeed reported for MEL¹⁷¹, but at much harsher operating conditions than applied in this experiment. Moreover, the measurements do not show an increase in the number of oxidations over time. Thus, no differences were observed in the spectra acquired after one minute and after two hours. Independent of whether the oxidations are already present in solution or are induced by the electrospray ion source, in any case the plasma treatment applied in the form of solubilizing MEL in plasma-treated PBS buffer does not have any influence on these observed oxidations. Hence, we can conclude that MEL is not oxidized by plasma, and that the synergistic effects of MEL and PT-PBS must be attributed to other effects. One possibility is the enhanced translocation of MEL through the cell membrane upon plasma-induced oxidation of the phospholipids. This will be discussed in the next section.

MEL Translocation across Native and Oxidized Phospholipid Membrane Revealed through MD Simulations

To gain further insight into the experimentally observed synergetic effect between MEL and the RONS present in PT-PBS and to investigate the mechanisms of MEL access to cancer cells through oxidized membranes, we performed US MD simulations.

This method allows us to elucidate the MEL translocation across the native and oxidized PLBs, based on the FEPs plotted in Figure 5.9. Based on the polarity of the lipids, the hydrophilic part refers to the upper and lower lipid head groups (light blue color in Figure 5.9a), while the hydrophobic part refers to the lipid tails of the PLB (grey color in Figure 5.9b-e). In the native case, when MEL enters from the water phase to the hydrophilic head group of the upper leaflet (see Figure 5.9b and 5.9c), it shows a high

affinity with the (charged) head groups of the PLB, due to strong Coulomb interaction¹⁷². As a result, the potential of mean force for insertion of MEL shows a drop in the free energy barrier, making insertion of MEL favorable (see first minimum near $z=1.5-2$ nm in Figure 9a, indicated with the arrow). Subsequently, the N-terminal of MEL moves through the hydrophobic tail region (see Figure 5.9d and 5.9e) and experiences a permeation barrier at the center of the bilayer. It is due to the fact that the residues of MEL near the C-terminal (i.e., LYS₂₁, ARG₂₂, LYS₂₃ and ARG₂₄) with a net charge of +4 prefer to stay at the upper head group-water interface, whereas the N-terminal residue LYS₇ with a net charge of +1 prefers to move into the inner head group-tail interface, which eventually leads to an increase of the free energy barrier at the center of the PLB¹⁷². When (the N-terminal of) MEL traverses further towards the lower leaflet, the free energy drops again, because most of the hydrophobic residues of MEL stay in the hydrophobic region of the PLB. Finally, at the lower head group region of the PLB, the energy rises again, because the charged residue LYS₇ near the N-terminal of MEL binds with the head group of the lower leaflet, resulting in a new barrier against translocation¹⁷³. Moreover, as MEL penetrates through the bilayer, its conformation changes, but most of its helical structure is retained at the surface of the PLB (see Figure 5.9b-5.9d).

It is important to notice that the first free energy maximum for the native case (see Figure 5.9a) is 29.28 ± 1.04 kJ/mol, obtained at the center of the bilayer (i.e., $z=0$ nm) and the second maximum is 24.9 ± 2.3 kJ/mol, obtained at around $z=-2$ nm, which indicates that MEL has to face multiple barriers across the bilayer, making the translocation more difficult. In addition, we observed an asymmetric free energy profile, that is most likely due to the disturbance and conformational changes in the PLB, which was observed in other simulation studies as well¹⁷².

On the other hand, in the oxidized PLB, the energy reaches a minimum in the center of the bilayer, because when the lipid tails are oxidized, they become less apolar and hence the hydrophilicity of the membrane core increases dramatically, so that MEL can penetrate more easily. In addition, on top of the general minimum in free energy, there are multiple free energy local maxima and minima, due to interactions of the amino acid side chains of MEL with the lipid tails. We can thus conclude from Figure 8a that the free energy barrier for the transport of MEL across the PLB decreases upon oxidation,

and even disappears in large enough oxidation degrees. Hence, the probability of MEL permeation to the cell interior increases. Thus, the simulation results can explain the experimental observations, as the RONS present in PT-PBS (e.g., H_2O_2 , NO_3^- and NO_2^- ions^{24,151} oxidize the cell membrane (as can be deduced from the lipid peroxidation experiments, see Figure 5.6). The latter increases the MEL permeation probability, so that lower doses of MEL already give cytotoxic effects. This will eventually reduce the toxic side effects for cancer patients.

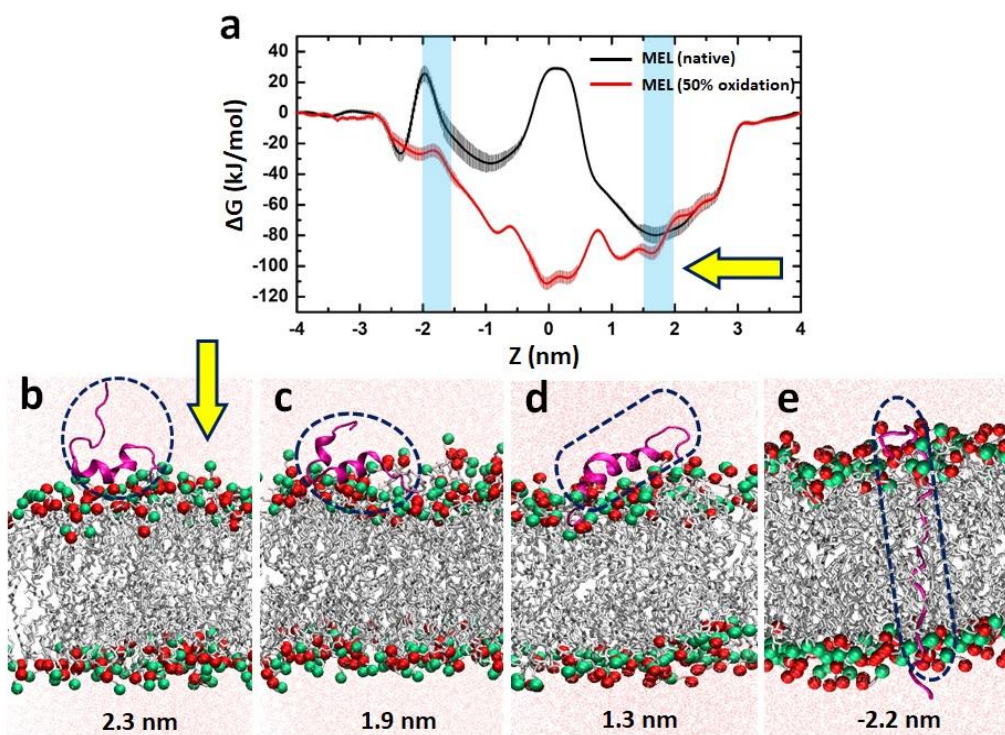


Figure 5.9. (a) Free energy profiles for translocation of MEL across the native and 50% oxidized PLB. (b)-(e) MEL at different positions of the native PLB. P and N atoms in the PLB are shown in red and green, respectively. MEL (shown within dashed circles/ovals) and the lipid tails are presented in magenta and grey, respectively. The light blue color in (a) represents the upper (right) and lower (left) head groups of the PLB. The yellow arrows in (a) and (b) indicate the direction of MEL translocation. At the bottom of (b)-(e), the respective positions of the N-terminal of MEL are indicated, referring to the z-axis of (a).

5.5 Conclusion

Bee venom is considered as a potential weapon against cancer. Melittin (MEL), a major polypeptide of Bee venom, is thought to function as lytic agent, and has been used traditionally in various cancer therapies¹⁷⁴ However, at high treatment doses, it exhibits severe nonspecific toxicity, because of its lytic properties¹⁷⁵. In this Chapter, we describe for the first time a combined treatment of MEL with PT-PBS that reduces the effective dose of MEL required to eliminate cancer cells. We have used *in vitro*, *in ovo* and *in silico* approaches to investigate the synergistic effect of PT-PBS and MEL on A375 melanoma and MCF7 breast cancer cells. We have previously demonstrated that CAP-treated liquids, such as PBS, deionized water and culture media, can effectively eliminate, pancreatic cancer, melanoma and glioblastoma cancer cells^{24,48,97}. In these studies, H₂O₂ and NO₂⁻ present in CAP-treated liquids play a key role in the induction of cell death in cancer cells. These ROS can further favour the formation of ONOO⁻^{24,48,176}, which has a high potential to induce lipid peroxidation¹⁷⁷. Our findings suggests that the ability of the RONS present in PT-PBS to damage the lipids in the cell membrane increases the MEL permeation and therefore lowers the therapeutic dose of MEL required to exert a cytotoxic effect in cancer cells. Our study demonstrates the synergistic effect of MEL and PT-PBS, i.e., the combined cancer cell cytotoxicity for both A375, MCF7 cell lines and malignant melanoma cancer tumors is larger than the sum of both individual effects of MEL and PT-PBS at the same concentration. This is supported by the calculated combination index (CI) values of 0.4, which indicates synergism. This synergy is attributed to the change in membrane integrity upon peroxidation of the membrane lipids by the RONS present in PT-PBS. As a result of the change in membrane integrity, the MEL translocation rate through the cell membrane increases significantly, as demonstrated by US MD simulations. Hence, MEL will already be able to penetrate inside the cell interior at lower treatment doses. Our results show that this synergy between PT-PBS and MEL has great potential for cancer therapy based on MEL, as it might help to reduce the non-specific toxicity of MEL.

Chapter 6: Protein oxidation: reactive species sensitize chemoresistant cells to lipid peroxidation-induced cell death

This Chapter is published as:

Priyanka Shaw, Naresh Kumar, Claudina Perez-Novo, Emilie Logie, Angela Privat-Maldonado, Sylvia Dewilde, Evelien Smits, Wim Vanden Berghe, Annemie Bogaerts
“Physical plasma-derived oxidants sensitize pancreatic cancer cells to ferroptotic cell death” *Free Radical Biology and Medicine*, 166, p187-200, 2021

6.1 Abstract

The growing number of cancer deaths worldwide demands for new treatment strategies. Recent developments in biomedical applications of physical plasma and plasma-treated liquids have become popular in cancer therapy. Since plasma produces a variety of reactive species, it can provide a reactive environment surrounding the biological target, which promotes membrane lipid peroxidation mediated cancer cell death, also referred to as iron-catalyzed mediated cell death. However, very few evidence has been reported on the role of plasma-derived oxidants in iron-catalyzed non-apoptotic cell death and related molecular mechanisms. In this Chapter, we discovered that treatment by plasma-derived oxidants via plasma-treated water (PTW) induces lipid peroxidation through impairment of the lipid repair enzyme glutathione peroxidase 4 (GPX4)/(GSH), as well as increasing the expression for Heme Oxygenase 1 (HMOX1) *in vitro* and *in ovo*. To support the *in vitro* and *in ovo* experiments, we showed by computer simulations that the oxidation of the catalytic residue of GPX4 assists the elimination of the enzymatic activity of GPX4, which suggests that the impairment of GPX4 by plasma-derived reactive species confers the tumor cell sensitivity to iron-catalyzed cell death.

6.2 Introduction

Pancreatic ductal adenocarcinoma (PDAC), generally known as pancreatic cancer, represents the fourth leading cause of cancer-related deaths in the western world. The incidence of this disease is displaying a rising tendency every year, and the mortality rate has not decreased significantly because of late diagnosis, early metastasis, and poor clinical therapy response¹⁷⁸. It is well known that a major contributor to this poor clinical outcome is the prominent chemoresistance, which is triggered by the resistance of pancreatic cells to undergo apoptosis. Besides, the unique tumor microenvironment where cancer cells cross-talk with pancreatic stellate cells promotes an intrastromal and intratumoral hypoxia cycle impairing drug delivery to cancer cells. This has fueled the search for therapeutic strategies targeting alternative (non-apoptotic) types of programmed cell death, such as necrosis/necroptosis or ferroptosis¹⁷⁹. Cancer cells

exhibit an increased iron demand compared with normal, non-cancer cells to enable growth. This iron dependency can make cancer cells more vulnerable to iron-catalysed necrosis, referred to as ferroptosis. The identification of FDA-approved drugs as ferroptosis inducers creates high expectations towards ferroptosis as a new strategy to kill therapy-resistant cancers¹⁸⁰. The cystine/glutamate antiporter inhibitor erastin was originally described to induce various ferroptosis hallmarks by increasing iron, lipid reactive oxygen species (ROS), and reducing the glutathione synthesis¹⁸⁰⁻¹⁸³. Interestingly, besides chemical ferroptosis induction, plasma treatment was recently also discovered to promote ferroptosis in cancer cells via the reduction of ferritin stored Fe³⁺ to Fe²⁺, lipid peroxidation in the cytoplasm, which thus directly or indirectly indicates that plasma shows similar efficacy to erastin-induced ferroptosis^{184,185}. As explained in earlier Chapters (Chapter 1 and 4), plasma contains a mixture of RONS, such as •OH, O₂•⁻, NO•, NO₂⁻, NO₃⁻ and H₂O₂¹⁸⁶. Accumulation of reactive species surrounding a biological target results in excessive peroxidation of polyunsaturated fatty acids (PUFAs)⁹. These play a key role in regulating non-apoptotic cell death mechanisms, such as ferroptosis characterized by iron-dependent accumulation of lipid peroxides, mainly caused by an impaired redox balance¹⁸⁷. Moreover, RONS induction by plasma-treated liquids (PTLs), e.g., culture media, saline solutions and phosphate buffers, showed promising therapeutic efficacy against drug resistant cancers, such as glioblastomas, lung cancer, leukaemia, melanoma, and pancreatic adenocarcinomas, and have received a growing scientific interest^{9,167,188}.

In the present Chapter, we focus on plasma-treated (deionized) water (PTW), which allows a more reproducible generation of RONS. Indeed, one of the central advantages of plasma-treated deionized water is to reduce the pH value, which supports the generation of highly potent radicals such as (O₂•⁻), (•OH), (ONOO⁻), i.e., either (ONOOH) or (O₂NOOH), (H₂O₂), (NO₂⁻) and (NO₃⁻) ions^{24,189,190}, etc. Among these radicals, •OH and ONOO⁻ directly interact with the cell membrane and cause increased level of Fe²⁺ and lipid peroxidation, which eventually induces ferroptosis through depletion of GSH/GPX4^{9,184,185}. More particularly, ferroptosis sensitization of chemoresistant adenocarcinoma pancreatic cell lines by PTW was studied in *in vitro* and *in ovo* models, and analyzed by *in silico* MD simulations, in relation to the oxidative

degradation of lipids (lipid peroxidation), phospholipid hydroperoxide glutathione peroxidase (GPX4) expression and its regulating redox factors Heme Oxygenase 1 (HMOX1).

6.3 Materials and Methods

Cells lines and treatment with PTW

We used the human adenocarcinoma pancreatic line BxPC-3 (ATCC® CRL-1678) and the ductal human carcinoma cell line (PANC-1, ATCC® CRL-1469). We treated deionized water with physical plasma, yielding so-called PTW, which we applied to the cell lines, as an alternative to direct plasma treatment, with larger applicability for tumors inside the body. The PTW was prepared using the kINPen® IND plasma jet (INP Greifswald/neoplas tools GmbH, Greifswald, Germany), as described previously in [Chapter 5](#)⁹. Briefly, plasma was generated with argon gas with a flow rate of 3 LPM, and we kept a 10 mm distance between the nozzle of the plasma jet device and the liquid surface. The plasma irradiation time onto the liquid was 10 min for all treatments. In our previous study we quantified the level of H₂O₂ and NO₂⁻ in PTW at the same conditions, where we detected H₂O₂/NO₂⁻ concentrations of resp. 1400 μM/125 μM inside the PTW²⁴.

Analysis of cell cytotoxicity and cell death

The cytotoxicity of PTW was evaluated on two pancreatic cancer cell lines: BxPC-3 and PANC-1. BxPC-3 cells were cultured in RPMI supplemented with 10% FBS, 1% non-essential amino acids, 1% glutamine, 1% penicillin (100 IU/ml) and streptomycin (100 mg/ml) (ThermoFisher Scientific, Massachusetts, USA), whereas the PANC-1 cells were maintained in DMEM supplemented with 10% FBS, 1% non-essential amino acids, 1% glutamine, 1% penicillin (100 IU/ml) and streptomycin (100 mg/ml), all from Gibco™ (ThermoFisher Scientific, Massachusetts, USA). After 24 hours, the culture medium was replaced by different percentages of PTW, i.e., 20, 10, and 5%, or with the ferroptosis inducer Erastin (Era) (Sigma-Aldrich, Missouri, USA), at concentrations of 10, 5, 2.5, or 1.2 μM, for another 24 hours. The cell viability was determined by MTT (3-(4,5-dimethylthiazol-2-yl)-2,5-diphenyltetrazolium bromide)

assay (Sigma-Aldrich, Missouri, USA) according to the manufacturer's instructions. The ability of PTW to induce iron-dependent cell death was monitored with the CellTox™ Green Cytotoxicity Assay kit (Promega, Wisconsin, USA) according to the manufacturer's protocol. For this approach, BxPC-3 and PANC-1 cells were stimulated during different time intervals (2, 4, 6 and 8 hours) with 10% PTW alone or in combination with 2 mM of the ROS scavenging agent NAC (N-Acetyl-L-cysteine), the iron chelators, ferroptosis inhibitors Ferrostatin 1 (Fer-1) (Sigma-Aldrich, Missouri, USA), Deferoxamine (DFO) purchased from Abcam (Cambridge, UK), the necroptosis inhibitor Necrostatin-1 (Nec-1) (Sigma-Aldrich, Missouri, USA) and the caspase inhibitor zVAD (Bachem, N-1510) used at 10 µM.

Release of Reactive Oxygen Species (ROS) by cancer cells

PTW at 10% was the optimal concentration selected for further molecular studies, based on IC₅₀ values obtained in the cell viability assay. To measure the release of ROS, both, BxPC-3 and PANC-1 cells were seeded at 1x10⁴ cells/ml in a 96 well plate and stimulated for 12 hours with 10% PTW, with or without the presence of 2 mM of the ROS inhibitor N-Acetyl-L-cysteine (NAC) obtained from Sigma-Aldrich (Missouri, USA). Subsequently, 50 µM of CellROX Green Reagent (ThermoFisher Scientific, Massachusetts, USA) was added and the fluorescence intensities were quantified in real time with an IncuCyte ZOOM® system (Essen Bioscience, Michigan, USA).

Intracellular Fe²⁺ analysis

The cellular Fe²⁺ concentration in PANC-1 and BxPC-3 cell lysates was assessed using an iron colorimetric assay kit from Biovision (K390, Milpitas, California, USA) according to the manufacturer instructions. In this assay, ferric carrier proteins dissociate ferric ions into solution in the presence of acid buffer. After reduction to the ferrous form (Fe²⁺), iron reacts with Ferene S to produce a stable colored complex. The Fe²⁺ concentration was determined by plotting the standard curve (0 to 10 nmol of iron).

Staining of intracellular reactive oxygen species (ROS) & Lipid Peroxidation

For fluorescence imaging of the intracellular release of ROS, cells were first seeded (1×10^5 cells/ml) on cover glasses and incubated at 37°C , 5 % CO_2 for 24 hours. Subsequently, the slides were incubated with 10% PTW alone or in combination with 2 mM NAC and $0.5 \mu\text{M}$ of the ferroptosis inhibitor Fer-1 for 3 hours. Subsequently, ROS intracellular production was detected after incubating for 30 minutes with $50 \mu\text{M}$ of cell-permeant reagent: 2', 7'-dichlorofluorescein diacetates (H2DCFDA, Thermo Fisher Scientific, Massachusetts, USA), and $10 \mu\text{M}$ Image-iT™ Lipid Peroxidation Kit, for live cell analysis (ThermoFisher scientific, Massachusetts, USA). The following step was a 20 min fixation in 4% paraformaldehyde (in PBS) and permeabilization in cytoskeleton buffer (pH 6.8, 50 mM NaCl, 150 Mm sucrose, 3 mM MgCl_2 , 50 mM Trizma-base, 0.5% Triton X-100). After permeabilization, the slides were washed three times with 1X PBS and mounted with ProLong®Gold Antifade Mountant with DAPI (ThermoFisher scientific, Massachusetts, USA). Images were obtained with a Zeiss AxioImager Z1 microscope (Carl Zeiss, Göttingen, Germany) equipped with an AxioCam MR ver.3.0 using a 40X magnification and filters for green fluorescent (GFP), red (Texas Red) and blue fluorescent (DAPI) channels.

Quantification of malondialdehyde (MDA)

To evaluate the formation of the lipid peroxidation product MDA, the BCxP-3 and PANC-1 cells were cultured (1×10^5 cells/ml) at 37°C , 5 % CO_2 for 24 hours. Then, slides were incubated with 10% PTW or $0.5 \mu\text{M}$ of lipid peroxidation inducer Fer-1 for 3 hours. Subsequently, the concentrations of MDA were quantified using the Lipid Peroxidation (MDA) Assay Kit (Sigma-Aldrich, USA) according to the manufacturer's instructions.

Assessment of Glutathione levels

Glutathione (GSH) levels were measured using the Quanti Chrom Glutathione Assay Kit (BioAssay Systems, DIGT-250) according to the manufacturer's protocol. Briefly, the cells were seeded at 2×10^5 cells/ml in a 5-cm dish, and after 24 hours in culture, they were treated with 10% PTW for 3 hours with or without the presence of 4

μM of Fer-1. After stimulation, the cells were collected and centrifuged at 425 g at 4°C for 5 minutes. The cell pellet was resuspended in 1X PBS and lysed by sonication at a frequency of 20 kHz. Subsequently, the lysates were centrifuged at 18,500 g, 4°C for 10 minutes and supernatants were used to determine the GSH concentrations.

GPX Enzyme Activity Assay

GPX enzyme activity was analyzed with a commercialized colorimetric BioVision Glutathione Peroxidase Activity Assay Kit (BioVision, Milpitas, CA). In short, PANC-1 and BxPC-3 cells after stimulation were centrifuged at 10,000 x g for 15 min at 4 °C in 200 μL cold GPX assay buffer, and the assay was performed following the kit protocol. One unit of enzymatic activity is defined as 1.0 μmol of NADPH oxidized to NADP⁺ per minute at 25 °C.

Chicken egg chorioallantoic membrane (CAM) assay

Four-day old fertilized chicken eggs were incubated in a horizontal position for 1 day at 37.7 °C and 65% humidity in an egg incubator with automatic turning function (Ova-Easy 100, Brinsea, Veenendaal, The Netherlands). On day 5, the upper pole was disinfected and pierced with a 20G sterile needle (BD) and sealed with medical tape (Leukosilk S, Covamed Farma BVBA, Marke, Belgium). The eggs were incubated in vertical position (turning function off) to promote the relocation of the air cell. On day 7, the egg shell was cut to expose the chicken chorioallantoic membrane (CAM). A 1 × 1 mm filter paper soaked in diethyl ether (Thermo Fisher Scientific, Massachusetts, USA) was briefly applied on a vascularized region of the CAM and a sterile silicone ring (ID = 5 mm, OD = 6 mm) was placed. A pellet of BxPC-3 cells (2×10^6 cells per egg) was mixed with 15 μL growth reduced factor Matrigel (8.6 mg/mL, Corning, Amsterdam, The Netherlands) and loaded into the ring. The eggs were sealed with Tegaderm (3M) and placed back in the incubator for 4 days. On day 11, the Tegaderm was cut and a sterile plastic ring (ID = 7 mm, OD = 8.5 mm) was placed around the tumor. Subsequently, 100 μL of 10% PTW mixed with PBS and 100 μL of 10% untreated water mixed with PBS were loaded into the ring. The eggs were sealed with Tegaderm and incubated until the end of the experiment. The cytotoxic effect of the treatments was assessed on day 14

when the tumors were excised and weighed in a precision balance (Mettler Toledo, Fisher, Merelbeke, Belgium). All steps outside the incubator were carried out using a heat block (set at 37.7 °C) with a custom-made egg-shaped aluminium adapter.

Assessment of cell proliferation by Ki67 staining

For immunohistochemistry, tumor sections (5 µm), obtained from the CAM assay, were fixed in 4% paraformaldehyde, embedded in paraffin, cut in 5-µm sections and stained with 1:1 hematoxylin and 0.5% eosin solution for histological analysis. For staining with the cell proliferation marker Ki67, antigen retrieval was performed with citrate buffer (10 mM, pH 6), at 96 °C for 20 min. Sections were permeabilised in 0.1% Tween-20 and blocked with 3% H₂O₂ in PBS (10 min, RT) and 2% BSA (30 min, RT). The slides were then incubated with 1:75 dilution of the mouse Anti-Human Ki-67 Antigen (Clone MIB-1, Agilent, Santa Clara, CA, USA) for 40 min at room temperature, followed by incubation with the secondary antibody Envision Flex HRP, Agilent, (Santa Clara, California, USA) during 30 min at room temperature. Diaminobenzidine was used to visualize positive staining and haematoxylin to counterstain.

Immunohistochemistry of GPX4 enzyme

Expression of GXP4 was evaluated in sections from the CAM-solid tumors. The slides were first incubated with blocking buffer (10% Goat serum, 1% BSA in PBS) for 20–30 minutes at room temperature followed by an incubation with 1:1000 dilution of the rabbit- mAb anti-Glutathione peroxidase 4 (ab125066, Abcam, Cambridge, UK), overnight at 4°. Subsequently, the stained slides were washed and incubated with secondary antibody HRP goat anti-rabbit IgG, (Abcam, Cambridge, UK), used at a dilution of 1:500. All sections were subsequently imaged with a Zeiss AxioImager Z1 microscope (Carl Zeiss, Göttingen, Germany) equipped with an AxioCam MR ver.3.0 (Carl Zeiss, Göttingen, Germany).

Immunofluorescence of HMOX1

We performed immunofluorescence assays to evaluate the expression of Heme Oxygenase 1 (HMOX1) in sections from the CAM-solid tumors. After antigen retrieval,

the slides were first incubated with blocking buffer, i.e., 5% BSA in PBS at RT, followed by an incubation with 1:100 dilution of the Anti-Heme Oxygenase 1 (ab68477, Abcam, Cambridge, UK) overnight at 4°C. Subsequently, the stained slides were washed (with 0.05% Triton X-100) and incubated with secondary antibody Alexa fluor 488 (1:1000; cat. no. ab150077, Abcam), at RT for 1 hour. DAPI was used for nuclear counterstain. All sections were subsequently imaged with a Zeiss AxioImager Z1 microscope (Carl Zeiss, Göttingen, Germany) equipped with an AxioCam MR ver.3.0 (Carl Zeiss, Göttingen, Germany).

MD simulations of GPX4 enzyme

We performed MD simulations to elucidate the stability of native and oxidized GPX4 at the molecular level and to determine the underlying mechanisms of physical plasma induced ferroptotic cell death. Simulations were carried out using the GROMACS¹⁹¹ program package (version 5.1.2), applying the GROMOS 54a7 force field¹⁹². The coordinate file (i.e., initial structure) of the human GPX4 was obtained from the Protein Data Bank (PDB ID: 2OBI)¹⁹³.

GPX4 was placed in a triclinic box, spacing the atoms at least 1.5 nm from the boundaries of the simulation box. The box was then filled with water molecules surrounding the GPX4, employing the SPC/E (extended simple point charge) water model and neutralized by Na⁺ and Cl⁻. Periodic boundary conditions were applied in all directions. Prior to the simulation, an energy minimization was performed using the steepest descent integration method. Subsequently, the system was equilibrated for 200 ps of the NVT ensemble (constant number of particles N, volume V, and temperature T). Next, a 500 ns production run was conducted within the NPT ensemble (constant number of particles N, pressure P, and temperature T at 310 K) with periodic boundary conditions. It was verified that the 500 ns production run was sufficient, as the native system reached stability after ~200 ns and it remained stable up to 500ns. The temperature was kept constant by V-rescale thermostat¹³⁰, while the pressure was maintained by 1 bar using a Parrinello-Rahman barostat¹³¹. Electrostatic interactions were calculated using the particle mesh Ewald method and cut-off distances for the calculation of Coulomb and van der Waals interactions were 1.0 nm during the equilibration. Note that multiple

simulations were carried out using a different cut-off radius and force fields, but the cut-off radius of 1.0 nm and GROMOS 54a7 force field were found to provide the most reliable description of the native GPX4.

To describe the oxidative stage of the protein in the MD simulations, we constructed different oxidation states (OX1 and OX2) of the human GPX4 protein, by selectively manipulating amino acid residues to get their corresponding oxidation states using the Vienna-PTM web server¹⁹⁴. The oxidation states were defined as follows: C₄₆ was oxidized to cysteic acid and W₁₃₆ was oxidized to 6-hydroxytryptophan, as previously reported and shown in Table 6.1¹¹⁸. Note that for both oxidized structures (OX1 and OX2) we again repeated the minimization, equilibration and production simulation steps, as mentioned above for the native case. The visualizing tool, PyMOL (Schrodinger, New York, USA) was used for image generation¹⁹⁵.

Statistical analysis

All experiments were performed in at least three independent biological replicates. Bar graphs are represented as the mean \pm S.D (standard deviation). Two groups were compared using Student's t-test with Welch's correction. Pearson's correlation coefficients were computed with a 95% confidence interval. p-values < 0.05 or $p < 0.01$, or $p < 0.001$ were considered statistically significant and labelled with * or ** or ***, respectively, within the graphs as described in the legends. Graphing and statistical analysis were performed using prism 8 (GraphPad software, San Diego, California, USA).

6.4. Results and discussion

PTW induces ferroptotic cell death in pancreatic adenocarcinoma BxPC-3 and PANC-1 cells

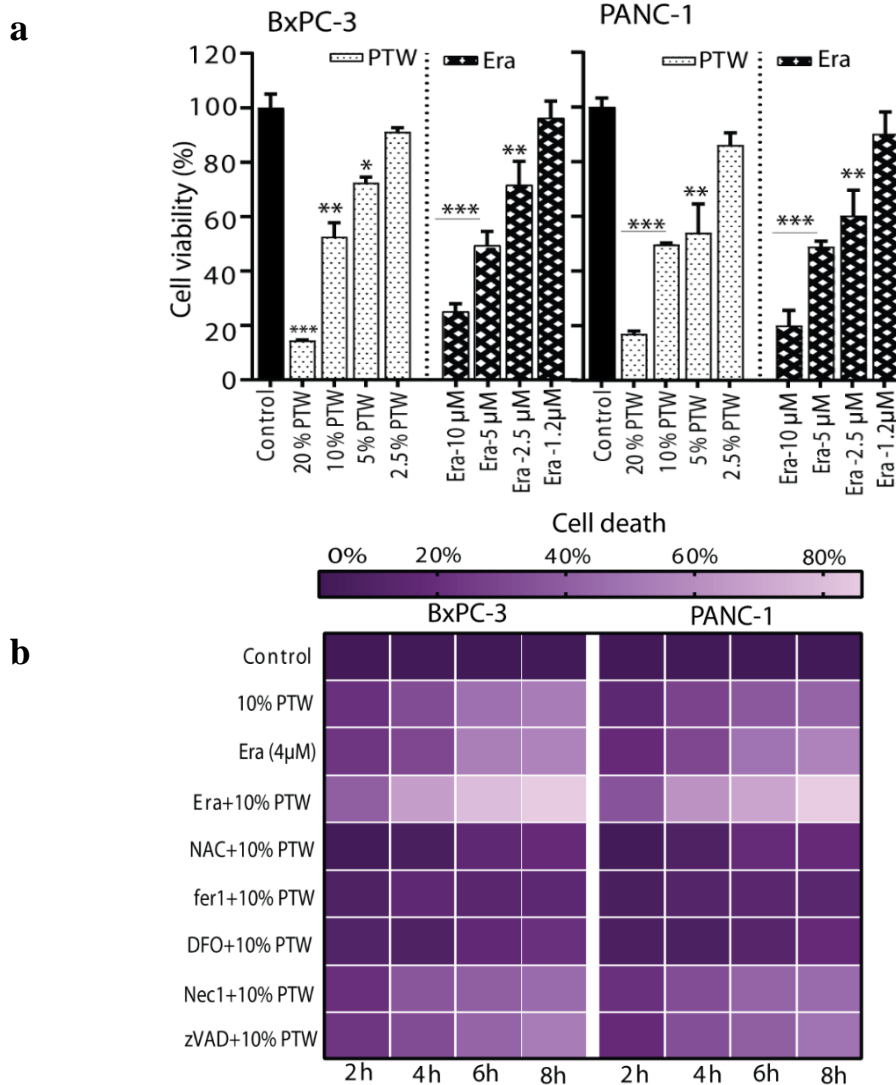


*Figure 6.1. Effect of Plasma-treated water (PTW) on cell viability of BxPC-3 and PANC-1 cells, represented as (a) percentage of viable cells, stimulation with different concentrations of PTW and Era. (b) heat map representing percentage of cell death, after incubation with 10%PTW, Era (4 μM), NAC (2 mM), Fer-1, DFO, Nec-1 (50 μM) and zVAD (10 μM), where * = $p \leq 0.05$, ** = $p \leq 0.01$, *** = $p \leq 0.001$.*

One of the main challenges in cancer research is to effectively kill tumor cells while leaving healthy cells intact. Cancer cells often have defects in their cell survival machinery, helping them to escape from apoptotic cell death pathways, which is one of the main causes of therapy resistance²⁴. To evaluate the potential therapeutic effect of PTW on chemoresistant pancreatic adenocarcinoma BxPC-3 and PANC-1 cancer cells, we measured changes in cell viability and cell death by the MTT and CellTox™ Green cytotoxicity assays, respectively. The MTT assays showed that 24 hours with PTW decreased cell viability in both cell lines in a dose-dependent manner at concentrations of 5%, 10% and 20% PTW (Figure 6.1a).

Furthermore, since PTW is a known inducer of oxidative stress which can promote non-apoptotic ferroptotic cell death¹⁹⁶, we also evaluated sensitivity of pancreatic cancer cells to the ferroptosis inducing chemical Erastin (Era). Similar to PTW treatment, Era also reduced cell viability in a dose-dependent manner with a similar efficacy in a concentration range of 2.5-10 μ M (Figure 6.1a). Upon comparing both dose responses, the BxPC-3 cells revealed similar sensitivity to PTW or Erastin treatment, reaching IC₅₀ values upon 10% PTW or 5 μ M Era treatment, respectively (Figure 6.1a). Similar results were obtained for the PANC-1 pancreatic cancer cells (Figure 6.1b).

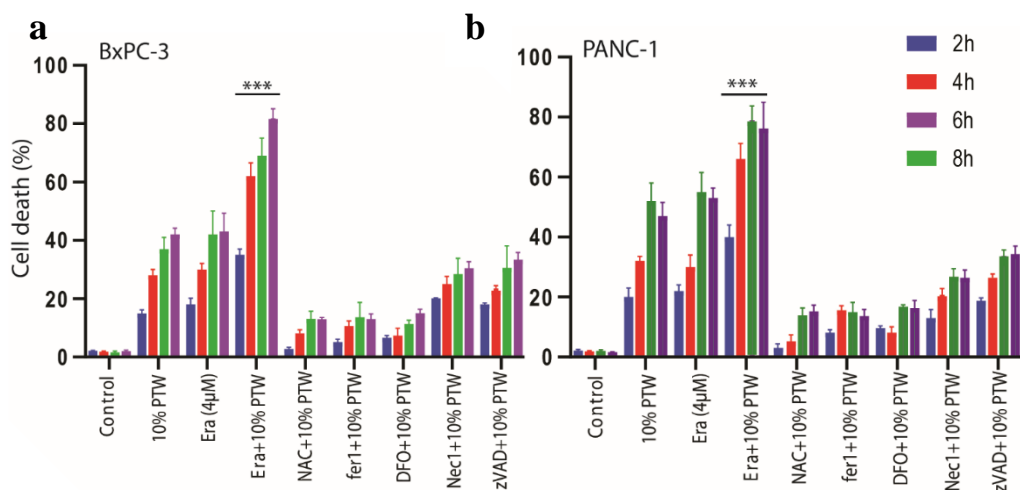
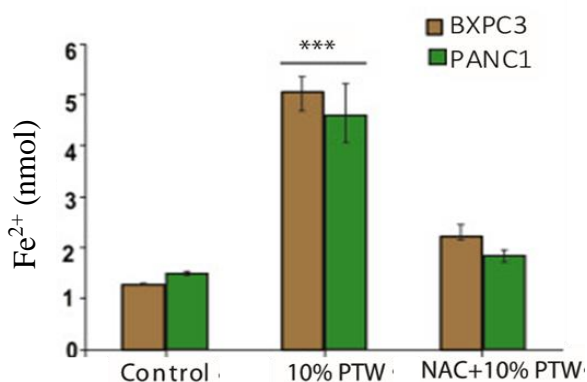


Figure 6.2. Cytotoxic effect of PTW on (a) BxPC-3 and (b) PANC-1 cells, after incubation with 10% PTW, Era (4 μ M), NAC (2 mM), inhibitors Fer-1, DFO, Nec-1(50 μ M) and zVAD (10 μ M), where * = $p \leq 0.05$, ** = $p \leq 0.01$, *** = $p \leq 0.001$.

To confirm the biochemical involvement of ferroptosis in PTW-induced cell death, we further compared single or combination treatments of PTW with the ferroptosis inducer agent Erastin (Era), ROS scavenging agent NAC (N-Acetyl-L-cysteine), the necrosis inhibitor Necrostatin-1 (Nec-1), the ferroptosis inhibitor Ferrostatin (Fer-1), the iron chelator Deferoxamine (DFO) and the general caspase inhibitor N-Benzyloxycarbonyl-Val-Ala-Asp(O-Me) fluoromethyl ketone (zVAD). As shown in Figure 6.2, Erastin (4 μ M) and 10% PTW treatment alone showed intermediate cytotoxic activity after 8h (approx. 40% cell death, close to IC_{50} values) in both cell lines. Interestingly, combination treatment of PTW and Era showed additive toxicity, up to 80% of cell death. In contrast, 10% PTW treatment in the presence of NAC, Fer-1 or DFO nearly completely reduced cytotoxicity from 40 to 10% cell death. In contrast, the necroptosis inhibitor Nec-1 and caspase inhibitor zVAD could only partially attenuate PTW-induced cell death (approx. 30% and 25% cell death respectively). Finally, PTW treatment increased the cellular levels of free Fe^{2+} by more than 2-fold (4.5-5 nM) compared to unstimulated cells, and this effect could not be completely reverted by NAC (Figure 6.3).



*Figure 6.3 Measurement of Fe^{2+} in BxPC-3 and PANC-1 cells upon 10% PTW and NAC treatment, where * = $p \leq 0.05$, ** = $p \leq 0.01$, *** = $p \leq 0.001$.*

Altogether, these results suggest that PTW predominantly elicits ferroptosis, and to a lesser extent, necroptosis mediated cell death. This is of importance since pancreatic cancer cells show relative increased ROS levels as compared to non-malignant cells

(primarily due to their increased metabolism, oncogene activation, and mitochondrial dysfunction) making them more vulnerable to ferroptosis-specific cancer therapies¹⁸⁰.

PTW treatment promotes intracellular ROS production and lipid peroxidation in cells, which can be blocked by the ROS scavenger NAC and the ferroptosis inhibitor ferrostatin

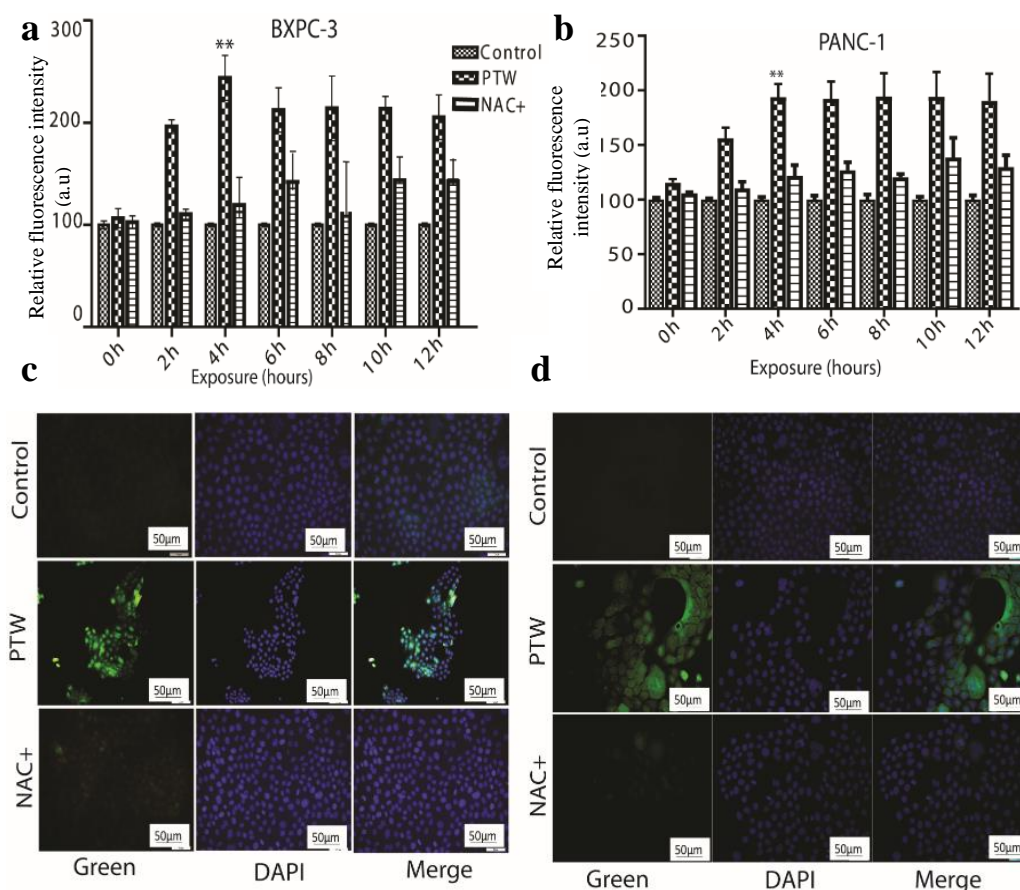


*Figure 6.4 (a & b) real-time release as percentage of ROS in BxPC-3 and PANC-1. (c & d) fluorescence images of positive BxPC-3 and PANC-1 cells stained with the H2DCFDA fluorescent probe. Green fluorescence represents intracellular ROS, DAPI (blue) represents the nuclear counterstain, where * = $p \leq 0.05$, ** = $p \leq 0.01$, *** = $p \leq 0.001$*

Previously, it has been demonstrated that PTW treatment promotes ferroptosis by stimulation of the iron-dependent Fenton reaction to increase intracellular ROS levels and extensive release of malondialdehyde (MDA), one of the final products of

polyunsaturated fatty acid peroxidation^{184,197}. Accordingly, we also characterized the potential effect of RONS released upon PTW treatment on the intracellular ROS levels, by measuring changes in cellular fluorescence intensities of CellROX[®]Green Reagent. This cell-permeable compound dye binds to nuclear and mitochondrial DNA and becomes strongly fluorescent upon oxidation. Treatment with 10% PTW resulted in a higher fluorescence intensity when compared to the signal of untreated cells, whereas the ROS scavenger NAC could reverse the effects in BxPC-3 and PANC-1 cell lines (Figure 6.4a and b). The maximal intensity was significantly increased in treated cells after 4 hours and remained stable for the next 8 hours treatment, as compared to untreated cells.

Similarly, the number of positive fluorescent cells following intracellular staining with the ROS detection probe H2DCFDA, was higher in both (BxPC-3 and PANC-1) cell cultures with PTW treatment than the number observed in untreated or NAC stimulated cells (Figure 6.4c and 6.4d).

Increasing intracellular RONS levels in response to PTW treatment can further propagate lipid peroxidation and cause lethal damage of cancer cells through ferroptosis¹⁸⁵. To evaluate the effect of PTW on lipid peroxidation mechanisms in BxPC-3 and PANC-1 cells, we measured the production of malondialdehyde (MDA), which is one of the final products of polyunsaturated fatty acid peroxidation in cells and an established marker of lipid peroxidation stress. As shown in Figure. 6.5a, the intracellular concentrations of MDA in BxPC-3 cells increased more than two-fold after stimulation with 10% PTW, and about two-fold in PANC-1 cells (Figure 6.6a), and the effect was reversed by Fer-1 in both cell lines.

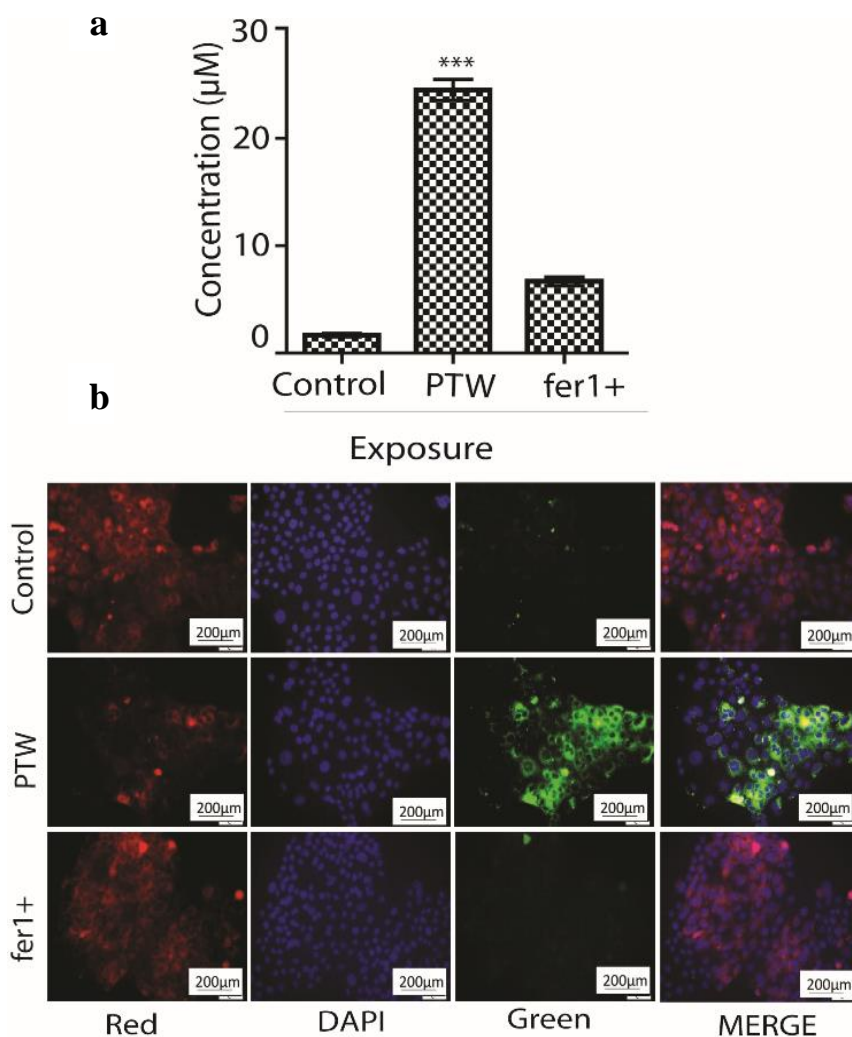


*Figure 6.5 (a) Malondialdehyde (MDA) product after stimulation with 10%-PTW and Fer-1 in BxPC-3 cells, and (b) Fluorescent staining where red fluorescence represents non-oxidized membrane lipids, DAPI (blue) represents the nuclear counterstain and green represents the oxidized membrane lipids in BxPC-3, where * = $p \leq 0.05$, ** = $p \leq 0.01$, *** = $p \leq 0.001$*

Finally, the presence of lipid peroxides was also microscopically confirmed by cellular fluorescent staining with the Image- iT (lipid peroxidation) detection reagents. Figure 6.5b and 6.6b shows that PTW treatment triggers a strong lipid peroxidation/ fluorescent signal near the cell membranes for for both the BxPC-3 and PANC-1 cells, respectively. Again, this could be blocked by Fer-1 in both cell lines. Altogether, these

results suggest that an increase in intracellular ROS levels promotes ferroptosis through increased lipid peroxidation, which can be inhibited in the presence of Fer-1.

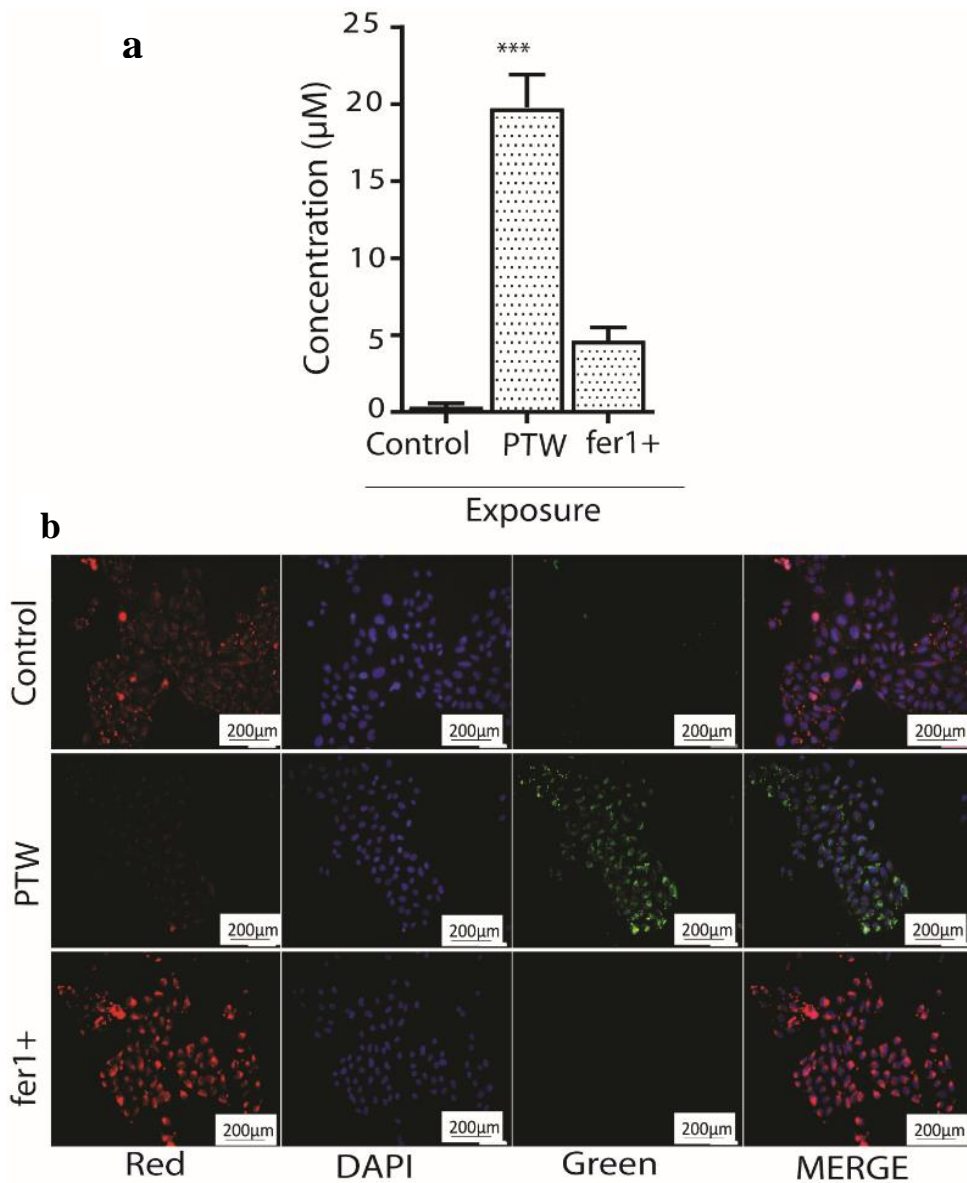


Figure 6.6 (a) Malondialdehyde (MDA) product after stimulation with 10%-PTW and Fer-1 in PANC-1 cells. (b) Fluorescent staining, where red fluorescence represents non-oxidized membrane lipids, DAPI (blue) represents the nuclear counterstain and green represents the oxidized membrane lipids in PANC-1, where $* = p \leq 0.05$, $** = p \leq 0.01$, $*** = p \leq 0.001$

MD simulations demonstrate oxidative destabilization of the GPX4 catalytic domain

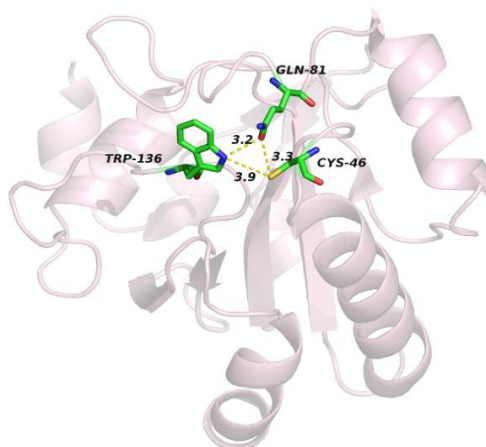


Figure 6.7 Native structure of GPX4 (PDB ID: 2OBI); the catalytic triad is a combination of three amino acid residues: Cys-46, Gln-81, and Trp-136, shown in sticks.

To gain further insight into impairment of GPX4 functions by PTW-induced RONS in response to PTW treatment, we performed MD simulations. This method allows to predict conformational changes in the catalytic active pocket GPX4 upon oxidation. Based on the literature, the active pocket site of GPX4 is located on the solvent accessible surface of the protein, consisting of C₄₆, Q₈₁ and W₁₃₆, also called a catalytic triad (Figure 6.7).

Table 6.2: C α distance between the catalytic triad of amino acids of GPX4 active pocket.

Measurements (nm)	C46 - Q81	C46 - W136	Q81 – W136
Native	0.66±0.06	0.92±0.06	1.05±0.06
OX1	0.68±0.07	1.17±0.09	1.14±0.69
OX2	1.03±0.06	0.94±0.07	1.34±0.08

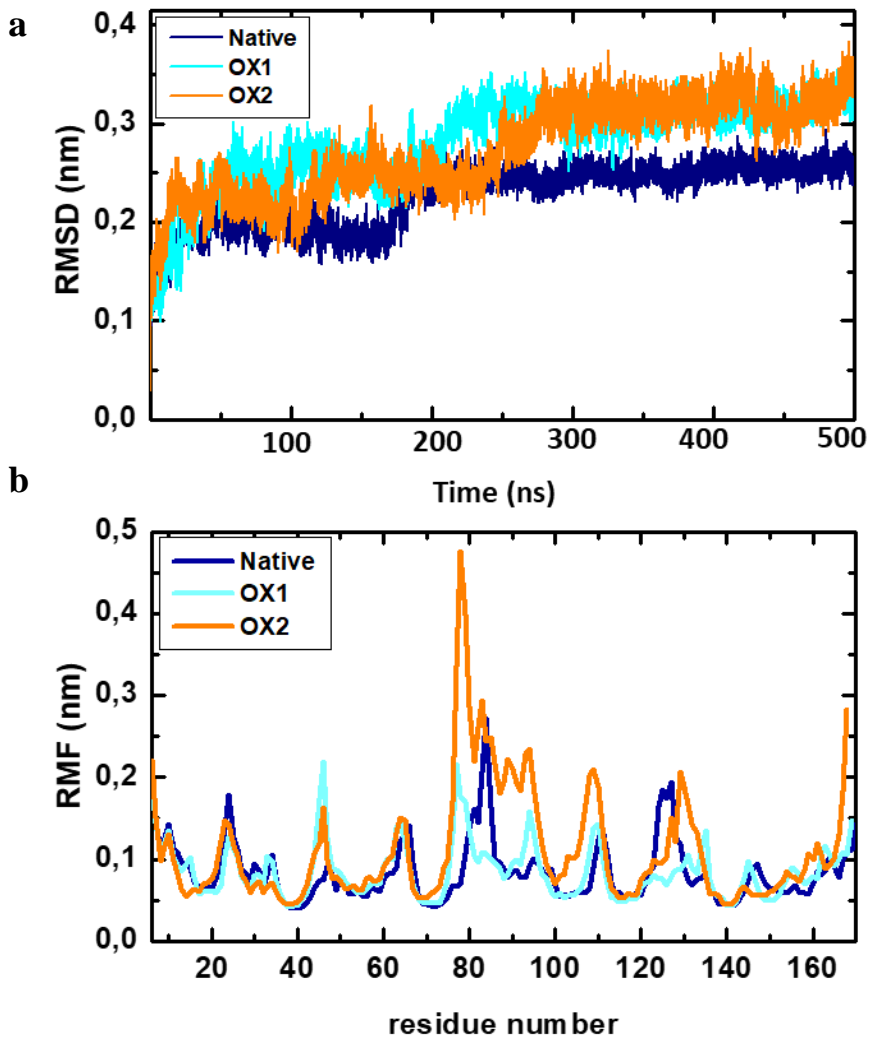
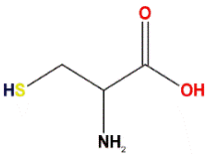
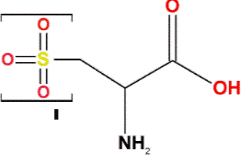
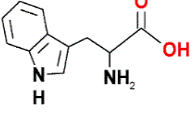
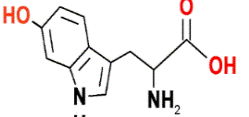


Figure 6.8 (a) RMSD analysis of the backbone of the native, OX1 and OX2 GPX4 structures; (b) RMSF analysis computed on each residue of the GPX4 structures.

In the catalytic triad, Q_{81} and W_{136} are localized at the hydrogen-bond distance to C_{46} , which is a critical determinant of the catalytic activity of GPX4¹⁹³. Furthermore, it has been shown that GPX4 can be oxidized in multiple oxidation states, which might affect the enzymatic activity of GPX4¹⁹⁸. Thus, to determine the effects of oxidation on the arrangements of the catalytic triad upon PTW treatment, three model systems of GPX4 (native, OX1, and OX2) were constructed, where OX1 and OX2 are described as the oxidized structure of GPX4 (Table 6.1). To determine the change in GPX4 structure

upon oxidation, we evaluated the root mean square deviation (RMSD) and root mean square fluctuations (RMSF). As shown in Figure 6.8 a and b, the RMSD of the native protein reaches its stable value after 200 ns and remains more or less constant at about 0.24 nm, whereas the RMSDs of the oxidized structures increase with relatively higher fluctuations (especially in the case of OX2 oxidation) compared to the native GPX4. This indicates that the oxidized structures cannot reach the equilibration state during 500 ns of the simulations. Similarly, the physical plasma-derived oxidant effects on the amino acids of GPX4 proteins were analyzed by measuring the time-averaged RMSF values and plotted against residue numbers based on the last 100 ns trajectory data. It is obvious that oxidation of C₄₆ to cysteic acid and W₁₃₆ to 6-hydroxytryptophan will affect the center of mass of the amino acids. Therefore, we calculated the stable alpha carbon (C α) distance between C₄₆ – Q₈₁, C₄₆ – W₁₃₆ and Q₈₁ – W₁₃₆, as shown in Table 6.2. In general, the movement and rotation of the side chain of cysteic acid and 6-hydroxytryptophan in the oxidized structures results in a rearrangement of the surrounding amino acids, increasing the C α distances among the catalytic machinery of GPX4. Monitoring the C α distances shows that oxidation of the catalytic residues plays a critical role in the stability of GPX4. Specifically, the C α distances among Q₈₁, cysteic acid and 6-hydroxytryptophan are relatively long for making an H-bond between them. This reduced stability may contribute to a decreased expression of GPX4 observed in our study. The averaged C α distance between the catalytic residue pairs are obtained using the "distance" code implemented in GROMACS. Additionally, we measured the RMSD values of native and oxidized systems only on the catalytic amino acids (Figure 6.9) to obtain a deeper insight into the stability of the catalytic machinery of GPX4. The RMSD of the catalytic machinery of GPX4 in the native structure was again found to be more stable in the native case than in the oxidized case. Overall, these MD simulation and experimental results indicate that oxidation of GPX4 leads to a higher dynamic flexibility of catalytic triad, which may reduce the protein stability.

Table 6.1: Modified amino acid residues to create the oxidized GPX4 structures.

Oxidation	Modified AAs in GPX4	Native AA	Oxidized AA
OX1	C46		
OX2	OX1 + W136		

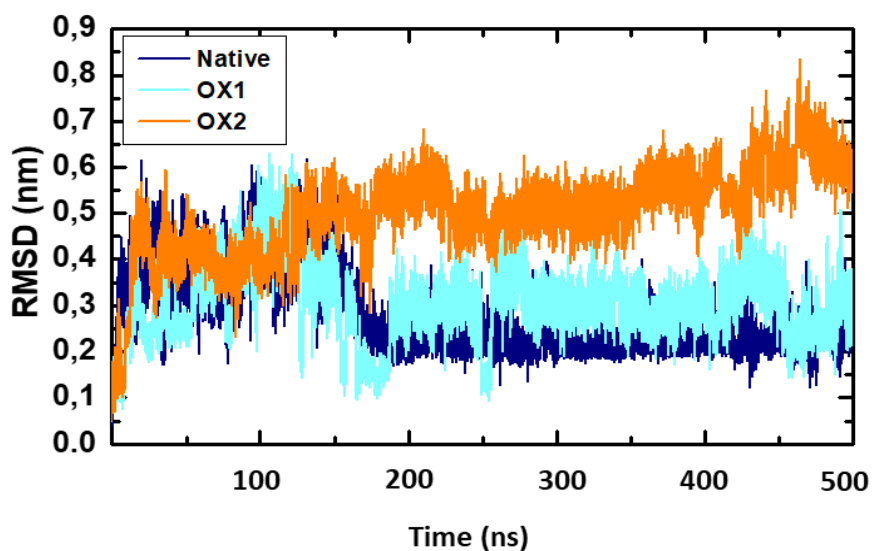


Figure 6.9 RMSD analysis of the catalytic machinery of the native, OX1 and OX2 GPX4's structure during 500 ns.

Next, to experimentally validate the MD simulation results, we measured the cellular changes in enzymatic GPX activity upon 10% PTW treatment in BxPC-3 cells. In line with the molecular modeling results, we observed that PTW treatment

significantly decreased GPX activity (Figure 6.10a). Sequentially, PTW treatment led to the highest decrease in total GSH level. This indicates that all present GSH becomes oxidized after PTW treatment, resulting in an exhaustion of the GSH system (Figure 6.10b).

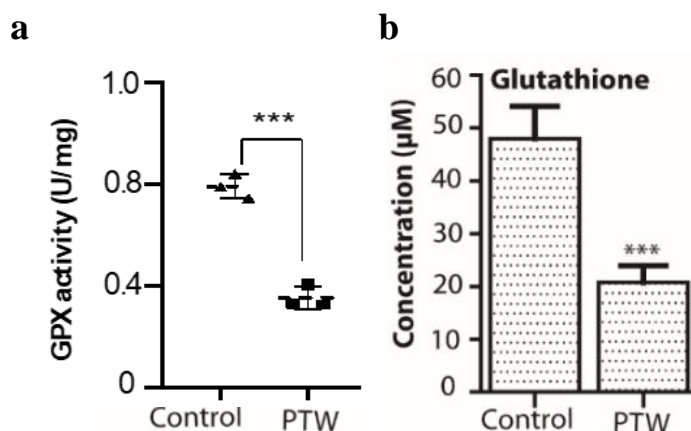


Figure 6.10 (a) GPX enzymatic activity measurement upon PTW, and (b) Cellular levels of glutathione (GSH, where $*$ = $p \leq 0.05$, $**$ = $p \leq 0.01$, $***$ = $p \leq 0.001$).

PTW-dependent decrease in GPX4 contributes to ferroptosis specific antitumor effects of BxPC-3 cells grown ex vivo/in ovo

Finally, we validated the ferroptosis specific therapeutic effects of PTW treatment on BxPC-3 pancreatic cancer tumor cells grown *in ovo* using the CAM assay. After 14 days, tumor sections were analyzed macroscopically by H&E and histochemical staining of the proliferation marker Ki67 (Figure 6.11). The stained tumor sections displayed morphological changes upon PTW treatment, showing cellular shrinking and presence of pyknotic dark small nuclei as a result of chromatin condensation (Figure 6.11a). In contrast, untreated (control) cells presented a more prominent malignant phenotype with mitotic activity (H&E staining, Figure 6.11a). In agreement with the H&E staining analysis of tumor specimens, 10% PTW treatment significantly reduced the tumor weight by approx. 74%, as compared to untreated (control) tumors (Figure 6.11b and Figure 6.11c). To assess the proliferative state of cells in the treated tumors, tissue sections were stained for the proliferation marker Ki-67. We observed that tumors

exposed to PTW treatment presented the lowest number of Ki-67 positive cells as compared to untreated tumors (Figure 6.11d). Further, histological sections from PTW-treated tumors showed reduced immunohistochemical staining for the lipid repair enzyme GPX4 when compared to non-treated tumors, in line with reduced GPX4 expression upon PTW treatment (Figure 6.11e). Finally, to know the contribution of HMOX1 in PTW induced ferroptosis, we also examined histological sections from PTW-treated tumors. We here observed that tumors treated with PTW showed increased expression of HMOX1 as compared to non-treated tumors (Figure 6.12). These results confirm that the PTW-dependent decrease in GPX4 and increase in HMOX1 expression.

contribute to ferroptosis specific antitumor effects of BxPC-3 cells grown *in ovo*.

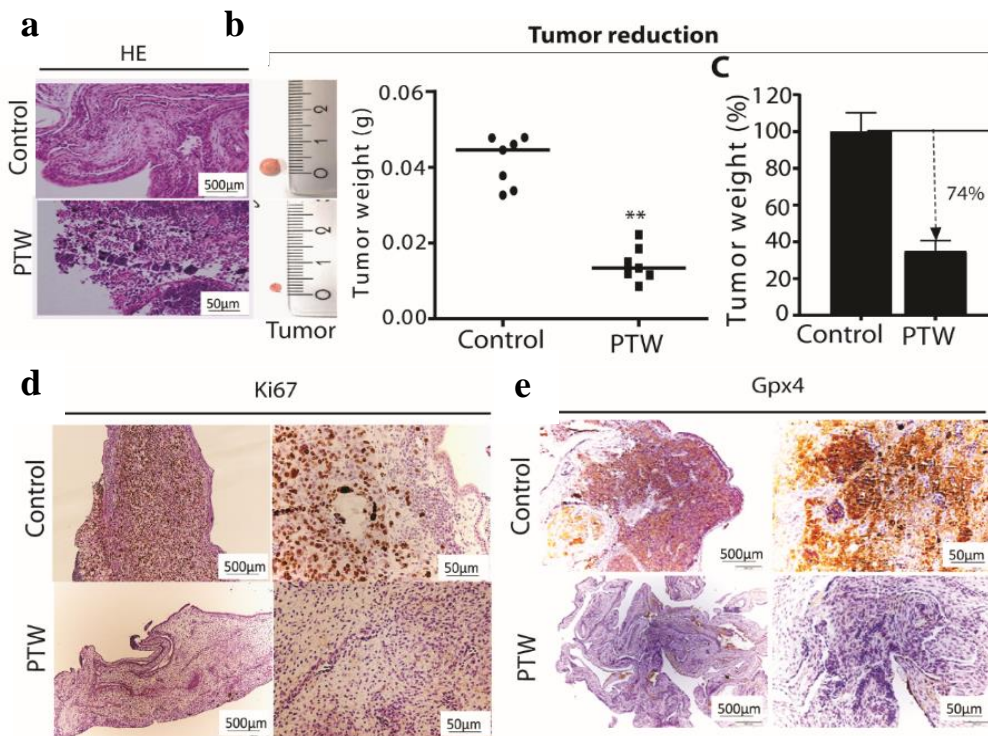


Figure 6.11 Effect of PTW treatment on pancreatic CAM tumor model, showing (a) haematoxylin and eosin staining; (b) weight reduction upon treatments in tumors *in ovo* (each dot represents one tumor); (c) reduction of tumor weight after treatment with 10% PTW (Percentage of tumor weight = weight treated/weight untreated \times 100%); (d and e) histochemical staining showing the reduction of the proliferation marker Ki-67 and GPX4 expression, where $*$ = $p \leq 0.05$, $**$ = $p \leq 0.01$, $***$ = $p \leq 0.001$.

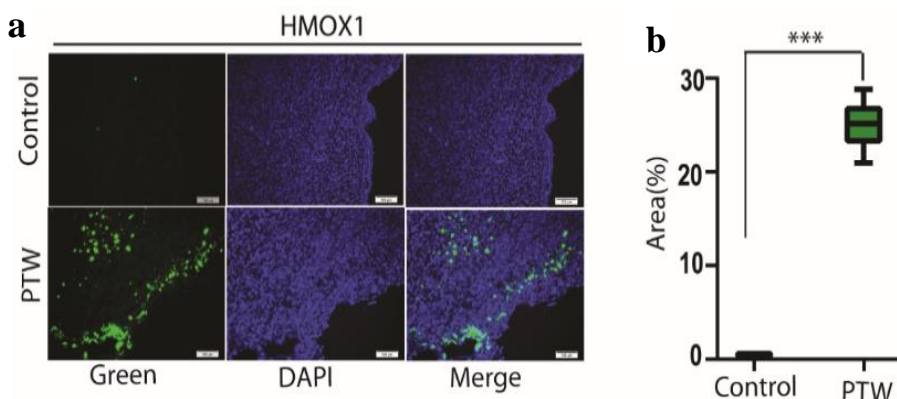


Figure 6.12 (a) Immunofluorescent staining, showing increased HMOX1 expression in tumor tissues after treatment with 10% PTW. Green represents HMOX1 over-expression, blue (DAPI) represents the nuclear counterstain and merge represents combination of green and DAPI. (b) The positive signal of HMOX1 of Figure 6.12a was scored using ImageJ software (treated versus untreated control setup, where * = $p \leq 0.05$, ** = $p \leq 0.01$, *** = $p \leq 0.001$).

6.5. Conclusion

In this Chapter, we discussed a new paradigm in pancreatic cancer treatment for ferroptosis sensitization by PTW treatment. Briefly, plasma-generated RONS (i.e., hydroxyl ($\cdot\text{OH}$) or alkoxy ($\text{RO}\cdot$) radicals) react with cell membrane poly-unsaturated fatty acids (PUFAs) and produce lipid oxidation products, such as PUFAs-OOH, leading to increased vulnerability for ferroptotic cell death. PTW-generated RONS can be converted to H_2O_2 by superoxide dismutase (SOD) on the cell membrane. When H_2O_2 diffuses into the cell, it subsequently yields highly toxic OH radicals in the presence of reduced iron (Fe^{2+}) through the Fenton reaction, which further increases the intracellular ROS pool. Excessive HMOX1 expression/activity induced by PTW-produced ROS leads to accumulation of Fe^{2+} and hydroxyl radicals by the Fenton reaction, resulting in ferroptosis sensitization. Further increase of ROS levels will progressively impair the antioxidant defense and lipid repair mechanisms through the HMOX1-GPX4 ferroptosis axis. In addition, PTW-triggered ROS can oxidize the GPX4 active pocket, leading to enzyme inactivation and impairment of the GPX4/GSH lipid repair system. Altogether, this will propagate a chain of lipid oxidation products, such as PUFAs-OOH, upon

reaction of hydroxyl ($\cdot\text{OH}$) or alkoxyl ($\text{RO}\cdot$) radicals with poly-unsaturated fatty acids (PUFAs)¹⁹⁷. The complete loss of membrane integrity will ultimately result in ferroptotic death of the drug resistant pancreatic cancer cells¹⁹⁹.

Chapter 7: DNA damage: reactive species sensitize cancer cells to chemotherapy drugs due the formation of DNA oxidized compound

This Chapter is published as:

Priyanka Shaw, Naresh Kumar, Angela Privat-Maldonado, Evelien Smits, Annemie Bogaerts “Cold Atmospheric Plasma Increases Temozolomide Sensitivity of Three-Dimensional Glioblastoma Spheroids via Oxidative Stress-Mediated DNA Damage” *Cancers* 13(8), p1780, 2021.

7.1 Abstract

Glioblastoma multiforme (GBM) is the most frequent and aggressive primary malignant brain tumor in adults. Current standard radiotherapy and adjuvant chemotherapy with the alkylating agent temozolomide (TMZ) yield poor clinical outcome. This is due to the stem-like properties of tumor cells and genetic abnormalities in GBM, which contribute to resistance to TMZ and progression. In this Chapter, we used CAP to enhance the sensitivity to TMZ through inhibition of antioxidant signaling (linked to TMZ resistance). We demonstrate that CAP indeed enhances the cytotoxicity of TMZ by targeting the antioxidant specific glutathione (GSH)/glutathione peroxidase 4 (GPX4) signaling. We combined TMZ with CAP and tested it on both TMZ-sensitive (U251, LN18 and LN229) and TMZ-resistant (U87-MG and T98G) cell lines using two-dimensional cell cultures. Subsequently, we used a three-dimensional spheroid model for the U251 (TMZ-sensitive) and U87-MG and T98G (TMZ-resistant) cells. The sensitivity of TMZ was enhanced, i.e., higher cytotoxicity and spheroid shrinkage was obtained when TMZ and CAP were administered together. We attribute the anticancer properties to the release of intracellular reactive oxygen species, through inhibiting the GSH/GPX4 antioxidant machinery, which can lead to DNA damage.

7.2 Introduction

GBM, also called glioblastoma, is the most common cancer malignancy with neuroectodermal origin, showing a considerable variability in age of onset, severity, histological features, and ability to metastasise ²⁰⁰. Currently, TMZ is used as the gold standard chemotherapeutic for the management of GBM among other drugs, i.e., bevacizumab and carmustine ²⁰¹ and it triggers cell-cycle dependent DNA-damage . Unfortunately, the characteristics of GBM significantly contribute to treatment failure and poor outcomes for GBM patients ²⁰² In addition, TMZ has adverse side effects due to the high toxicity and development of resistance over time ^{201,202}. To improve the effect of TMZ, many studies have combined it with radiation, other chemotherapeutic drugs, and phytochemicals, but many patients still develop drug resistance ^{200,203}. Besides, the distinctive tumor microenvironment of GBM stimulates an intrastromal and intratumoral hypoxia cycle, which impairs drug delivery to tumor cells ^{204,205} and involves aberrant

dysregulation of cellular signal transduction pathways^{205,206}. Upon oxidative stress, cells protect themselves via a sophisticated intracellular antioxidant system that involves the regulation of glutathione (GSH)/glutathione peroxidase4 (GPX4)^{205,207}. Cancer cells exhibit increased levels of intracellular ROS due to their hypermetabolism^{208,209}, leading to high expression of aquaporins, NADPH oxidases (NOX) and GPX4 compared to normal cells²¹⁰⁻²¹². Cancer cells use GSH as a substrate to reduce oxidation products and to suppress cell death, which leads to resistance against therapy^{210,211}. An excess of ROS can damage biomembranes and propagate lipid peroxidation chain reactions, and eventually oxidize GSH to GSSG^{206,213}. To maintain cellular redox homeostasis, GSSG is subsequently reduced to GSH by GPX4 and NADPH/H⁺, which balances the levels of oxidative mediators²¹⁴. The reduction and activation of antioxidant-related signaling molecules, such as GSH/GPX4 and nuclear factor erythroid 2-related factor 2 (Nrf2), plays an important role in TMZ resistance, as it can turn the oxidative-mediated response on and off, dependent on the intracellular redox status²¹⁵⁻²¹⁸. High intracellular GSH/GPX4 levels in GBM cells lead to epithelial-mesenchymal transition, which results in tumor progression, metastasis and chemoresistance²¹⁹. A possible solution to TMZ toxicity and resistance could be the combination of TMZ with other drugs or therapies that could modulate the GSH/GPX4 levels²²⁰.

Besides chemotherapeutic drugs, an exogenous source of RONS, such as CAP treatment, in combination with TMZ has been found to inhibit cell growth and induce cell cycle arrest in human GBM cell lines LN18, LN229 and U87-MG *in vitro*²²¹. Moreover, the combination of both treatments can reduce cell migration and increase the expression of surface integrins $\alpha\beta3$ and $\alpha\beta5$ in GBM cell lines¹²⁰.

Recently, our group demonstrated the effect of CAP treatment on 3D human glioblastoma spheroid models, and we found that plasma-generated short-lived and long-lived species, such as $\cdot\text{OH}$, $\text{O}_2^{\cdot-}$, NO_2^- , NO_3^- and H_2O_2 , inhibited spheroid growth and reduced cell migration²²². Other studies have shown the effect of plasma-treated liquids (PTLs), more particularly, plasma-activated phosphate-buffered saline (P-A PBS), sodium chloride 0.9% (P-A NaCl) and culture medium (PTM) on human colorectal (HCT-116) and ovarian cancer (SKOV-3) spheroid models. These studies show that PTL

treatment induced cell death and reduction of spheroid growth²²³⁻²²⁵. However, despite the great interest of these works, none of these studies provided precise information on the plasma-induced cell death mechanisms in a spheroid model, or the role of the antioxidant machinery in human GBM tumor models. Indeed, inhibiting the antioxidant machinery, such as GSH/GPX4, plays an important role to enhance the efficacy of TMZ. Hence, there is no evidence whether CAP can sensitize GBM cells towards TMZ, by inhibiting the antioxidant machinery. Indeed, the only two papers published in literature on the combination of CAP with TMZ^{120,221} only used 2D cell cultures, they did not focus on the cell death mechanisms and the role of the antioxidant machinery, and did not reveal whether CAP can restore the sensitivity of TMZ-resistant GBM in 3D tumor-like tissues.

In the present Chapter, we therefore focus on the combined CAP and TMZ treatment of both TMZ-sensitive and TMZ-resistant GBM spheroids, which provide a more complex tumor microenvironment than cell monolayers. We determined the role of plasma-generated RONS in the induction of oxidative stress-mediated cell death in GBM cells by studying the depletion of intracellular GSH/GPX4 and corresponding DNA damage.

7.3 Materials and Methods

Cell lines

We obtained the human glioblastoma (GBM) cell lines (U251, LN18, LN229, U87-MG and T98G) from the Cell Line Service GmbH. All cells were cultured in DMEM supplemented with 10% FBS, 1% glutamine, 1% penicillin (100 IU/ml) and streptomycin (100 mg/ml), all from Gibco™ (ThermoFisher Scientific, Massachusetts, USA). Cell cultures were maintained in a 5% CO₂ environment at 37 °C, with 95% relative humidity. After thawing the cells, they were passaged 2-3 times to reach their regular growth rate prior to experiments. The cells U251 (passage 55+21), LN18 (passage 6), LN229 (passage 20), U87-MG (passage 32+9) and T98G (passage 15) were grown as monolayer cultures, allowed to adhere and maintained to approximately 90% confluency. In addition, cells are regularly tested for the absence of mycoplasma contamination using the MycoAlert detection kit (Lonza). In general, the cells were kept in culture for 4-5

weeks and after that, a new vial of cells were thawed. Additionally, cells were transduced with the Nuclight Red Lentivirus reagent (Essen Biosciences, Ann Arbor, MI, USA) using their standard transduction protocol.

Indirect plasma treatment and TMZ treatment of 2D GBM cell lines

We treated phosphate buffered saline (PBS) using the kINPen® IND plasma jet (INP Greifswald/neoplas tools GmbH, Greifswald, Germany), as described previously^{9,24}. The cells were grown until they reached confluency and 2×10^5 cells/ml were seeded into a flat bottom 96-well plate. The following day, we replaced the culture medium by different percentages of plasma-treated PBS (PT-PBS), i.e., 200 μ L cell culture media containing 20, 10, 5, 2.5 and 1.2% phosphate buffer saline (PBS), or with the standard GBM treatment chemotherapy drug TMZ (Sigma-Aldrich, Missouri, USA). TMZ was resuspended at 20 mg/mL in 100% DMSO, aliquoted and stored at -20 °C at a concentration of 100 mM.

IC₅₀ estimation

We determined the cell viability on the monolayers of all five GBM cell lines by the MTT (3-(4,5-dimethylthiazol-2-yl)-2,5-diphenyltetrazolium bromide) assay (Sigma-Aldrich, Missouri, USA), according to the manufacturer's instructions. All five GBM cell lines were stimulated for up to 24 hours with different percentages of PT-PBS and different concentrations of TMZ (as described above) to determine the IC₅₀ value for each treatment. Subsequently, we combined the optimized doses of the single treatments (PT-PBS and TMZ) i.e., the cells are exposed to PT-PBS and TMZ simultaneously.

Combination Index

To determine the synergistic cytotoxic effect of the combination of TMZ and PT-PBS in all five GBM cell lines, the combination index (CI) value was calculated based on²²⁶. In general, CI values < 0.1 indicate very strong synergism, CI = 0.1–0.3 strong synergism, CI = 0.3–0.7 synergism, CI = 0.7–0.9 slight synergism and CI = 0.9–1.1 nearly additive, while CI = 1.1–1.45 refers to slight to moderate antagonism^{226,227}.

Spheroid Formation

We used a non-adherent technique for the formation of spheroids²²². Briefly, cell suspensions were prepared in culture medium supplemented with 0.24% methyl-cellulose in DMEM to enhance spheroid formation. Methyl-cellulose was prepared as previously described^{222,228}. 100 μ L of cell suspension (5000 cells/well) were seeded in ultra-low attachment (ULA) 96-well plates (round bottom, Corning Costar, Corning, NY, USA) and centrifuged for 10 min at 1000 rpm. The plates were incubated at 37 °C in a 5% CO₂ humidified atmosphere and spheroids were formed for 3 days.

Indirect and direct plasma treatments, in combination with TMZ, of the 3D spheroids

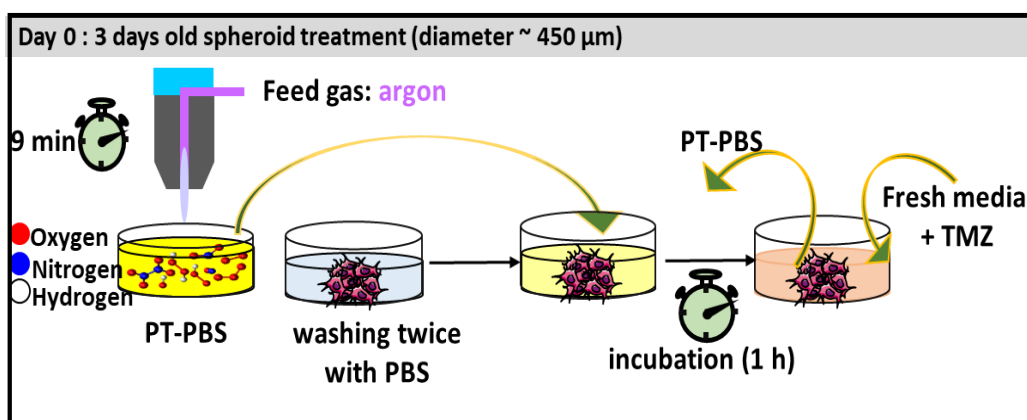


Figure 7.1 Schematic presentation of the indirect treatment setup.

After determining the optimal doses, we investigated the effect of these doses on the 3D spheroid model. Before treatment, three-day-old spheroids were washed twice with PBS to remove the culture medium. For the indirect treatment (Figure 7.1), PBS was first treated with the kINPen plasma jet and then transferred to the spheroids. More specifically, 200 μ L of PT-PBS was applied and the plate was placed in the incubator (37 °C, 5% CO₂) for 1 hour. After this, fresh warm complete culture medium containing TMZ was added to each well. In our 2D cell cultures, we replaced the culture medium by different percentages of plasma-treated PBS (PT-PBS), i.e., 200 μ L cell culture medium containing 20, 10, 5, 2.5 and 1.2% phosphate buffer saline (PBS). The cells were stimulated for up to 24 hours because they start to die after 4-5 hours of treatment and up

to 24 hours almost 80 to 90% of the cells were dead in the PT-PBS + TMZ combination. we followed a protocol based on our previous work⁹. In case of indirect treatment (by the kINPen) of the 3D spheroids, the PT-PBS together with TMZ have no effect on the reduction of tumor size.

Therefore, we incubate the spheroids first with PT-PBS for 1 hr and then we add TMZ together with fresh medium. Also in that case, our experiments revealed that indirect treatment by the kINPen plasma jet was not strong enough to induce significant reduction of the tumor size or cell death in the spheroids. Moreover, longer treatment times could increase the stress in cells due to lack of nutrients and growth factors, which could bias the results on cell death assessed. To monitor cell viability in spheroids for 7-days it is important to replace the PBS with culture medium immediately after the treatment. Thus, in the next experiments, the spheroids were subjected to direct plasma treatment (Figure 7.2). We found that direct treatment by the kINPen plasma jet disturbed the spheroid stability due to the high flow rate of argon gas during plasma generation. Thus, we applied a softer plasma jet device, i.e., the COST plasma jet, to the wells containing the spheroids in 200 μ L PBS^{119,222,229}. Briefly, the plasma was sustained at 250 V_{RMS} and an operating frequency of 13.56 MHz. It was operated with a feed gas of 1 LPM He with 5% H₂O vapour admixture achieved by passing part of the He through an H₂O-filled Drechsel flask. As reported previously by our group, the administration of H₂O vapour helps to generate a higher amount of RONS²²². The spheroids, contained in 200 μ L of PBS in ULA plate, were exposed to a single CAP treatment with the COST jet for 3 min, or to TMZ alone at 40 μ M for U251 and 72 μ M for U87-MG and T98G (optimized dosage from the IC₅₀ value as described below) or the combination of both (CAP for 3 min + TMZ, 40 μ M for U251 and 72 μ M for U87-MG and T98G). Spheroids in 200 μ L of untreated PBS were used as negative controls. We kept untreated spheroids in untreated PBS (“vehicle” solution) for the same period of time as the spheroids treated with plasma/TMZ. The PBS used in this case was not treated with plasma, serving as a negative “vehicle” control for our experiments. After the direct plasma treatment, spheroids remained in the treated solution and were incubated for 60 min. For the direct treatment of the spheroids with the COST plasma jet, we also incubated the spheroids

first with PT-PBS for an hour and then TMZ was added with fresh culture medium. More specifically, 200 μL of PT-PBS was applied per spheroid and the plate was placed in the incubator ($37\text{ }^{\circ}\text{C}$, 5% CO_2) for 1h by following our standard protocol⁹⁷ (Figure 7.2). In this case, the incubation time was chosen based on the time it takes to treat a whole plate (around 50-60 min) for a single cell line with all conditions. By the end of treatment, the first treated spheroids had already spent about 50-60 min in the plasma-treated solution. For this reason, we have considered 1 hr incubation for all spheroids with PT-PBS, after which it was replaced with medium at this corresponding time and TMZ was immediately added for the assessment of combinational treatments. Longer treatment times with PT-PBS (more than 60 min) could increase the stress in cells due to lack of nutrients and growth factors could affect the spheroid growth. After this period, the solution was replaced with complete warm, fresh medium containing TMZ prepared according to the downstream experiment. The RONS present in COST jet have been previously described⁹⁷. This study revealed that H_2O_2 , NO_2^- and NO_3^- are the main RONS presented in the PT-PBS and responsible for the biological effects, and their concentrations for the same conditions as used in this paper were measured to be 1200 μM , 5 μM , and 6 μM , respectively. This is different than for the PT-PBS treated by the kINPen (see above), and can explain why the PT-PBS produced by the COST jet is more effective for the spheroids.

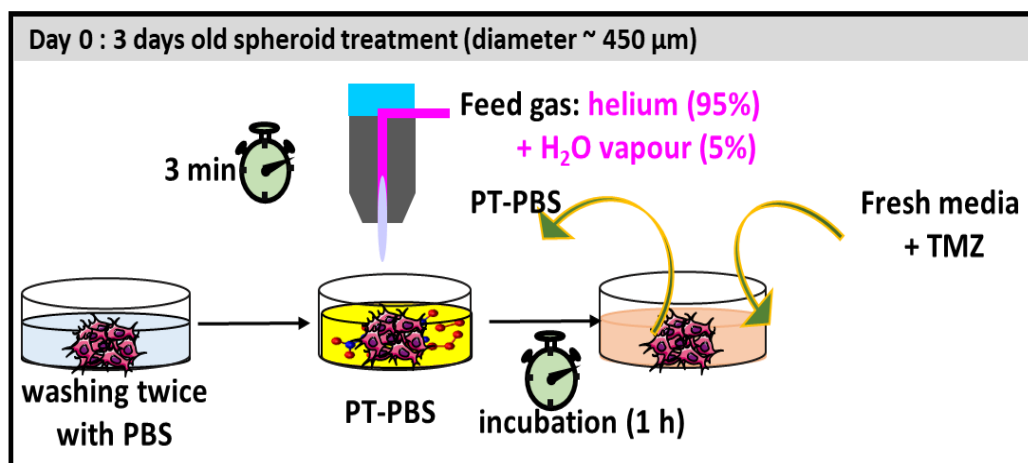


Figure 7.2 Schematic presentation of the direct treatment setup.

Cytotoxicity Assay

We used the Cytotox Green reagent (50 nM, Essen Biosciences) for real-time quantification of cell death. This cell-permeable compound dye binds to nuclear and mitochondrial DNA and becomes strongly fluorescent upon oxidation. The plates were incubated in the IncuCyte Live-Cell Analysis System (Sartorius, Ann Arbor, MI, USA) and spheroid growth was followed during seven days after treatment. Data were analysed with the IncuCyte ZOOM version 2016B (Essen BioScience) as well as ImageJ software to collect the following metrics: (1) spheroid core area, corresponding to the proliferative region only (red live cells; calculated by drawing a circle at the edge of the bright red core of the spheroid using ImageJ); (2) total spheroid area, corresponding to the combined viable, proliferative spheroid core and the Cytotox Green⁺ region (total spheroid region measured from phase contrast images); and (3) the amount of Cytotox Green⁺ in treated spheroids (confluence percentage of the image area occupied by green objects using ImageJ software) normalized to the untreated control at each time point, representing the cytotoxic effect of the treatment.

Estimation of intracellular reactive oxygen species (ROS) levels

To measure the release of intracellular ROS in the spheroids, we used CellROX Green Reagent (Thermo Fisher Scientific, Massachusetts, USA). CellROX is a DNA-binding cell-permeant dye and exhibits bright green photostable fluorescence upon oxidation by reactive oxygen species. We followed the incorporation of the fluorescent probe by the spheroids over a period of 24 hours, following CAP, TMZ alone and the combined treatment, with or without the presence of the ROS inhibitor, with a pre-incubation of 1 h for N-Acetyl-cysteine (NAC, 2.5 μ M, Sigma-Aldrich (Missouri, USA)). 60 min after treatment, we added the culture medium containing 2.5 μ M CellROX Green reagent. We analyzed the green fluorescence with the IncuCyte ZOOM software.

Assessment of Glutathione levels and 8-hydroxy-2'-deoxyguanosine levels

24 hours post treatments, we washed the spheroids twice with PBS and incubated them in 50 μ L TrypLE express reagent (12604-021, Life Technologies Europe B.V.) for 15 min at 37°C in a 96-well plate. Immediately after, we added fresh warm culture

medium and we dissociated the spheroids with gentle mechanical force using a Pasteur pipette. After the cells were centrifuged at 1000 rpm up to 3 min, we measured the glutathione (GSH) and 8-hydroxy-2'-deoxyguanosine (8-OHdG) levels. We quantified the total GSH and genomic DNA in 10^4 cells from dissociated spheroids. We measured the GSH level using a luminescence-based assay (Promega, USA) following a standard molecular biology protocol^{22,23}. We used the genomic DNA extracted from the same number of tumor cells for the detection of the 8-OHdG level using an oxidative DNA damage ELISA kit (Cell Biolabs, inc. USA).

Immunohistochemical analysis for Ki-67

We collected the spheroids 24 hours after treatment and fixed them with 4% paraformaldehyde for 24 hours at 4 °C. We transferred the fixed spheroids to a 4% agarose mold as described before²²². The agarose pads were embedded in paraffin, and cut in 5- μ m sections. For staining with the cell proliferation marker Ki-67, antigen retrieval was performed with citrate buffer (10 mM, pH 6), at 96 °C for 20 min. Sections were permeabilised in 0.1% Tween-20 and blocked with EnVision FLEX peroxidase blocking reagent (Dako, SM842) for 10 min at room temperature (RT). The slides were then incubated with 1:75 dilution of the mouse Anti-Human Ki-67 Antigen (Clone MIB-1, Agilent, Santa Clara, CA, USA) for 40 min at RT. The samples were then incubated with the secondary antibody Envision Flex HRP, Agilent (Santa Clara, California, USA) for 30 min at RT. Chromogen (substrate) DAB (9511, CINtec histology, Germany) was added to reveal the reaction. Haematoxylin was used to counter stain. The sections were imaged with Zeiss AxioImager Z1 microscope (Carl Zeiss, Göttingen, Germany) equipped with an AxioCam MR ver.3.0. The number of ki67⁺ and haematoxylin⁺ cells was counted using ImageJ software. %ki67⁺ cells = (number ki67⁺ cells/number haematoxylin⁺cells)*100%.

Immunohistochemistry of GPX4 enzyme and 8-Oxo-2'-deoxyguanosine

We evaluated the expression of GXP4 and 8-Oxo-2'-deoxyguanosine (8-oxo-dG) in sections from the spheroid tumors. The slides were first incubated with blocking buffer, i.e., 5% BSA in PBS for 8-oxo-dG (incubated for 2h) and EnVision FLEX

peroxidase blocking reagent (Dako, SM842) for GPX4 (incubated for 10 min) at RT, followed by an incubation with the rabbit- mAb anti-Glutathione peroxidase 4 (1:200; ab125066, Abcam, Cambridge, UK) and anti-8-oxo-dG (1:50; 206461 Abcam), overnight at 4°. Subsequently, the stained slides were washed with 0.05% TritonX-100 for 8-oxo-dG and 0.1% Tween-20 for GPX4. The slides for 8-oxo-dG staining were incubated with Alexa Fluor 488 secondary antibody (1:500; ab150113, Abcam) at RT for 1 hour and the slides with GPX4 staining were incubated with the secondary antibody Envision Flex HRP, Agilent (Santa Clara, California, USA) for 30 min at RT. All sections were subsequently imaged with a Zeiss AxioImager Z1 microscope (Carl Zeiss, Göttingen, Germany) equipped with an AxioCam MR ver.3.0 (Carl Zeiss, Göttingen, Germany). The mean percentage area was counted using ImageJ software.

Statistical analysis

All experiments were performed in at least three independent biological replicates and are shown as mean \pm standard error of the mean (SEM). Statistical analysis was performed by one-way analysis of variance (ANOVA) with Tukey's comparison analysis. The data were considered statistically significant when * = $p \leq 0.05$; ** = $p \leq 0.01$; *** = $p \leq 0.001$, p-values for individual treatments are compared to untreated controls.

7.4. Results

PT-PBS effectively enhances the activity of TMZ in 2D cell cultures

In this study, we used PBS as plasma-treated liquid (PTL) because PBS prevents cells rupturing or shrivelling up due to osmosis. The anticancer effects of other PTL such as NaCl or plasma-treated media have been studied as well ^{121,122,230,231}. However, plasma can change the acidity of NaCl solutions, decreasing the stability of soluble RONS ²³⁰. We believe PT-PBS might be more suitable for practical applications in a clinical setting than (commonly used) plasma-treated media or NaCl ²²³, because of its higher stability of RONS ²³². Indeed, PBS and other phosphate buffers are used to generate PTL due to their buffering properties that control the acidification during or after plasma exposure ^{121,122}. Moreover, the components present in PBS enhance the membrane

electropermeabilisation²³³ by decreasing the phospholipid free energy barrier, which favors the transfer of PT-PBS radicals into the cell and cause oxidative stress that mediates cell death. For instance, Grisetti et al. has shown that PT-PBS induced a fast-occurring and more pronounced cell death, visible within deeper layers of the 3D spheroid models (25).

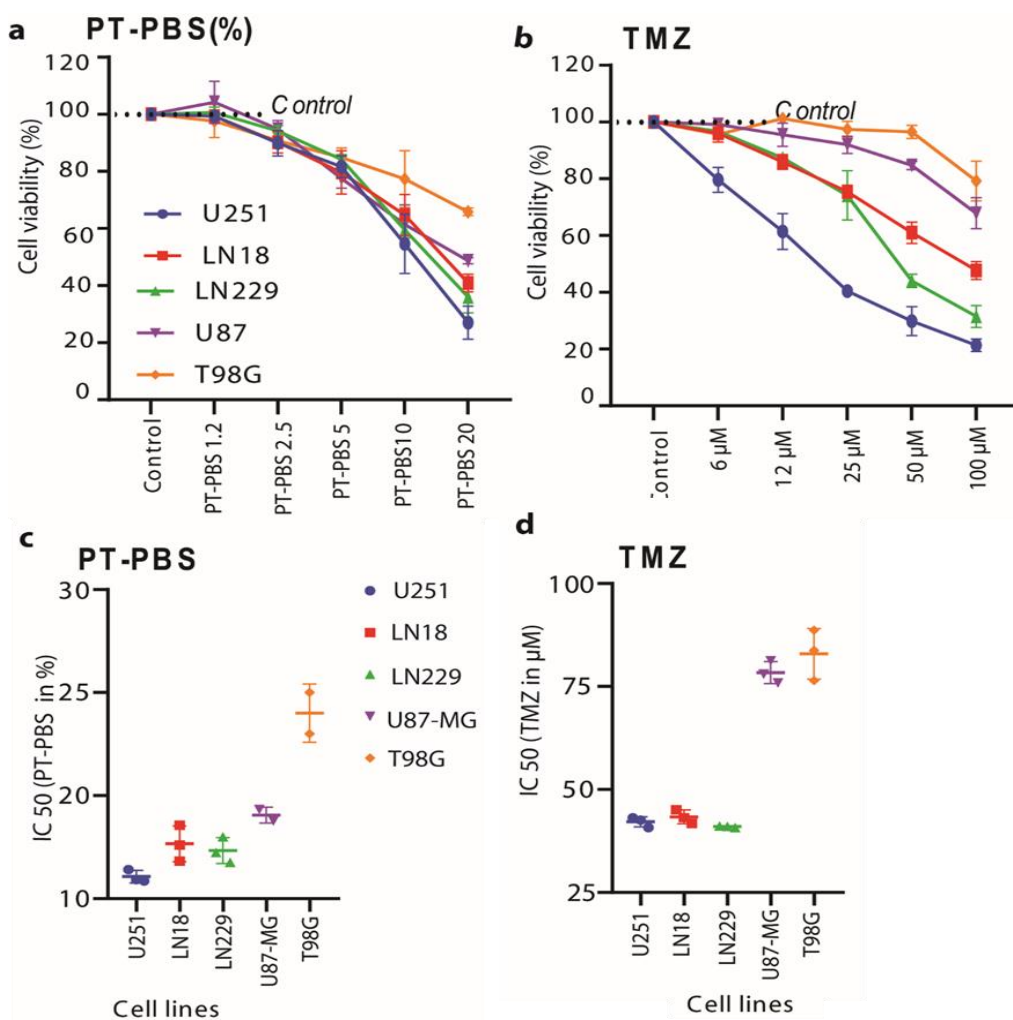


Figure 7.3 Cell cytotoxicity at different doses of (a) PT-PBS (the values in the x-axis are in %) and (b) TMZ, on U251, LN18 and LN229 (TMZ-sensitive) and U87-MG and T98G (TMZ-resistant) cell lines after 24 h incubation. Half maximal inhibitory concentration (IC50) values of (c) PT-PBS and (d) TMZ, where * = $p \leq 0.05$, ** = $p \leq 0.01$, *** = $p \leq 0.001$.

We used the U251, LN18, LN229, U87-MG and T98G cell lines. We analyzed the cytotoxic effect of PT-PBS alone, TMZ alone and its combination, on all five GBM monolayer cell cultures with the MTT assay. 24 hours incubation with PT-PBS decreased the cell viability in all GBM cell lines in a dose-dependent manner, in a concentration range of 1.2 – 20 % PT-PBS in 200 μ L culture medium (Figure 7.3a). The same applies to TMZ treatment in a concentration range of 6-100 μ M added to cells in 200 μ L culture medium (Figure 7.3b).

U87-MG and T98G cells were less sensitive to TMZ than the other three cell lines (Figure 7.3b). Upon comparing both dose responses, the U251, LN18, and LN229 cells revealed similar sensitivity to PT-PBS or TMZ treatment, with IC_{50} values of 12% PT-PBS or 45 μ M TMZ treatment (Figure 7.3 c and d). The U87-MG and T98G cells treated with PT-PBS or TMZ presented slightly higher IC_{50} values of 18% PT-PBS for U87-MG and 24% for T98G, and approx. 80 μ M TMZ for both cell lines (Figure 7.3 c and d). As controls, we used 10% non-treated PBS in the culture media for all GBM cells. We observed slight cell death in case of 20 % untreated PBS, but in 10% untreated PBS there was no cell death observed. The DMSO concentration in all the TMZ, plasma, and combined plasma + TMZ treatments was maintained at 0.25% for all experiments. These results show that U251, LN18 and LN229 are sensitive to both treatments. In contrast, U87-MG is resistant only to TMZ, while T98G is resistant to TMZ, as well as to PT-PBS at lower doses. Additionally, the dose response cytotoxicity curve, as well as the IC_{50} values of TMZ and PT-PBS monotherapy (Figure 7.3 a-d) showed that U251 (IC_{50} = 38.1 μ M), LN18 (IC_{50} = 45 μ M), and LN229 (IC_{50} = 39 μ M) were more sensitive to low concentrations of TMZ. In contrast, U87-MG (IC_{50} = 78 μ M) and T98G (IC_{50} = 80 μ M) required higher concentrations of TMZ to evoke the same cytotoxic response. This is in good agreement with literature^{203,234}. Based on these results, we have categorized these five GBM cell lines into two groups: TMZ-resistant (IC_{50} value > 50 μ M) and TMZ-sensitive (IC_{50} value < 50 μ M). From here on, we will use these terms to refer to these cell lines in this study.

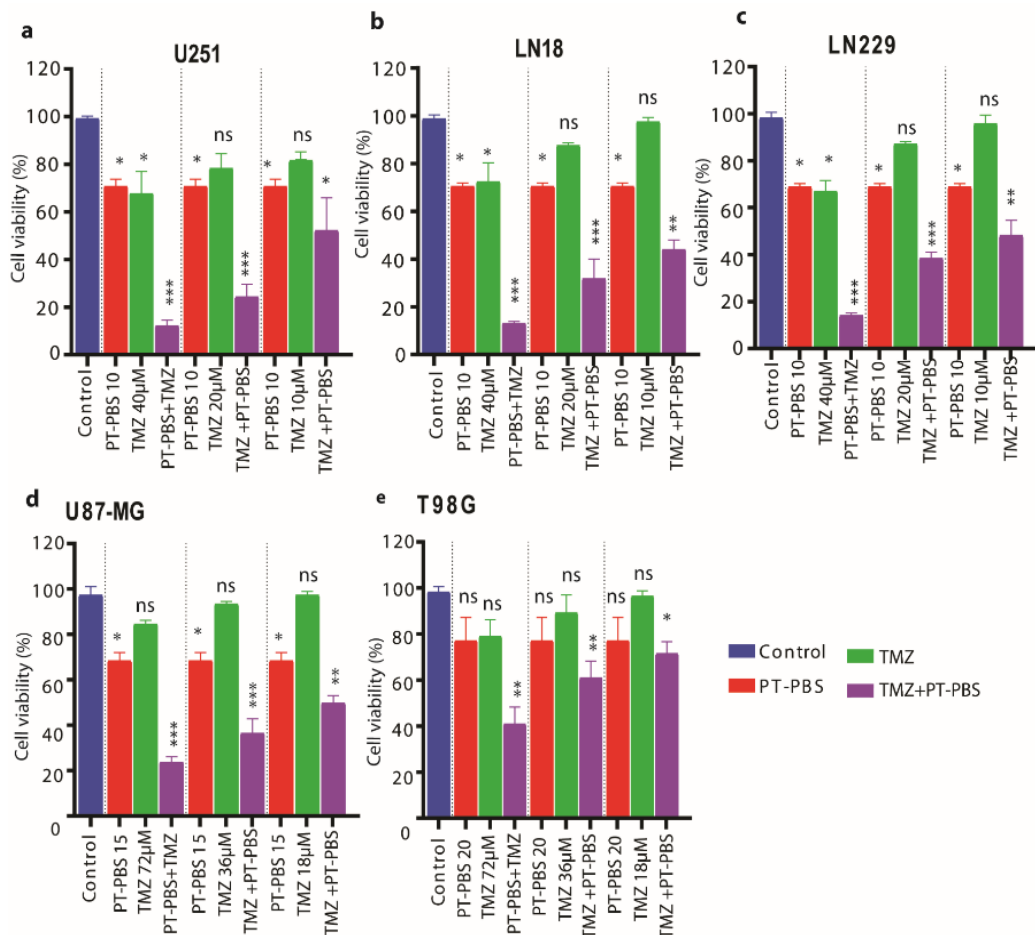


Figure 7.4 Cell viability at a fixed dose of PT-PBS (10%), and varying doses of TMZ (i.e., 40 μ M, 20 μ M and 10 μ M) alone and in combination, for TMZ-sensitive cells, i.e., (a) U251, (b) LN18, and (c) LN229. For PT-PBS (at 15 or 20%) and varying doses of TMZ (i.e., 72 μ M, 36 μ M and 18 μ M) alone and in combination, for TMZ-resistant cells, i.e., (d) U87-MG and (e) T98G, after 24 h incubation, where * = $p \leq 0.05$, ** = $p \leq 0.01$, *** = $p \leq 0.001$.

After determining the IC_{50} values for PT-PBS and TMZ, we further compared the cytotoxicity of single or combination treatments of PT-PBS with TMZ. We selected a slightly lower concentration of PT-PBS than its IC_{50} values (i.e., we fixed it at 10% for the TMZ-sensitive cell lines; 15% for U87-MG and 20% for the T98G cell line) and we varied the concentrations of TMZ in a range lower than its obtained IC_{50} values (i.e., 40, 20 and 10 μ M for the TMZ-sensitive cell lines, and 72, 36 and 18 μ M for the TMZ-resistant cell lines). As shown in Figure 7.4 a-c, TMZ (40 μ M) and 10% PT-PBS

treatment alone had a cytotoxic effect in U251, LN18, and LN229 (i.e., the TMZ-sensitive cell lines) after 24 hours (approx. 35 to 40% cell death, close to the IC₅₀ values). Interestingly, the combination of PT-PBS and TMZ showed synergistic toxicity, inducing up to 85-90% ($p \leq 0.001$) cell death in all TMZ-sensitive cell lines. Similarly, in case of U87-MG and T98G, TMZ 72 μ M and 15% or 20% PT-PBS treatments alone were cytotoxic after 24 hours (approx. 25 to 35% cell death). The combination treatment of PT-PBS and TMZ again showed synergistic toxicity, resulting in up to 78% ($p \leq 0.001$) cell death in U87-MG and 62% ($p \leq 0.01$) cell death in T98G (Figure 7.4 d and e).. Altogether, these results suggest the synergistic cytotoxic action of PT-PBS and TMZ in both TMZ-sensitive and TMZ-resistant cell lines.

PT-PBS and TMZ treatment do not cause significant damage in 3D spheroids

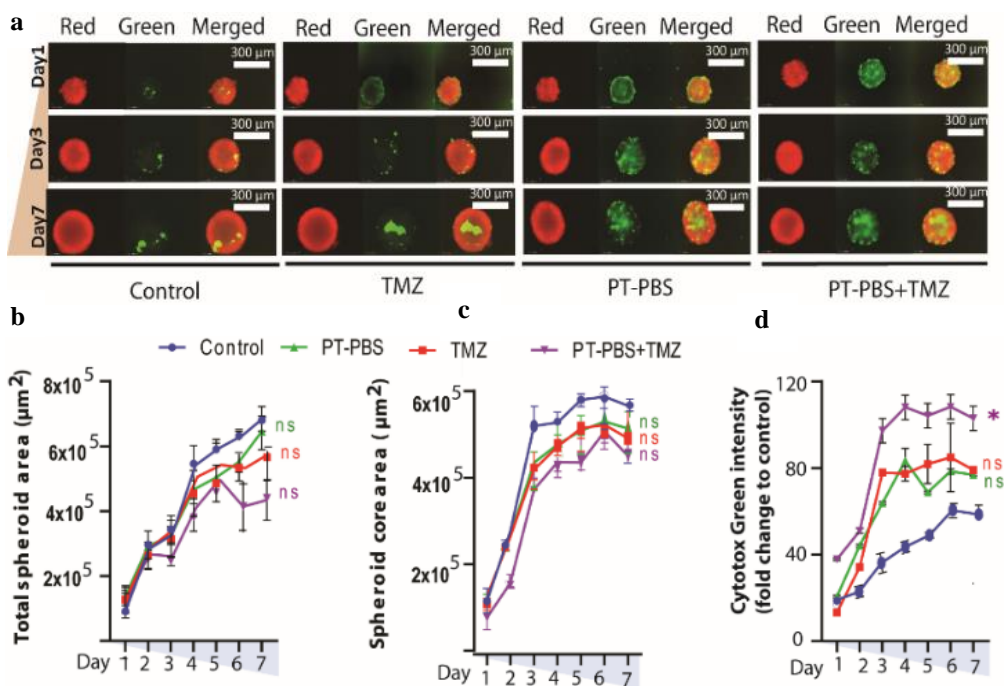


Figure 7.5 (a) Images of U251 3D spheroids following indirect plasma treatment: red image of spheroid represents live cells, green represents dead cells within the spheroid, and merged represents the combined image of red and green; (b) total spheroid area of viable cells + dead cells in the spheroid, (c) area of the spheroid core (viable cells), and (d) Cytotoxic green intensity in the spheroids (dead cell confluency), where * = $p \leq 0.05$, ** = $p \leq 0.01$, *** = $p \leq 0.001$.

We tested the cytotoxicity of PT-PBS (10%) and TMZ (40 μ M) alone and in combination on U251 (TMZ-sensitive) spheroids, using the doses obtained from the 2D experiments. The experimental design of the indirect plasma treatment of the spheroids was illustrated in Figure 7.1. The total spheroid area was measured to assess changes in spheroid size due to cell death and destruction of the spheroid architecture (Figure 7.5a-d). The individual treatment of U251 spheroids with 10% PT-PBS or 40 μ M TMZ did not induce significant cytotoxic effects ($p = ns$), and did not inhibit spheroid growth (Figure 7.5 a-c). We only observed a slight increase in cell death for the combined treatment ($p = ns$, Figure 7.5d). Large tumor spheroids with diameter greater than 500 μ m normally consist of three layers, i.e., proliferating and quiescent regions and a necrotic core. Proliferating cells provide the driving force for tumor growth. It is a target of interest for tumor studies, since a lot of activities occur in this region. Quiescent cells have no growth or active motion but still consume nutrients. The necrotic core is comprised of dead cells which are regarded only as viscoelastic material without living activities. When the nutrient environment changes, proliferating cells may become quiescent cells and eventually die due to the limited distribution of oxygen and nutrients. In addition, quiescent cells may convert to the proliferating type if sufficient nutrients return, which leads to heterogeneous situations within the spheroid core. This heterogeneous nature of viable cells within a spheroid is also observed in our study (Figure 7.5a and 7.6d). A bright red signal (representative of viable cells) is observed at the edge of the spheroid, and it decreases or disappears towards the necrotic center. After mono or combinational treatments, we observed cell debris around the spheroids, which are mostly formed by dead cells (positive for the cell death stain Cytotox Green). We have defined the area under the sharp and tight edges of the spheroid as 'spheroid core area', whereas the 'total spheroid area' is the sum of both 'spheroid core area' and the area of debris. Hence, these treatments alone or in combination were not enough to inhibit spheroid growth or decrease the spheroid core area. The reason is that the treated spheroids receive only long-lived reactive species, produced upon interaction between plasma and the treated liquid. Indeed, it is reported that 3D spheroids are more resistant

to treatment than cells in monolayers. Direct treatment, however, delivers both short-lived and long-lived species, as well as ultraviolet radiation, charged particles, and electromagnetic fields, with higher chances to induce the desired response in spheroids. Thus, for further treatments, we directly applied the COST plasma jet on U251 (TMZ-sensitive) and U87-MG and T98G (TMZ-resistant) spheroid models. We selected these three cell lines because of their ability to form tight spheroids.

Direct plasma treatment is cytotoxic for both TMZ-sensitive and TMZ-resistant GBM spheroids

Here we evaluate the effect of CAP in combination with TMZ on U251 (TMZ-sensitive) and U87-MG and T98G (TMZ-resistant) spheroids, which offer a closer architecture to the natural tumor microenvironment than 2D cell cultures. The experimental setup was schematically illustrated in Figure 7.2. Treating the spheroids with TMZ (40 μ M for U251 and 72 μ M for U87-MG and T98G) alone has virtually no effects, with only a slight reduction of the total spheroid area and core area and a small fraction of dead cells in all three cell lines (Figure 7.6 a-d), evidencing a low response to TMZ treatment. On the other hand, 3 min CAP treatment shows a clear reduction in total spheroid area and core area, and a larger fraction of dead cells, in U251 and U87-MG, but not in T98G, suggesting resistance of the T98G spheroids to CAP treatment.

However, when 3 min CAP and TMZ (40 μ M for U251, and 72 μ M for U87-MG and T98G) treatments were combined, significant cytotoxicity (expressed as the reduction of total spheroid and core area) was achieved in both TMZ-sensitive (U251, reduction of total spheroid ($p \leq 0.01$), core area ($p \leq 0.001$)) and TMZ-resistant spheroid models (U87-MG, reduction of total spheroid ($p \leq 0.01$), core area ($p \leq 0.001$)) and T98G, reduction of total spheroid ($p \leq 0.001$), core area ($p \leq 0.01$)) (Figure 7.6 a-b). Similarly, both the TMZ-sensitive and TMZ-resistant spheroids presented elevated intensity of Cytotox green (U251 ($p \leq 0.001$), U87-MG ($p \leq 0.001$) and T98G ($p \leq 0.01$)) (Figure 7.6c) in the combination treatment, which is also quite clear from the fluorescence microscopy analysis (Figure 7.6d). These findings indicate that the combined treatment induces cell death within the spheroids.

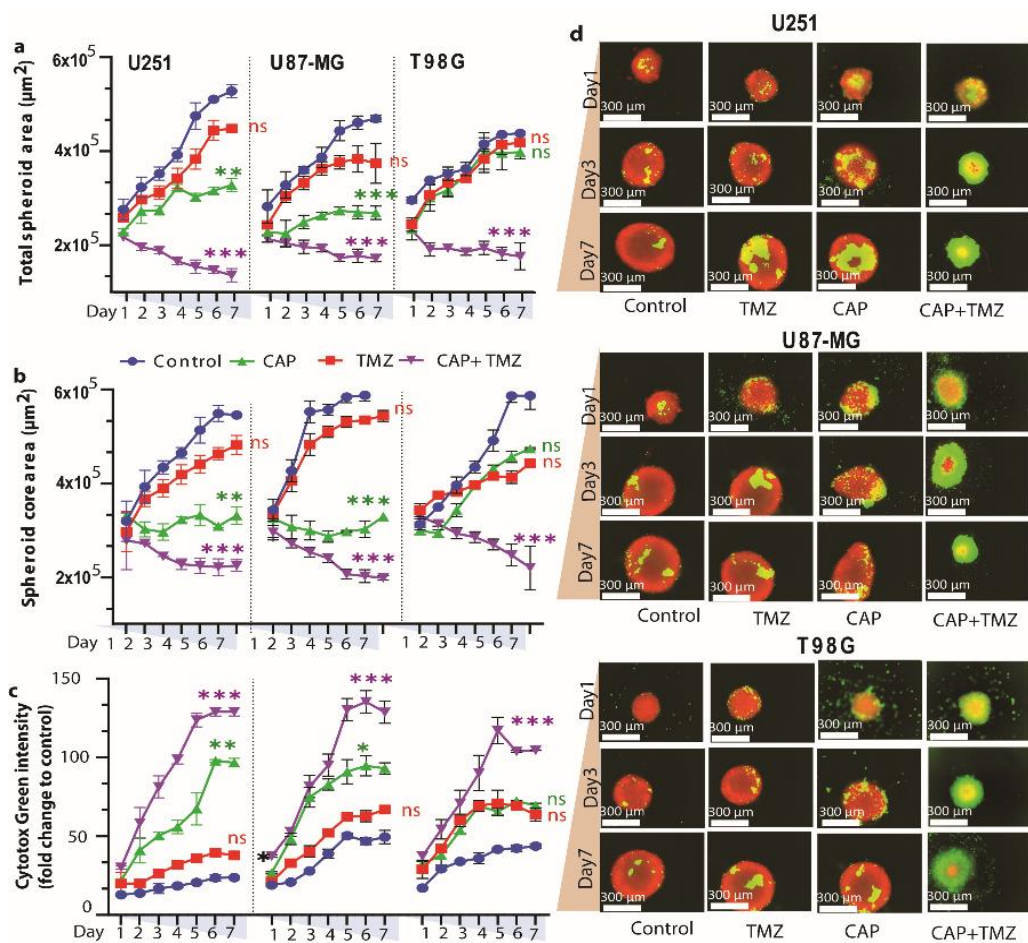
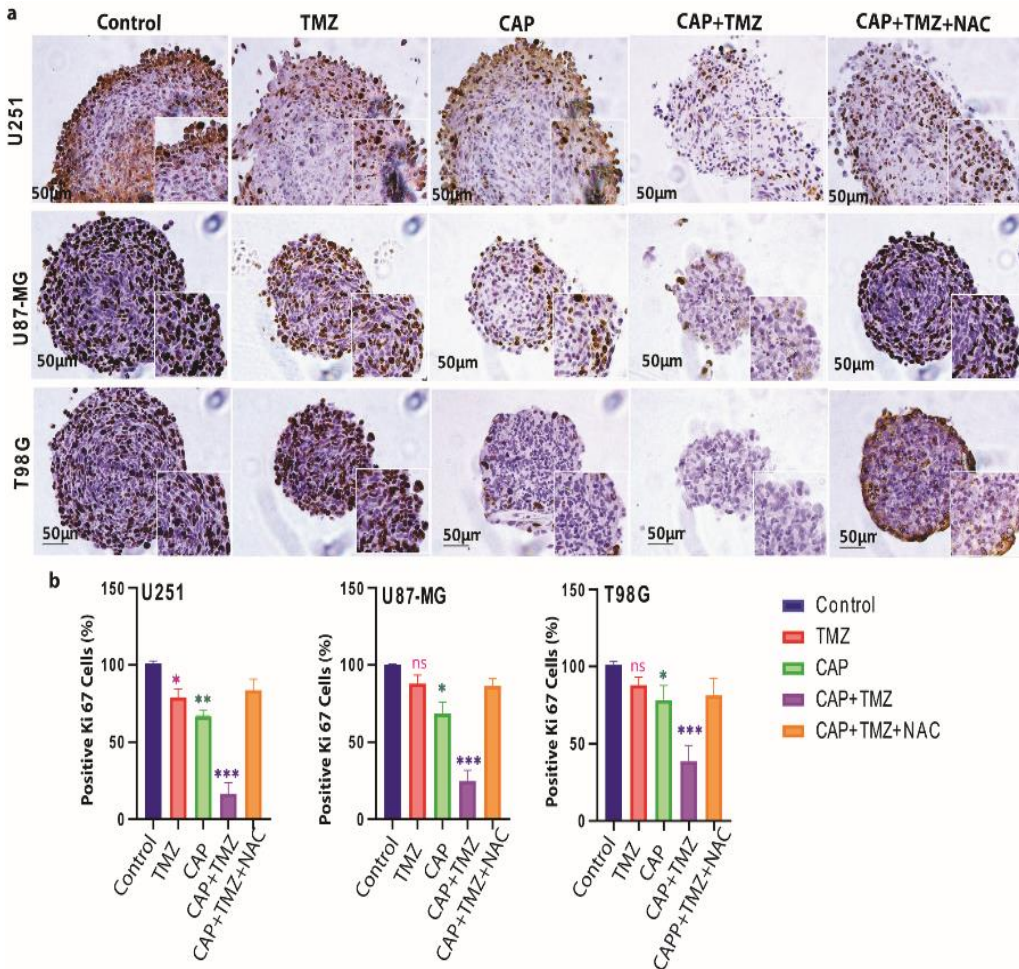


Figure 7.6 (a) Images of U251 3D spheroids following indirect plasma treatment: red image of spheroid represents live cells, green represents dead cells within the spheroid, and merged represents the combined image of red and green; (b) total spheroid area of viable cells + dead cells in the spheroid; (c) area of the spheroid core (viable cells), and (d) Cytotox green intensity in the spheroids (dead cell confluency), where $*$ = $p \leq 0.05$, $**$ = $p \leq 0.01$, $***$ = $p \leq 0.001$.

Ki-67 expression is reduced in TMZ-sensitive and TMZ-resistant GBM spheroids



*Figure 7.7 Effect of CAP (COST jet), TMZ and their combination treatment on the expression of the proliferative marker Ki-67 in GBM spheroids; (a) representative images of Ki-67 staining. The enlarged image demonstrates variable ki67 staining. (b) Percentage of Ki-67+ cells were scored using ImageJ software, where * = $p \leq 0.05$, ** = $p \leq 0.01$, *** = $p \leq 0.001$; data are representative of two independent experiments, 5 spheroids per condition.*

To understand the specific inhibitory therapeutic effects of CAP and TMZ treatment, we assessed the expression of the proliferation marker Ki-67 in the spheroids by immunohistochemistry. We observed a reduced percentage of Ki-67⁺ cells after the individual 3 min CAP ($p \leq 0.01$ for U251, and $p \leq 0.05$ for U87-MG and T98G) and TMZ ($p \leq 0.05$ for U251, and not significant for U87-MG and T98G) treatments compared

with the untreated controls, but the effect was much more pronounced in all three cell line spheroids after the combined treatment ($p \leq 0.001$) (Figure 4).

Induction of intracellular ROS causes GSH/GPX4 inhibition in TMZ-sensitive and TMZ-resistant GBM spheroids

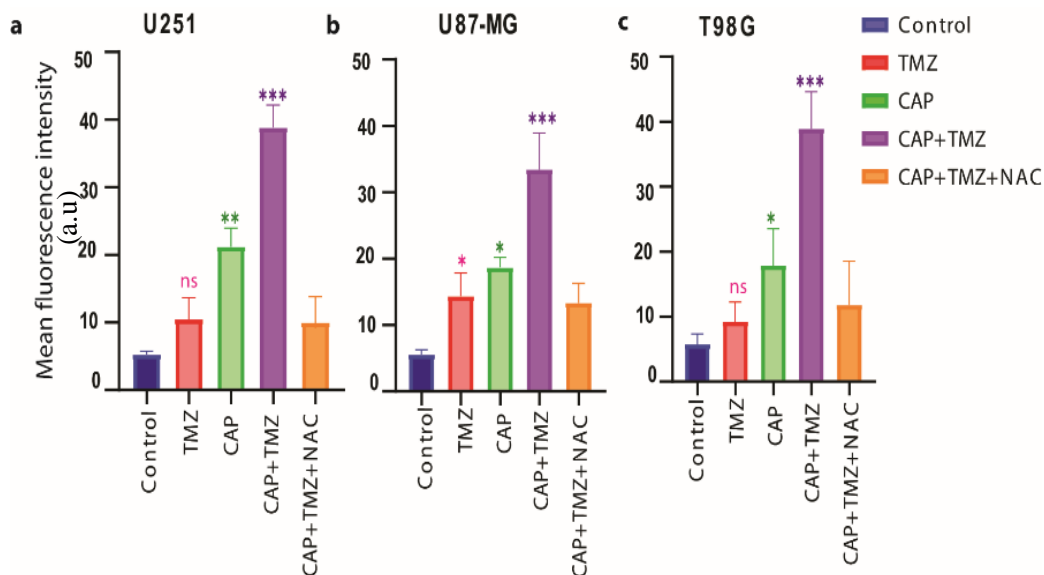


*Figure 7.8 Intracellular reactive oxygen species (ROS) content upon treatment of CAP, TMZ, CAP + TMZ and CAP + TMZ + NAC (a) U251 (TMZ-sensitive), (b) U87-MG and (c) T98G (TMZ-resistant) spheroids, where * = $p \leq 0.05$, ** = $p \leq 0.01$, *** = $p \leq 0.001$; data are representative of two independent experiments, 5 spheroids per condition.*

To evaluate the change in the intracellular antioxidant machinery and the release of intracellular ROS upon treatment, we quantified the intracellular ROS levels, the depletion of glutathione levels (GSH) and the suppression of GPX4 expression upon treatment. We measured the intracellular ROS levels using CellROX[®] Green reagent. This cell-permeable compound dye binds to nuclear and mitochondrial DNA and becomes strongly fluorescent upon oxidation. In case of intracellular ROS release, the combination treatment 3 min CAP + TMZ shows higher fluorescence intensity when compared to the CAP and TMZ treatment alone for both TMZ-sensitive (U251, $p \leq 0.001$) and TMZ-resistant (U87-MG, $p \leq 0.001$; and T98G, $p \leq 0.001$) spheroids (Figure 7.8). This indicate that the CAP synergistically enhances the therapeutic effect of TMZ

against GBM spheroids. The ROS scavenger NAC reversed the effects of the combination therapy in both TMZ-sensitive and TMZ-resistant spheroids.

We observed that the combination therapy significantly (for U251 cells $p \leq 0.01$, for U87-MG cells $p \leq 0.01$ and for T98G cells $p \leq 0.05$) decreases the GSH levels (Figure 7.9) and the protein expression of GPX4 (Figure 7.10a) in both TMZ-sensitive (U251, $p \leq 0.01$) and TMZ-resistant (U87-MG, $p \leq 0.001$ and T98G, $p \leq 0.01$) spheroids.

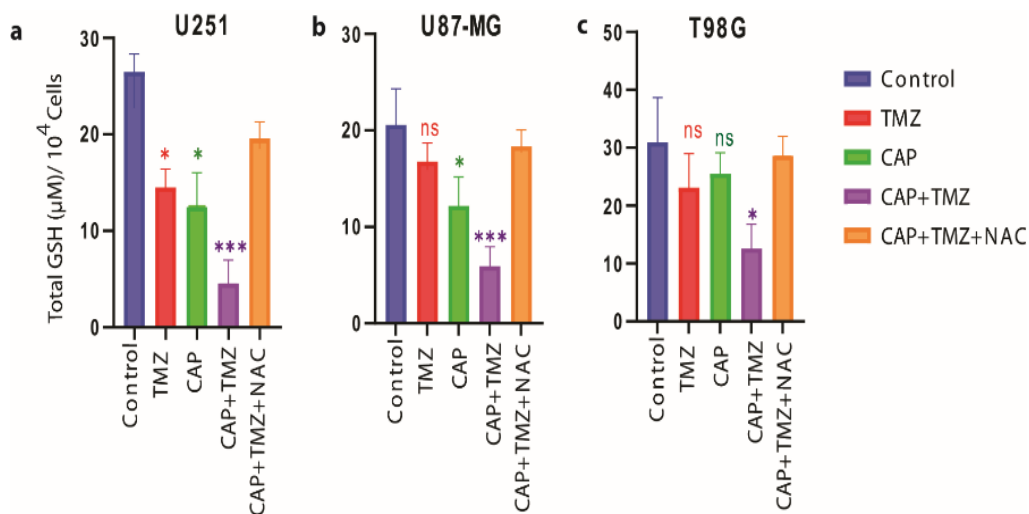


Figure 7.9 Intracellular GSH content upon treatment with CAP, TMZ, CAP + TMZ and CAP + TMZ + NAC (a) U251 (TMZ-sensitive), (b) U87-MG and (c) T98G (TMZ-resistant) spheroids, where * = $p \leq 0.05$, ** = $p \leq 0.01$, *** = $p \leq 0.001$; data are representative of two independent experiments, 5 spheroids per condition.

The effects of combined treatment seem to be restored by the addition of NAC inhibitor, indicating that CAP synergistically enhances the therapeutic effect of TMZ in three different GBM spheroids.

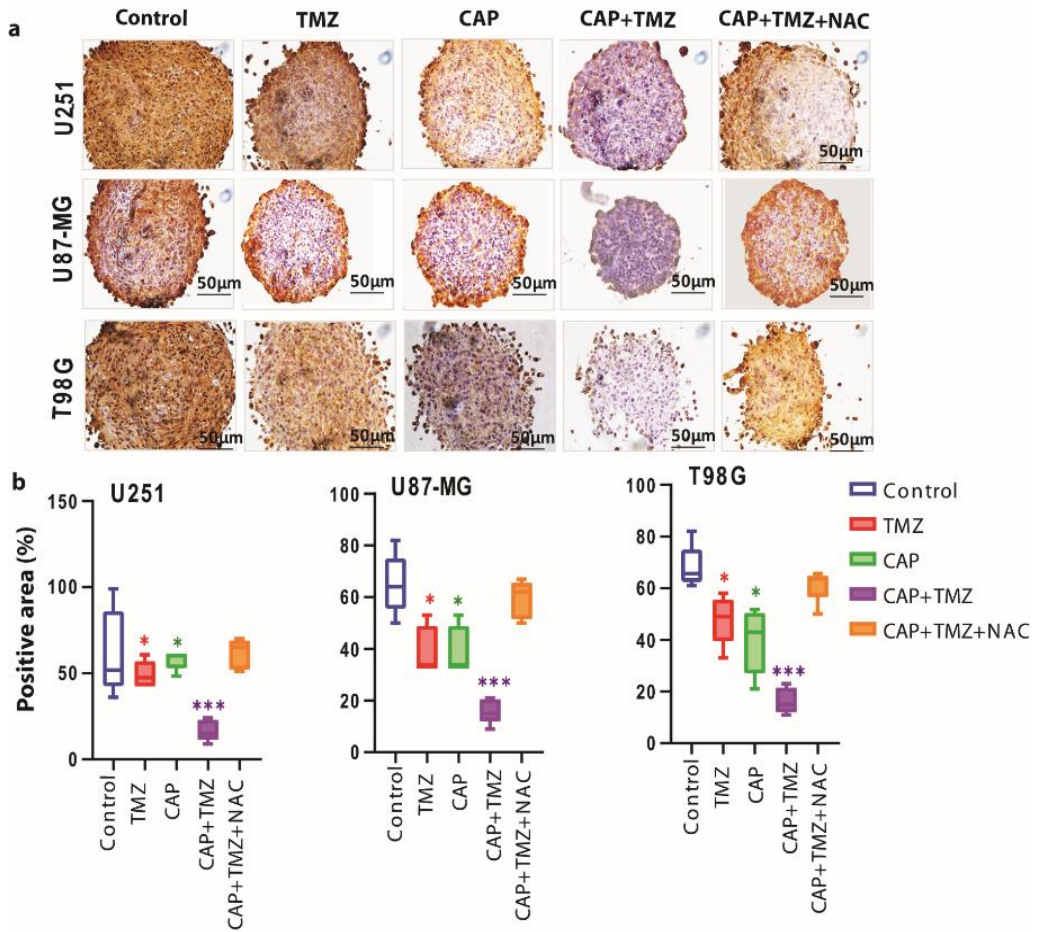


Figure 7.10 (a) Histochemical staining of GPX4 protein expression (brown color) in the U251, U87-MG and T98G spheroids, following TMZ, CAP, CAP + TMZ and CAP + TMZ + NAC treatment. (b) GPX4 protein expression quantified using ImageJ software, where $* = p \leq 0.05$, $** = p \leq 0.01$, $*** = p \leq 0.001$; data are representative of two independent experiments, 5 spheroids per condition.

Combination of CAP and TMZ causes DNA oxidation in TMZ-sensitive and TMZ-resistant GBM spheroids

To gain further insight into the impairment of the antioxidant function by CAP-induced DNA damage in TMZ-sensitive and TMZ-resistant GBM spheroids, we measured the levels of 8-hydroxy-2'-deoxyguanosine (8-OHdG) and 8-Oxo-2'-deoxyguanosine (8-oxo-dG), which are the most representative biomarkers of oxidative damage to DNA. The resistance of GBM to TMZ therapy was found to be closely related to the GSH/GPX4 (antioxidant machinery) system of the cell²³⁵. In our recent paper³¹ (31) we showed that CAP triggered cell death in a dose- and time-dependent manner, which was due to increased ROS levels and an inhibition of the GSH/GPX4 antioxidant machinery system of the cell²³⁵. ROS accumulation is regarded as one hallmark of oxidative stress-mediated cell death. Many data show that various ROS scavengers can entirely avoid cell death and cellular ROS accumulation¹²⁰. Similarly, administration of TMZ downregulates the antioxidant-related signaling molecules, such as GSH/GPX4, which play an important role in cell death²³⁶⁻²³⁸. Thus, it could be possible that the combination treatment induces excessive intracellular RONS, which may subsequently have a critical role in oxidative stress-induced cell death. Therefore, together with an increasing endogenous ROS environment and an inhibiting antioxidant system, this results in the accumulation of hydroxyl ($\cdot\text{OH}$) radicals and promotes DNA oxidation.

The combination treatment of 3 min CAP and TMZ resulted in a higher expression of 8-OHdG when compared to the CAP and TMZ treatments alone (U251 ($p \leq 0.001$), U87-MG ($p \leq 0.001$) and T98G ($p \leq 0.001$), Figure 7.11 a – 7.11f), as well as higher levels of 8-oxo-dG formation (U251 ($p \leq 0.001$), U87-MG ($p \leq 0.001$) and T98G ($p \leq 0.001$); Figure 7.11g-7.11i), in both TMZ-sensitive and TMZ-resistant spheroids. Again, this confirms the role of CAP in amplifying the DNA damage upon TMZ treatment and leads to a strong synergistic effect (CI = 0.2 to 0.4).

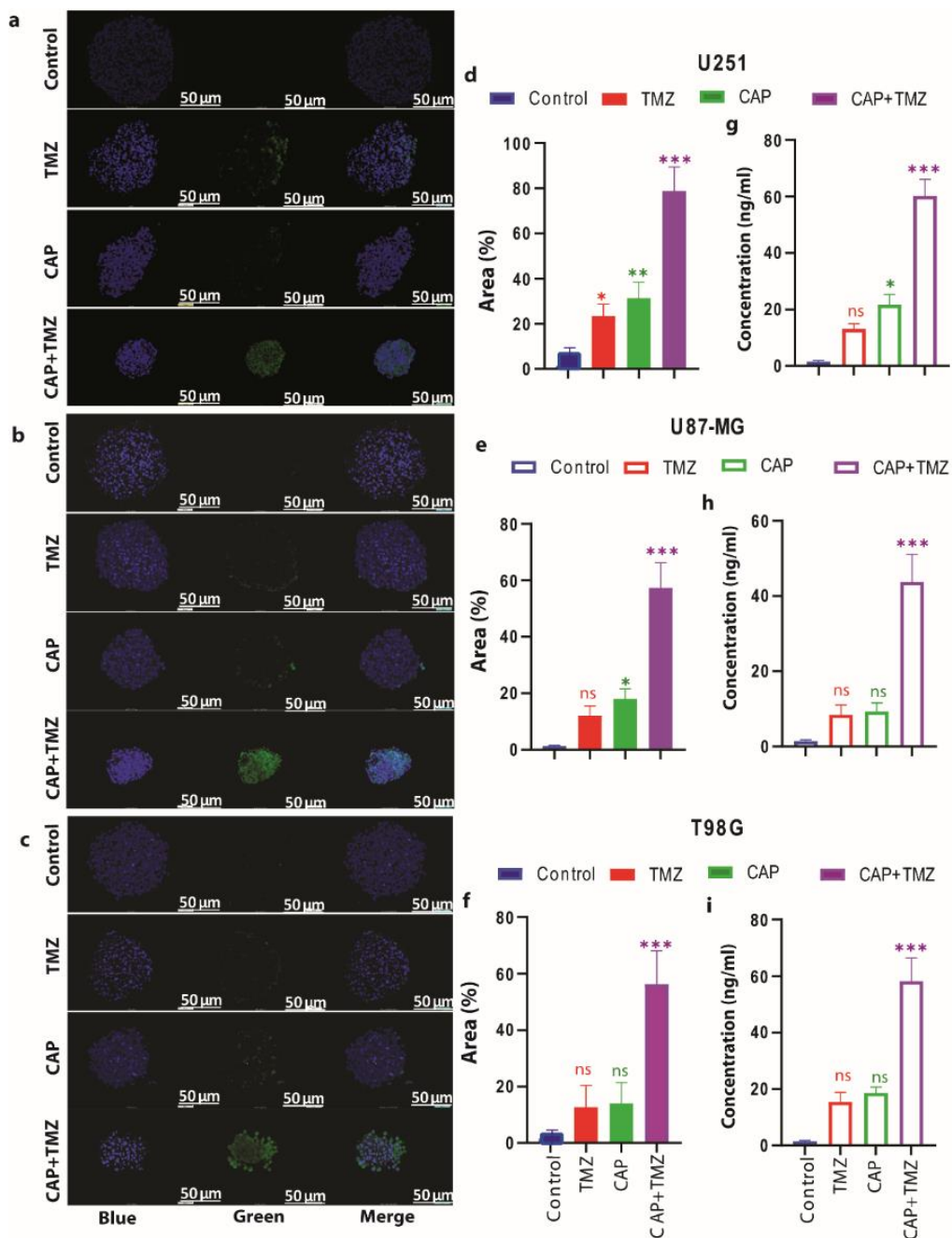


Figure 7.11 (a–c) Expression of 8-oxo-dG (in green) in U251, U87-MG and T98G spheroids upon treatment of TMZ alone and their combination, blue (DAPI) represents the nuclear counterstain. (d–f) The staining was scored using ImageJ software (g–i) Quantification of (8-OHdG) in U251, U87-MG and T98G spheroids upon TMZ alone and their combination (CAP + TMZ), where * = $p \leq 0.05$, ** = $p \leq 0.01$, *** = $p \leq 0.001$; data are representative of two independent experiments, 5 spheroids per condition.

7.5. Discussion

The GBM resistance to TMZ is the most important cause of chemotherapy failure^{236,237}. Thus, to determine whether the combined treatment of CAP and TMZ reduced the cell viability of GBM cells, we applied indirect plasma treatment (PT-PBS) in combination with TMZ to five different GBM cell lines. Two types of plasma treatment are applied in cancer research: direct and indirect treatment. In the case of direct treatment, cells or tissue are directly treated with the plasma source. In indirect treatment, PTLs have shown promising therapeutic efficacy against drug resistant cancers, such as GBM, lung cancer, leukemia, melanoma, and pancreatic adenocarcinomas, and receive growing scientific interest^{9,188,238,239}. Most of these studies are carried out on 2D monolayer cell cultures, while only a few studies have considered the biological microenvironment of the tumors, which can be mimicked using the 3D tumor spheroid model^{96,222,223,240-242}. The tumor microenvironment plays a key role in the response to treatment, regulating tumor progression and metastatic processes²⁴³. Thus, it is possible that therapies developed using only 2D cell cultures do not meet the requirements to achieve the desired response as in *in vivo* models. A 3D tumor spheroid model can bridge this gap because, in this model, cells are grown as aggregates of single or multiple cell types. This allows 3D cell–cell contact, and proliferation in a more physiological geometry that stimulates the production of extracellular matrix proteins and enhances intercellular communication²⁴⁴. When evaluating the biological effects for the purpose of quantifying patient treatment efficacy, 3D spheroid assays may thus better reflect the response of cells within a tumor than 2D cell cultures. Thus far, however, no combinational studies of plasma with TMZ have been performed on GBM spheroid models.

We believe CAP enhances the effect of TMZ because it acts via the generation and local deposition of various ROS on the target, leading to changes in the redox environment and redox-mediated signaling towards tumor cell death. We have previously shown that CAP decreases the phospholipid free energy barrier of cell membranes, affecting the membrane integrity and the overall tumor growth⁹. We have also shown

that both short-lived and long-lived species delivered by CAP effectively inhibit tumor growth and reduce cell migration in GBM spheroids ²²².

Altogether, these data demonstrate that direct plasma treatment has more cytotoxic effects in 3D GBM spheroids than indirect plasma treatment (PT-PBS). Indeed, during direct plasma treatment, the combination of short-lived and long-lived species, such as $\cdot\text{OH}$, O , $\text{O}_2^{\cdot-}$, O_2 , O_3 , $\text{NO}\cdot$, $\text{NO}_2\cdot$, NO_2^- , NO_3^- and H_2O_2 , work simultaneously on the targeted cells and tissue. Moreover, the short-lived reactive species, such as $\cdot\text{OH}$, O , $\text{O}_2^{\cdot-}$, O_2 , and $\text{NO}\cdot$, lead to subsequent reaction on the tumor surface, which causes self-perpetuation of toxicity after being in direct contact with CAP ²⁴⁵, while the cytotoxicity effects produced by indirect treatment can only be due to long-lived species, such as H_2O_2 and $\text{NO}_2^-/\text{NO}_3^-$.

Interestingly, the addition of NAC restores the effect of the combined treatment to the effect of TMZ only in U251 and U87-MG, and to the level of CAP only in T98G. This might indicate some differences in mechanism in the response between the different cell lines, but to elucidate these differences, more dedicated studies would be needed. In the literature, it was shown that T98G was more resistant to TMZ, caused by lower ROS levels and a higher total antioxidant capacity and GSH concentration ²³⁴. Therefore, increasing exogenous ROS levels together with inhibiting the antioxidant defense system could overcome this therapy resistance. In the case of combined treatment, we found significant inhibition of Ki-67⁺ cells. However, in the presence of NAC, the treatment effects were reduced to the level of CAP treatment only. NAC was not able to fully circumvent the combined effect of the treatment, as its addition reduced the ROS to levels similar to those in CAP only. It is thus possible that other signaling molecules were involved in the response evoked. More studies could help to further elucidate this response.

Cancer cells are metabolically hyperactive, they produce high levels of ROS, and are under intrinsic oxidative stress, which makes them more vulnerable to oxidative stress by exogenous RONS, as produced by CAP ²⁴⁶⁻²⁴⁸. The combination of CAP and TMZ treatment may increase the intracellular ROS levels, which leads to the depletion of the intracellular GSH level, and GPX4 expression, and consequently to cell death. The enhanced intracellular ROS levels in response to CAP + TMZ treatment can further result

in the depletion of GSH levels and the suppression of GPX4 expression, which causes oxidative stress-mediated cell death^{238,249}. GPX4 inactivation is one of the key features of cell death, which occurs either through a drop in GSH levels and/or by direct oxidative modification of the GPX4 enzyme.

Furthermore, to see the result of impairment of the antioxidant system on DNA damage in TMZ-sensitive and TMZ-resistant GBM spheroids, we measured the levels of 8-hydroxy-2'-deoxyguanosine (8-OHdG) and 8-Oxo-2'-deoxyguanosine (8-oxo-dG), which are the most representative biomarkers of oxidative damage to DNA. Again, this confirms the role of CAP in amplifying the DNA damage to TMZ treatment and led to a strong synergistic effect.

7.6. Conclusion

TMZ is an alkylating agent, used in the treatment of GBM, which induces oxidative stress-mediated cell death. A recurring issue with current chemotherapeutics used for GBM treatment is the adverse side effects induced due to the high toxicity of these drugs, and the developed resistance over time. To address this problem, we investigated whether the combined treatment of CAP and TMZ has potential to overcome TMZ resistance in GBM. To achieve our aim, we applied indirect (PT-PBS) as well as direct plasma treatment in combination with TMZ on both TMZ-sensitive and TMZ-resistant GBM cells. Interestingly, we found that the combination of PT-PBS with TMZ enhances the efficacy of the latter towards both TMZ-sensitive and TMZ-resistant cells *in vitro*. However, PT-PBS alone or in combination was not effective on both U251 (TMZ-sensitive) and U87-MG and T98G (TMZ-resistant) 3D spheroid models, because 3D spheroids are more resistant to treatment than cells in monolayers. To evaluate the response of plasma on tumor spheroids, we applied direct CAP treatment on both TMZ-sensitive and TMZ-resistant spheroids. The reason is that direct plasma treatment delivers a complex mixture of long-lived and short-lived RONS upon direct contact with the biological sample, while during indirect treatment, the biological sample receives only the long-lived reactive species. Our results demonstrate that combined direct CAP + TMZ treatment significantly improves the response of GBM to TMZ treatment in spheroids, as

demonstrated by the reduction in spheroid growth. This improvement is attributed to the inhibition of the GSH/GPX4 antioxidant machinery, which leads to DNA oxidation. Indeed, the combination treatment induces the expression of 8-OHdG and the formation of 8-oxo-dG products, likely due to the accumulation of OH radicals induced by CAP. Such attack on DNA can lead to cell death in both TMZ-sensitive and TMZ-resistant spheroid models. The findings presented in this study provide a novel therapeutic strategy for GBM to enhance the efficacy of TMZ through a combination of increasing exogenous ROS and inhibiting the protective antioxidant system.

Chapter 8: Summary

Reactive oxygen and nitrogen species (RONS) generated by cold atmospheric plasma (CAP) can activate discrete signaling transduction pathways or disrupt redox cellular homeostasis, depending on their concentration. This makes that CAP possesses therapeutic potential towards wound healing, cancer, and other diseases. In order to effectively use CAP in the clinic, a clear understanding of the interaction of RONS with biomolecules (lipids, proteins and nucleic acids) from the atomic to the macro scale, and their biological significance, is needed.

Main findings of the thesis

In this work, I have therefore studied the dual role of CAP-derived RONS (discussed in [Chapter 1](#)), i.e., (i) in the signaling pathways involved in wound healing, and (ii) in their reaction with biomolecules to cause oxidation-mediated damage. I performed computer simulations ([Chapter 2](#)) to provide fundamental insight about the occurring processes that are difficult or even impossible to obtain experimentally. Furthermore, next to computational studies, I used both 2D and 3D tissue cultures. I used a 3D tissue model ([Chapter 3](#)) because in this model cells are grown as aggregates of single or multiple cell types that allows cell–cell contact. Even more, the 3D model allows proliferation in a more physiologically relevant geometry that stimulates the production of extracellular matrix proteins.

(i) The role of CAP in signaling pathways. In the first part of my thesis, we determined that CAP accelerates the migration of human gingival fibroblasts (HGFs) ([Chapter 4](#)). HGFs treated with CAP for 3 min migrate to each other across the gap faster than those in the control group and the 5-min treatment group at days 1 and 3. We found that low-dose CAP treatment does not inhibit HGF proliferation. The migratory effect could be supported by new myogenesis formation and extracellular matrix (ECM) breakdown. We revealed that three steps are involved in the migration of the HGFs. The first step is cell cycle arrest caused by the low-dose CAP-derived RONS that is not lethal to cells. The second step is ECM disruption for the establishment of the migrating bed for easier transportation of cells. Finally, HGF migration occurs as a result of an outward

migrating signal cascade. The HGFs detach and move to the middle of the wound, until the wound closure is completed. Overall, these synergistic actions of CAP help establishing favourable wound beds and result in enhanced wound healing.

(ii) CAP causes oxidation-mediated cell death. CAP-generated species initially interact with the outer surface of cells, i.e., the phospholipid bilayer membrane, and induce its oxidation. CAP-induced oxidation of the phospholipids demonstrated that cell membranes with higher fractions of cholesterol (i.e., typical for normal cells) were protected from pore formation. In contrast, when lower concentrations of cholesterol were present (i.e., typical for most cancer cells), the cell membrane was more vulnerable to oxidative stress, and it favoured pore formation. The pores generated in the cell membrane facilitate the transport of plasma-generated RONS into the intracellular compartment, where they can exert further oxidative damage to cells. Furthermore, this pore formation also allows a better transdermal drug delivery. In [Chapter 5](#), I demonstrated that RONS present in plasma-treated phosphate buffered saline (PT-PBS) (e.g., H_2O_2 , NO_3^- and NO_2^- ions) oxidize the cell membrane (lipid peroxidation) and increase the permeation of the anti-cancer drug melittin (MEL) across the lipid bilayer. Therefore, the therapeutic dose of MEL required to exert a cytotoxic effect in cancer cells can be reduced after PT-PBS treatment. The synergy between MEL and CAP is attributed to the change in membrane integrity upon peroxidation of the membrane lipids by the RONS present in PT-PBS. As a result, the MEL translocation rate through the cell membrane increases significantly, as demonstrated by ‘umbrella sampling’ molecular dynamics (MD) simulations. Hence, more MEL molecules are able to penetrate into the cell at lower treatment doses.

Further, excessive lipid-peroxidation plays a key role in regulating non-apoptotic cell death mechanisms, such as ferroptosis caused by impairment of redox balance. In [Chapter 6](#), I focused on CAP-generated reactive species that directly interact with the cell membrane and cause increased level of Fe^{2+} and lipid peroxidation, which eventually induces ferroptosis through depletion of GSH/GPX4 and its regulating redox factor HMOX1. Typically, HMOX1 induces a cytoprotective antioxidant response by degrading heme to generate carbon monoxide, biliverdin, and Ferrous ions (Fe^{2+}) under

mild oxidative stress conditions. However, when oxidative stress and lipid peroxidation levels increase above the homeostatic stress tolerance, antioxidant cytoprotection may lead to ferroptotic cell death. For example, excessive amounts of HMOX1 trigger sensitization of ferroptosis due to an imbalanced increase of Fe^{2+} levels, insufficient buffering capacity by ferritin and uncontrolled production of hydroxyl radicals via the Fenton reaction. In contrast, the effects of CAP were lost in presence of the ferroptosis inhibitor Fer-1, indicating indeed that the excessive lipid peroxidation induced by CAP may be in part due to the inactivation of the GPX4/GSH lipid repair enzyme system, responsible for induction of ferroptotic cell death. To gain further insight into the impairment of GPX4 functions by CAP-induced RONS, I performed MD simulations. This method allows to predict conformational changes in the catalytic active pocket of GPX4 upon oxidation. Movement and rotation of the side chain of cysteic acid and 6-hydroxytryptophan in the oxidized structures results in a rearrangement of the surrounding amino acids, increasing the $\text{C}\alpha$ distances among the catalytic machinery of GPX4. Monitoring the $\text{C}\alpha$ distances shows that oxidation of the catalytic residues plays a critical role in the stability of GPX4. Specifically, the $\text{C}\alpha$ distances among the catalytic triad are relatively long for making an H-bond between them. Additionally, the root-mean-square-deviation (RMSD) of the catalytic machinery of GPX4 in the native structure was more stable than in the oxidized structure. This reduced stability in the oxidized structure may contribute to a decreased expression of GPX4 observed in the immunohistochemistry analysis of the GPX4 expression.

The reduction and activation of antioxidant-related signaling molecules, such as GSH/GPX4 or HMOX1, also plays an important role in drug resistance, as it can turn the oxidation-mediated response on and off, dependent on the intracellular redox status. High intracellular GSH/GPX4 levels in cancer cells lead to epithelial–mesenchymal transition, which results in tumor progression, metastasis and chemoresistance. In [Chapter 7](#), I showed that CAP increases the sensitivity of Temozolomide (TMZ) in a 3D spheroid tumor model (i.e., higher cytotoxicity and spheroid shrinkage was obtained when TMZ and CAP were administered together) in a dose- and time-dependent manner, due to increased ROS levels and an inhibition of the GSH/GPX4 antioxidant machinery. Thus,

the combination treatment can induce excessive intracellular RONS levels, which may subsequently have a critical role in oxidative stress-induced cell death. Therefore, together with increasing the endogenous ROS environment, inhibiting the antioxidant system results in the accumulation of hydroxyl (OH) radicals and promotes DNA oxidation, as observed by the high levels of 8-hydroxy-2'-deoxyguanosine (8-OHdG) and expression of 8-Oxo-2'-deoxyguanosine (8-oxo-dG), which are the most representative biomarkers of oxidative damage to DNA.

Outlook for future work

In this PhD thesis, I aimed to elucidate several mechanisms at the molecular level for plasma medicine applications, i.e., wound healing and enhancement of transdermal drug delivery in cancer treatment, that is mainly mediated via reactive oxygen and nitrogen species (RONS). However, electric fields and other components of CAP should not be neglected, because they are also shown to contribute to pore formation in the cell membrane. This allows RONS to enter the cells and cause strong effects on other biomolecules.

CAP has shown remarkable achievements in the field of plasma medicine, such as inactivation of bacteria, treatment of chronic wounds, and selective killing of cancer cells. However, many more investigations on the interactions of CAP with prokaryotic and eukaryotic cells are still needed in order to generate a complete picture of plasma medicine. In my opinion, future research should include (i) the elucidation of CAP-triggered signaling pathways that may lead to apoptosis or necrosis in cancer cells; (ii) studying the combined effect of reactive species with other components of CAP, such as electric fields, UV, etc.; (iii) the investigation of CAP-induced long-term effects on macromolecules such as DNA and proteins; (iv) figuring out the epigenetic effects of CAP on normal cells; and (v) assessment of CAP exposure on immune cells. In the last two decades, the plasma medicine field has made significant progress in understanding of the underlying mechanisms. At this stage, it seems ready for clinical trials, so that it can enter into the health care arena. The various *in vitro* and *in vivo* studies performed

within our plasma medicine community in the last decades are very important, if we want plasma medicine to become a real adjuvant treatment therapy.

Samenvatting (Summary in dutch)

Reactieve zuurstof- en stikstofdeeltjes (Eng: reactive oxygen and nitrogen species, RONS) geproduceerd door koud atmosferisch plasma (Eng: cold atmospheric plasma; CAP) kunnen discrete signaaltransductieroutes activeren of redox-cellulaire homeostase verstoren, afhankelijk van hun concentratie. CAP heeft dus een therapeutisch potentieel voor wondgenezing, kanker, en mogelijk andere ziekten. Om CAP effectief in ziekenhuizen te kunnen gebruiken, is een duidelijk begrip van de interactie van RONS met biomoleculen (lipiden, eiwitten en nucleïnezuren) nodig, van atomaire schaal tot macroschaal, alsook van de biologische effecten hiervan.

Belangrijkste bevindingen van het proefschrift

In dit werk heb ik daarom de dubbele rol van CAP-geproduceerde RONS bestudeerd (besproken in [Hoofdstuk 1](#)) die (i) helpen bij de signaalroutes betrokken bij wondgenezing, en (ii) reageren met biomoleculen en oxidatieve schade veroorzaken. Ik heb computersimulaties uitgevoerd ([Hoofdstuk 2](#)) om fundamenteel inzicht te krijgen in de onderliggende processen die experimenteel moeilijk of zelfs onmogelijk te bestuderen zijn. Verder heb ik, naast computationele studies, zowel 2D als 3D weefselculturen gebruikt. Ik heb een 3D-weefselmodel gebruikt ([Hoofdstuk 3](#)) omdat in dit model cellen worden gekweekt als aggregaten van enkele of meerdere celtypen die cel-celcontact mogelijk maken. Bovendien maakt het 3D-model proliferatie mogelijk in een meer fysiologisch relevante geometrie die de productie van extracellulaire matrixeiwitten stimuleert.

(i) De rol van CAP in signaalroutes. In het eerste deel van mijn proefschrift hebben we vastgesteld dat CAP de migratie van menselijke gingivale fibroblasten (Eng: human gingival fibroblasts, HGF's) versnelt ([Hoofdstuk 4](#)). HGF's die gedurende 3 minuten met CAP werden behandeld, migreerden sneller naar elkaar over de kloof dan die in de controlegroep en de behandelingsgroep van 5 minuten, op dag 1 en 3. Uit deze studie blijkt dat een lage dosis CAP-behandeling de HGF-proliferatie niet afremt. Het migratie-effect zou kunnen worden ondersteund door de vorming van nieuwe myogenese en de afbraak van extracellulaire matrix (ECM). Er zijn drie stappen betrokken bij de

migratie van de HGF's. De eerste stap is het stoppen van de celcyclus, veroorzaakt door de lage dosis CAP-geproduceerde RONS die niet dodelijk is voor cellen. De tweede stap is ECM-verstoring voor het opzetten van het migrerende bed voor eenvoudiger transport van cellen. Ten slotte vindt HGF-migratie plaats als gevolg van een naar buiten migrerende signaalcascade. De HGF's komen los en verplaatsen zich naar het midden van de wonde, totdat de wondsluiting is voltooid. Over het algemeen helpen deze synergetische werkingsmechanismen van CAP bij het creëren van gunstige wondbedden en resulteren ze in verbeterde wondgenezing.

(ii) CAP veroorzaakt oxidatie-gemedieerde celdood. De RONS geproduceerd door CAP interageren aanvankelijk met het buitenoppervlak van cellen, d.w.z. het fosfolipide dubbellaagmembraan, en induceren de oxidatie ervan. De oxidatie van fosfolipiden toont aan dat celmembranen met hogere fracties cholesterol (zoals typisch voor normale cellen) worden beschermd tegen porievorming. Wanneer daarentegen lagere concentraties cholesterol aanwezig zijn (zoals meestal het geval is bij kankercellen), is het celmembraan kwetsbaarder voor oxidatieve stress en bevordert het de vorming van poriën. De poriën die in het celmembraan worden gegenereerd, vergemakkelijken de doorgang van plasma-gegenereerde RONS naar het intracellulaire compartiment, waar ze verdere oxidatieve schade aan cellen kunnen veroorzaken. Bovendien maakt deze porievorming ook een betere transdermale geneesmiddelafgifte mogelijk. In [Hoofdstuk 5](#) liet ik zien dat RONS aanwezig in plasma-behandelde PBS (PT-PBS) (bv. H_2O_2 , NO_3^- and NO_2^- ionen) het celmembraan oxideren (lipide-peroxidatie) en de permeatie van het antikanker-geneesmiddel melittine (MEL) door de lipide dubbellaag bevorderen. Daarom kan de therapeutische dosis van MEL, nodig om een cytotoxisch effect in kankercellen uit te oefenen, verlaagd worden na behandeling met PT-PBS. De synergie tussen MEL en CAP wordt toegeschreven aan de verandering in membraanintegriteit na peroxidatie van de membraanlipiden door de RONS aanwezig in PT-PBS. Als gevolg hiervan neemt de MEL-translocatiesnelheid door het celmembraan aanzienlijk toe, zoals aangetoond door “umbrella sampling” moleculaire dynamica (MD) simulaties. Daarom kunnen bij lagere behandelingsdoses meer MEL-moleculen in de cel doordringen.

Verder speelt overmatige lipide-peroxidatie een sleutelrol bij het reguleren van niet-apoptotische celdoodmechanismen, zoals ferroptose veroorzaakt door verslechtering van de redoxbalans. In [Hoofdstuk 6](#) concentreerde ik me verder op RONS, geproduceerd door CAP, die direct interageren met het celmembraan en een verhoogd niveau van Fe^{2+} en lipideperoxidatie veroorzaken, wat uiteindelijk ferroptose induceert door uitputting van GSH/GPX4 en zijn regulerende redoxfactor HMOX1. Doorgaans induceert HMOX1 een cytoprotectieve antioxidantrespons door heem af te breken om koolmonoxide, biliverdine en Fe^{2+} te genereren onder milde oxidatieve stressomstandigheden. Wanneer de oxidatieve stress en lipideperoxidatieniveaus echter toenemen tot boven de homeostatische stresstolerantie, kan de antioxidantcytoprotectie leiden tot ferroptotische celdood. Overmatige hoeveelheden HMOX1 veroorzaken bijvoorbeeld sensibilisatie van ferroptose als gevolg van een onevenwichtige toename van Fe^{2+} -niveaus, onvoldoende buffercapaciteit door ferritine en ongecontroleerde productie van hydroxylradicalen via de Fenton-reactie. Daarentegen gingen de effecten van CAP verloren in aanwezigheid van de ferroptose-remmer Fer-1, wat inderdaad aantoont dat de overmatige lipideperoxidatie die wordt geïnduceerd door CAP gedeeltelijk te wijten kan zijn aan de inactivatie van het GPX4/GSH-lipideherstel-enzymstelsel, dat verantwoordelijk is voor de inductie van ferroptotische celdood. Om meer inzicht te krijgen in de aantasting van GPX4-functies door CAP-geïnduceerde RONS, heb ik MD simulaties uitgevoerd. Deze methode maakt het mogelijk om conformationele veranderingen in de katalytische actieve “pocket” van GPX4 na oxidatie te voorspellen. Beweging en rotatie van de zijketen van cysteïnezuur en 6-hydroxytryptofaan in de geoxideerde structuren resulteert in een herschikking van de omringende aminozuren, waardoor de $\text{C}\alpha$ -afstanden tussen de katalytische machinerie van GPX4 toenemen. Monitoring van de $\text{C}\alpha$ -afstanden toont aan dat oxidatie van de katalytische residuen een cruciale rol speelt in de stabiliteit van GPX4. In het bijzonder zijn de $\text{C}\alpha$ -afstanden tussen de katalytische triade relatief lang voor het maken van een H-binding daartussen. Bovendien is de RMSD van de katalytische machinerie van GPX4 in de originele structuur stabielere dan in de geoxideerde structuur. Deze verminderde stabiliteit in geval van oxidatie kan bijdragen aan een verminderde expressie van GPX4 die wordt waargenomen in de immunohistochemische analyse van de GPX4-expressie.

De reductie en activering van signaalmoleculen gerelateerd aan antioxidanten, zoals GSH/GPX4 of HMOX1, speelt ook een belangrijke rol bij de resistentie tegen geneesmiddelen, omdat het de oxidatie-gemedieerde respons kan in- en uitschakelen, afhankelijk van de intracellulaire redoxstatus. Hoge intracellulaire GSH/GPX4-niveaus in kankercellen leiden tot epitheliale-mesenchymale overgang, wat resulteert in tumorprogressie, metastase en chemoresistentie. In **Hoofdstuk 7** liet ik zien dat CAP de gevoeligheid van Temozolomide (TMZ) in een 3D sferoïde tumormodel verhoogt (d.w.z. een hogere cytotoxiciteit en sferoïde krimp werd verkregen wanneer TMZ en CAP samen werden toegediend) op een dosis- en tijdsafhankelijke manier, te wijten aan de verhoogde ROS-niveaus en een remming van de GSH/GPX4-antioxidantenmachinerie. Mogelijk induceert de combinatiebehandeling overmatige intracellulaire RONS, die vervolgens een cruciale rol kunnen spelen bij door oxidatieve stress geïnduceerde celdood. Samen met het verhogen van de endogene ROS-omgeving resulteert het remmen van het antioxidantensysteem in de accumulatie van hydroxyl (OH) radicalen en bevordert het DNA-oxidatie, wat aangetoond wordt door de hoge niveaus van 8-hydroxy-2'-deoxyguanosine (8-OHdG) en de expressie van 8-Oxo-2'-deoxyguanosine (8-oxo-dG), de meest representatieve biomarkers van oxidatieve schade aan DNA.

Vooruitzichten voor toekomstig werk

In dit proefschrift had ik als doel om verschillende mechanismen op moleculair niveau op te helderen voor toepassing van plasmageneeskunde, voornamelijk voor wondgenezing en verbetering van transdermale medicijnafgifte bij kankerbehandeling, die hoofdzakelijk wordt gemedieerd via reactieve zuurstof- en stikstofdeeltjes (RONS). Elektrische velden en andere componenten van CAP mogen echter niet buiten beschouwing worden gelaten omdat is aangetoond dat ze ook poriënvorming in het celmembraan kunnen veroorzaken. Hierdoor kunnen RONS de cellen binnendringen en sterke effecten veroorzaken op andere biomoleculen in de cellen.

CAP heeft opmerkelijke vooruitgang geboekt op het gebied van plasmageneeskunde, zoals inactivatie van bacteriën, behandeling van chronische wonden en selectieve doding in kankercellen. Er is echter nog veel meer onderzoek nodig naar de

interacties van CAP met prokaryote en eukaryote cellen om een volledig beeld te krijgen van de werking van plasmageneeskunde. Naar mijn mening moet toekomstig onderzoek zich vooral focussen op: (i) de opheldering van CAP-getriggerde signaalroutes die kunnen leiden tot apoptose of necrose in kankercellen; (ii) het bestuderen van het effect van RONS in combinatie met andere componenten van CAP, zoals elektrische velden, UV, enz.; (iii) onderzoek naar langetermijneffecten van CAP op macromoleculen zoals DNA en eiwitten; (iv) het uitzoeken van de epigenetische effecten van CAP op normale cellen; en (v) beoordeling van CAP-blootstelling op immuuncellen. In de laatste twee decennia heeft het gebied van de plasmageneeskunde veel vooruitgang geboekt in nieuwe inzichten naar de onderliggende mechanismen. Plasmageneesmiddel lijkt nu klaar voor meer klinische testen, zodat het de arena van de gezondheidszorg kan betreden. De vele *in vitro* en *in vivo* onderzoeken, uitgevoerd door verschillende onderzoeksgroepen in de voorbije decennia zijn erg belangrijk voor de plasmageneeskunde, als we willen dat plasmatechnologie een echte adjuvante behandelingstherapie wordt in klinische context.

Academic Curriculum vitae

❖ *List of published articles in international peer-reviewed scientific journals*

1. **Priyanka Shaw**, Naresh Kumar, Claudina Perez-Novo, Emilie Logie, Angela Privat-Maldonado, Sylvia Dewilde, Evelien Smits, Wim Vanden Berghe, Annemie Bogaerts “Physical plasma-derived oxidants sensitize pancreatic cancer cells to ferroptotic cell death” *Free Radical Biology and Medicine*, 166, p. 187-200, 2021.
2. **Priyanka Shaw**, Naresh Kumar, Angela Privat-Maldonado, Evelien Smits, Annemie Bogaerts “Cold Atmospheric Plasma Increases Temozolomide Sensitivity of Three-Dimensional Glioblastoma Spheroids via Oxidative Stress-Mediated DNA Damage” *Cancers* 13(8), p. 1780, 2021.
3. **Priyanka Shaw**, Naresh Kumar, Sohail Mumtaz, Jun Sup Lim, Jung Hyun, Jang, Doyoung Kim, Bidya Dhar Sahu, Annemie Bogaerts, and Eun Ha Choi “Evaluation of non-thermal effect of microwave radiation and its mode of action in bacterial cell inactivation” *Scientific Reports* 11(1), p. 1-12, 2021.
4. Maksudbek Yusupov, Angela Privat-Maldonado, Rodrigo Cordeiro, Hanne Verswyvel, **Priyanka Shaw**, Jamoliddin Razzokov, Evelien Smits, Annemie Bogaerts “Oxidative damage to hyaluronan–CD44 interactions as an underlying mechanism of action of oxidative stress-inducing cancer therapy” *Redox Biology* 43, p. 101968, 2021.
5. Emilie Logie, Chandra S Chirumamilla, Claudina Perez-Novo, **Priyanka Shaw**, Ken Declerck, Ajay Palagani, Savithri Rangarajan, Bart Cuypers, Nicolas De Neuter, Fazil Mobashar Hussain Urf Turabe, Navin Kumar Verma, Annemie Bogaerts, Kris Laukens, Fritz Offner, Pieter Van Vlierberghe, Xaveer Van Ostade, Wim Vanden Berghe “Covalent Cysteine Targeting of Bruton’s Tyrosine Kinase (BTK) Family by Withaferin-A Reduces Survival of Glucocorticoid-Resistant Multiple Myeloma MM1 Cells” *Cancers* 13(7), p. 1618, 2021.
6. **Priyanka Shaw**, Naresh Kumar, Dietmar Hammerschmid, Angela Privat-Maldonado, Sylvia Dewilde, Annemie Bogaerts “Synergistic effects of melittin

- and plasma treatment: A promising approach for cancer therapy” *Cancers* 11(8), p. 1109, 2019.
7. **Priyanka Shaw**, Naresh Kumar, Hyong Sin Kwak, Han Sup Uhm & Eun Ha Choi “Bacterial inactivation by plasma treated water enhanced by reactive nitrogen species” *ScientificReports* 8(1), p. 11268, 2018
 8. **Priyanka Shaw**, Naresh Kumar, Jamoliddin Razzokov, Maksudbek Yusupov, Pankaj Attri, Han Sup Uhm, Eun Ha Choi, Annemie Bogaerts “Enhancement of cellular glucose uptake by reactive species: A promising approach for diabetes therapy” *RSC Advances* 8(18), p. 9887-9894, 2018.
 9. **Priyanka Shaw**, Naresh Kumar, Pankaj Attri, Han Sup Uhm, & Eun Ha Choi “Influence of nitric oxide generated through microwave plasma on L6 skeletal muscle cell differentiation via oxidative signaling pathways” *ScientificReports* 7(1), p. 542, 2017.
 10. Dharmendra K. Yadav, Reeta Rai, Naresh Kumar, Surjeet Singh, Sanjeev Misra, Praveen Sharma, **Priyanka Shaw**, Horacio Pérez-Sánchez, Ricardo L. Mancera, Eun Ha Choi, Mi-hyun Kim & Ramendra Pratap. “New arylated benzo(h)quinolines induce anti-cancer activity by oxidative stress-mediated DNA damage.” *Scientific Reports* 6(1), p. 1-13, 2016.

❖ List of unpublished articles (in preparation or submitted)

11. Ihn Han, In-Seok Song, Seung Ah Choi, Taebok Lee, Suk Ji, Maksudbek Yusupov, **Priyanka Shaw**, Annemie Bogaerts, Eun Ha Choi, and Jae Jun Ryu “Enhanced Migration of Human Gingival Fibroblast by Non-Thermal Biocompatible Dielectric Barrier Discharge Plasma” *Cell Death and Differentiation*, 2021.
12. **Priyanka Shaw**, Naresh Kumar, Maxime Sahun, Angela Privat-Maldonado, Evelien Smits, Annemie Bogaerts “Targeting the keepers of redox balance: key for oxidative stress-inducing therapies” *Free Radical Biology and Medicine*, 2021.

❖ *List of abstracts for poster presentations*

1. Priyanka Shaw, Naresh Kumar, Angela Privat-Maldonado, Sylvia Dewilde, and Annemie Bogaerts "In Silico and In Vitro Identification of Anticancer Target of Cold Plasma" at 8th International Conference of Plasma Medicine (Online conference), August, Seoul (Republic of Korea), 2021.
2. Priyanka Shaw, Naresh Kumar, Angela Privat-Maldonado, Evelien Smits, and Annemie Bogaerts "Plasma-derived oxidants induce tumor cell death via oxidative stress-mediated DNA damage in a three-dimensional model of human glioblastoma tumor" for the 7th International Workshop on Plasma for Cancer Treatment 2021 (IWPCT 2021), July, Barcelona (Spain), 2021.
3. Priyanka Shaw, Naresh Kumar, Dietmar Hammerschmid, Sylvia Dewilde and Annemie Bogaerts, Synergistic effects of Bee venom and reactive oxygen and nitrogen species on the membrane fluidity: A promising approach for cancer therapy, 2019 International Forum on Functional Materials (IFFM 2019), June, Gangneung City (Republic of Korea), 2019.
4. Priyanka Shaw, Naresh Kumar, Sylvia Dewilde and Annemie Bogaerts, Interaction and translocation of Melittin with or without oxidized membranes: Implications for cancer therapy, 8th Young Professionals Workshop on Plasma Medicine - Frontiers in Redox Biology and Medicine (FiRBaM 2019), August, Greifswald (Germany), 2019.
5. Naresh Kumar, Priyanka Shaw, Sylvia Dewilde and Annemie Bogaerts, Enhancement of cellular translocation of bee venom by reactive species: a promising approach for cancer therapy, 6th International Workshop on Plasma for Cancer Treatment (IWPCT 2019), April, Antwerp (Belgium), 2019.
6. Priyanka Shaw, Naresh Kumar, Sylvia Dewilde and Annemie Bogaerts, Interaction and translocation of melittin with or without oxidized membranes: implications for cancer therapy, Belgian Association for Cancer Research, February, Antwerp (Belgium), 2019.
7. Naresh Kumar, Priyanka Shaw, Eun Ha Choi, Pankaj Attri, and A. Bogaerts, The stimulation of L6 Skeletal Muscles Cell Differentiation by Non thermal plasma

- modified electrically conductive fibers, iPlasmaNano-VIII - 8th International Conference on Plasma Nanoscience, July, Antwerp (Belgium), 2017.
8. Priyanka Shaw, Naresh Kumar, Pankaj Attri and Eun Ha Choi, Enhancement of Nitric Oxide with non-thermal plasma jet and its effect on Escherichia coli and cancer cells inactivation, The 50th Winter annual conferences of the Korean Vacuum Society, February, Seoul (Republic of Korea), 2016.
 9. Priyanka Shaw, Suck Woo Lee, Naresh Kumar, Han Sup Uhm and Eun Ha Choi “Output characteristics of the high power microwave generated from the Virtual cathode device” The 20th Annual Conferences of the International Vacuum Society (IVC-20), August, Busan (Republic of Korea), 2016.
 10. Priyanka Shaw, Naresh Kumar, Pankaj Attri, Ji Hoon Park, Han Sup Uhm and Eun Ha Choi, Output characteristics of the high power microwave generated from the Virtual cathode device, International form on functional material, June, Jeju Island (Republic of Korea), 2015.
 11. Priyanka Shaw, Naresh Kumar, Pankaj Attri and Eun Ha Choi, Enhancement of Nitric Oxide with non-thermal plasma jet and its effect on Escherichia inactivation, The 49th Summer Annual Conferences of the Korean Vacuum Society, August, Changwon (Republic of Korea), 2015.
 12. Naresh Kumar, Priyanka Shaw, Pankaj Attri, Han Sup Uhm and Eun Ha Choi*, Role of Exogenous Nitric Oxide Generated through Microwaves Plasma Activate the Oxidative Signaling Components in Differentiation of Myoblast cells into Myotube. The 49th Summer Annual Conferences of the Korean Vacuum Society, August, Changwon (Republic of Korea), 2015
 13. Priyanka Shaw, Naresh Kumar, Pankaj Attri, Ku Y. Baik, Ji Hoon Park, Eun Ha Choi and Han Sup Uhm, Influence of nitric oxide generated through microwave plasma on L6 skeletal muscles cell differentiation via oxidative signalling pathways, International Form on Functional Material, February, Jeju Island (Republic of Korea), 2015

❖ List of abstracts for oral presentations

1. Priyanka Shaw, Plasma-derived oxidants induce tumor cell death via oxidative stress-mediated DNA damage in a three-dimensional model of human glioblastoma tumor for the International Workshop on Plasma for Cancer Treatment 2021 (IWPCT 2021), July, Barcelona (Spain), 2021.
2. Priyanka Shaw, Naresh Kumar, Sylvia Dewilde and Annemie Bogaerts, Interaction and translocation of Melittin with or without oxidized membranes: Implications for cancer therapy, 8th Young Professionals Workshop on Plasma Medicine - Frontiers in Redox Biology and Medicine (FiRBaM 2019), August, Greifswald (Germany), 2019.
3. Priyanka Shaw, Naresh Kumar, Dietmar Hammerschmid, Sylvia Dewilde and Annemie Bogaerts, Synergistic effects of Bee venom and reactive oxygen and nitrogen species on the membrane fluidity: A promising approach for cancer therapy, 2019 International Forum on Functional Materials (IFFM 2019), June, Gangneung City (Republic of Korea), 2019.

❖ List of scientific awards/grants

1. Best Student paper award for the poster "In Silico and In Vitro Identification of Anticancer Target of Cold Plasma" at 8th International Conference of Plasma Medicine (online conference), 2021, prize money 150 USD.
2. Young Scientist Award (NSF/YSA/2021/02) for "Cold Atmospheric Plasma Interactions in Cancer Treatment by means of Computer Modelling" by Nature Science Foundation, Coimbatore - 641 004, Tamil Nadu, India. (2021)
3. Best poster award for the poster "Synergistic effects of Bee venom and reactive oxygen and nitrogen species on the membrane fluidity: A promising approach for cancer therapy" presented at IFFM 2019, Gangneung Korea, prize money 50,000 Korean Won.
4. IVC Student award for the poster "Output characteristics of the high power microwave generated from the Virtual cathode device" in 20th Annual Conferences of the International Vacuum Society (IVC-20), Korea (2016), prize money 3,80,000 Korean Won.

5. Outstanding Poster Presentation award for the poster “Influence of nitric oxide generated through microwave plasma on L6 skeletal muscles cell differentiation via oxidative signaling pathways.” in IFFM, (International forum on functional material), Jeju, Korea (2015), prize money 30,000 Korean Won.

❖ Peer reviewer of

- ✓ Cancers (Impact factor: 7);
- ✓ Journal of Personalized Medicine (Impact factor: 5)
- ✓ Scientific Reports, nature communication (Impact factor 4.5);
- ✓ Biomolecules (Impact factor: 4.5).

❖ Research visit

June-July (2019): Plasma Bioscience Research Center (PBRC) group of Kwangwoon University (South Korea) for 21 days under the supervision of Prof. Dr. Eun Ha Choi with a Belgian-Korean (FWO-KRF) research grant.

References

- 1 Genheden, S., Reymer, A., Saenz-Méndez, P. & Eriksson, L. A. Computational chemistry and molecular modelling basics. (2017).
- 2 Laskowski, R. A. & Swindells, M. B. (ACS Publications, 2011).
- 3 Pluhackova, K. & Böckmann, R. A. Biomembranes in atomistic and coarse-grained simulations. *Journal of physics: condensed matter* 27, 323103 (2015).
- 4 Weidinger, A. & Kozlov, A. V. Biological activities of reactive oxygen and nitrogen species: oxidative stress versus signal transduction. *Biomolecules* 5, 472-484 (2015).
- 5 Bhattacharyya, A., Chattopadhyay, R., Mitra, S. & Crowe, S. E. Oxidative stress: an essential factor in the pathogenesis of gastrointestinal mucosal diseases. *Physiological reviews* 94, 329-354 (2014).
- 6 Pourova, J., Kottova, M., Voprsalova, M. & Pour, M. Reactive oxygen and nitrogen species in normal physiological processes. *Acta physiologica* 198, 15-35 (2010).
- 7 Ozcan, A. & Ogun, M. Biochemistry of reactive oxygen and nitrogen species. *Basic principles and clinical significance of oxidative stress* 3, 37-58 (2015).
- 8 Hatziagapiou, K., Kakouri, E., Lambrou, G. I., Bethanis, K. & Tarantilis, P. A. Antioxidant properties of *Crocus sativus* L. and its constituents and relevance to neurodegenerative diseases; focus on Alzheimer's and Parkinson's disease. *Current neuropharmacology* 17, 377-402 (2019).
- 9 Shaw, P. *et al.* Synergistic effects of melittin and plasma treatment: A promising approach for cancer therapy. *Cancers* 11, 1109 (2019).
- 10 Shaw, P., Kumar, N., Privat-Maldonado, A., Smits, E. & Bogaerts, A. Cold Atmospheric Plasma Increases Temozolomide Sensitivity of Three-Dimensional Glioblastoma Spheroids via Oxidative Stress-Mediated DNA Damage. *Cancers* 13, 1780 (2021).
- 11 Pham-Huy, L. A., He, H. & Pham-Huy, C. Free radicals, antioxidants in disease and health. *International journal of biomedical science: IJBS* 4, 89 (2008).
- 12 Mazumder, P. M., Rathinavelusamy, P. & Sasmal, D. Role of antioxidants in phytomedicine with special reference to antidiabetic herbs. *Asian Pacific Journal of Tropical Disease* 2, S969-S979 (2012).
- 13 Hameister, R., Kaur, C., Dheen, S. T., Lohmann, C. H. & Singh, G. Reactive oxygen/nitrogen species (ROS/RNS) and oxidative stress in arthroplasty. *Journal of Biomedical Materials Research Part B: Applied Biomaterials* 108, 2073-2087 (2020).
- 14 Phaniendra, A., Jestadi, D. B. & Periyasamy, L. Free radicals: properties, sources, targets, and their implication in various diseases. *Indian journal of clinical biochemistry* 30, 11-26 (2015).
- 15 Shaw, P. *et al.* Bacterial inactivation by plasma treated water enhanced by reactive nitrogen species. *Scientific reports* 8, 11268-11268, doi:10.1038/s41598-018-29549-6 (2018).
- 16 Heslin, C. *et al.* Quantitative assessment of blood coagulation by cold atmospheric plasma. *Plasma Medicine* 4 (2014).

- 17 Stratmann, B. *et al.* Effect of Cold Atmospheric Plasma Therapy vs Standard Therapy Placebo on Wound Healing in Patients With Diabetic Foot Ulcers: A Randomized Clinical Trial. *JAMA Netw Open* 3, e2010411-e2010411, doi:10.1001/jamanetworkopen.2020.10411 (2020).
- 18 Geback, T., Schulz, M. M., Koumoutsakos, P. & Detmar, M. TScratch: a novel and simple software tool for automated analysis of monolayer wound healing assays. *Biotechniques* 46, 265-274, doi:10.2144/000113083 (2009).
- 19 Bekeschus, S., Schmidt, A., Weltmann, K.-D. & von Woedtke, T. The plasma jet kINPen – A powerful tool for wound healing. 4, 19-28, doi:10.1016/j.cpme.2016.01.001 (2016).
- 20 Lou, B.-S. *et al.* Helium/argon-generated cold atmospheric plasma facilitates cutaneous wound healing. *Frontiers in bioengineering and biotechnology* 8, 683 (2020).
- 21 Arndt, S. *et al.* Cold atmospheric plasma (CAP) changes gene expression of key molecules of the wound healing machinery and improves wound healing in vitro and in vivo. *PloS one* 8, e79325 (2013).
- 22 Kumar, N., Attri, P., Choi, E. H. & Uhm, H. S. Influence of water vapour with non-thermal plasma jet on the apoptosis of SK-BR-3 breast cancer cells. *RSC Advances* 5, 14670-14677 (2015).
- 23 Kumar, N. *et al.* Induced apoptosis in melanocytes cancer cell and oxidation in biomolecules through deuterium oxide generated from atmospheric pressure non-thermal plasma jet. *Scientific reports* 4, 7589, doi:10.1038/srep07589 (2014).
- 24 Kumar, N., Attri, P., Dewilde, S. & Bogaerts, A. Inactivation of human pancreatic ductal adenocarcinoma with atmospheric plasma treated media and water: A comparative study. *Journal of Physics D: Applied Physics* 51, 255401 (2018).
- 25 Kumar, N. *et al.* The action of microsecond-pulsed plasma-activated media on the inactivation of human lung cancer cells. *Journal of Physics D: Applied Physics* 49, 115401, doi:10.1088/0022-3727/49/11/115401 (2016).
- 26 Chen, G. *et al.* Transdermal cold atmospheric plasma-mediated immune checkpoint blockade therapy. *Proceedings of the National Academy of Sciences* 117, 3687-3692 (2020).
- 27 Van Loenhout, J. *et al.* Cold atmospheric plasma-treated PBS eliminates immunosuppressive pancreatic stellate cells and induces immunogenic cell death of pancreatic cancer cells. *Cancers* 11, 1597 (2019).
- 28 Filipić, A. *et al.* Cold atmospheric plasma as a novel method for inactivation of potato virus Y in water samples. *Food and environmental virology* 11, 220-228 (2019).
- 29 Bunz, O. *et al.* Cold atmospheric plasma as antiviral therapy—effect on human herpes simplex virus type 1. *The Journal of general virology* 101, 208 (2020).
- 30 Bunz, O., Mese, K., Zhang, W., Piwowarczyk, A. & Ehrhardt, A. Effect of cold atmospheric plasma (CAP) on human adenoviruses is adenovirus type-dependent. *PLoS One* 13, e0202352 (2018).

- 31 Mann, M. S. *et al.* Introduction to DIN-specification 91315 based on the
characterization of the plasma jet kINPen® MED. *Clinical Plasma Medicine* 4,
35-45 (2016).
- 32 Schönebeck, R. in *Comprehensive Clinical Plasma Medicine* 485-494
(Springer, 2018).
- 33 Brehmer, F. *et al.* Alleviation of chronic venous leg ulcers with a hand-held
dielectric barrier discharge plasma generator (PlasmaDerm® VU-2010): results
of a monocentric, two-armed, open, prospective, randomized and controlled
trial (NCT 01415622). *Journal of the European Academy of Dermatology and
Venereology* 29, 148-155 (2015).
- 34 Wandke, D. in *Comprehensive Clinical Plasma Medicine* 495-502 (Springer,
2018).
- 35 Arndt, S., Schmidt, A., Karrer, S. & von Woedtke, T. Comparing two different
plasma devices kINPen and Adtec SteriPlas regarding their molecular and
cellular effects on wound healing. *Clinical Plasma Medicine* 9, 24-33 (2018).
- 36 Arndt, S., Schmidt, A., Karrer, S. & von Woedtke, T. *Clinical Plasma
Medicine*.
- 37 Golda, J., Sgonina, K., Held, J., Benedikt, J. & Schulz-von der Gathen, V.
Treating surfaces with a cold atmospheric pressure plasma using the COST-jet.
JoVE (Journal of Visualized Experiments), e61801 (2020).
- 38 Florian, J., Merbahi, N., Wattiaux, G., Plewa, J.-M. & Yousfi, M.
Comparative studies of double dielectric barrier discharge and microwave
argon plasma jets at atmospheric pressure for biomedical applications. *IEEE
Transactions on Plasma Science* 43, 3332-3338 (2015).
- 39 Moreau, E., Sosa, R. & Artana, G. Electric wind produced by surface plasma
actuators: a new dielectric barrier discharge based on a three-electrode
geometry. *Journal of Physics D: Applied Physics* 41, 115204 (2008).
- 40 Eden, J. G. & Park, S. Microcavity plasma devices and arrays: A new realm of
plasma physics and photonic applications. *Plasma physics and controlled
fusion* 47, B83 (2005).
- 41 Becker, K., Zhu, W. & Lopez, J. Microplasmas: Environmental and biological
applications. *Plasma Phys. Controlled Fusion* 47, B513-B523 (2005).
- 42 Kunhardt, E. E. Generation of large-volume, atmospheric-pressure,
nonequilibrium plasmas. *IEEE transactions on plasma science* 28, 189-200
(2000).
- 43 Itoh, H., Teranishi, K. & Suzuki, S. Discharge plasmas generated by
piezoelectric transformers and their applications. *Plasma Sources Science and
Technology* 15, S51 (2006).
- 44 Kumar, N. *et al.* Physical plasma-derived oxidants sensitize pancreatic cancer
cells to ferroptotic cell death. *Free Radical Biology and Medicine* 166, 187-200
(2021).
- 45 Xu, S. *et al.* Cold atmospheric plasma-activated Ringer's solution inhibits the
proliferation of osteosarcoma cells through the mitochondrial apoptosis
pathway. *Oncology reports* 43, 1683-1691 (2020).
- 46 Bisag, A. *et al.* Plasma-activated Ringer's lactate solution displays a selective
cytotoxic effect on ovarian cancer cells. *Cancers* 12, 476 (2020).

- 47 Rezaei, F., Vanraes, P., Nikiforov, A., Morent, R. & De Geyter, N. Applications of plasma-liquid systems: A review. *Materials* 12, 2751 (2019).
- 48 Van Boxem, W. *et al.* Anti-cancer capacity of plasma-treated PBS: effect of chemical composition on cancer cell cytotoxicity. *Scientific reports* 7, 16478-16478, doi:10.1038/s41598-017-16758-8 (2017).
- 49 Hoffmann, C., Berganza, C. & Zhang, J. Cold Atmospheric Plasma: methods of production and application in dentistry and oncology. *Medical gas research* 3, 1-15 (2013).
- 50 Jungbauer, G. *et al.* The Antimicrobial Effect of Cold Atmospheric Plasma against Dental Pathogens—A Systematic Review of In-Vitro Studies. *Antibiotics* 10, 211 (2021).
- 51 Li, H. P. *et al.* Translational plasma stomatology: applications of cold atmospheric plasmas in dentistry and their extension. *High voltage* 2, 188-199 (2017).
- 52 Hong, Y. *et al.* Sterilization effect of atmospheric plasma on Escherichia coli and Bacillus subtilis endospores. *Letters in applied microbiology* 48, 33-37 (2009).
- 53 Kostov, K. G. *et al.* Inactivation of Candida albicans by cold atmospheric pressure plasma jet. *IEEE Transactions on plasma science* 43, 770-775 (2014).
- 54 Brown, P. *et al.* Iatrogenic Creutzfeldt–Jakob disease at the millennium. *Neurology* 55, 1075-1081 (2000).
- 55 Smith, A., Dickson, M., Aitken, J. & Bagg, J. Contaminated dental instruments. *Journal of Hospital Infection* 51, 233-235 (2002).
- 56 Deng, X.-T., Shi, J. & Kong, M. G. Protein destruction by a helium atmospheric pressure glow discharge: capability and mechanisms. *Journal of applied physics* 101, 074701 (2007).
- 57 Deng, X.-T., Shi, J., Chen, H. & Kong, M. G. Protein destruction by atmospheric pressure glow discharges. *Applied physics letters* 90, 013903 (2007).
- 58 Duchesne, C., Banzet, S., Lataillade, J. J., Rousseau, A. & Frescaline, N. Cold atmospheric plasma modulates endothelial nitric oxide synthase signalling and enhances burn wound neovascularisation. *The Journal of pathology* 249, 368-380 (2019).
- 59 Shekhter, A. B., Serezhenkov, V. A., Rudenko, T. G., Pekshev, A. V. & Vanin, A. F. Beneficial effect of gaseous nitric oxide on the healing of skin wounds. *Nitric oxide* 12, 210-219 (2005).
- 60 Shekhter, A., Kabisov, R., Pekshev, A., Kozlov, N. & Perov, Y. L. Experimental and clinical validation of plasmadynamic therapy of wounds with nitric oxide. *Bulletin of Experimental Biology and Medicine* 126, 829-834 (1998).
- 61 Van der Paal, J., Neyts, E. C., Verlackt, C. C. & Bogaerts, A. Effect of lipid peroxidation on membrane permeability of cancer and normal cells subjected to oxidative stress. *Chemical science* 7, 489-498 (2016).
- 62 Biscop, E. *et al.* Influence of Cell Type and Culture Medium on Determining Cancer Selectivity of Cold Atmospheric Plasma Treatment. *Cancers* 11, 1287, doi:10.3390/cancers11091287 (2019).

- 63 Van der Paal, J., Verheyen, C., Neyts, E. C. & Bogaerts, A. Hampering effect of cholesterol on the permeation of reactive oxygen species through phospholipids bilayer: possible explanation for plasma cancer selectivity. *Scientific reports* 7, 1-11 (2017).
- 64 Cairns, R. A., Harris, I. S. & Mak, T. W. Regulation of cancer cell metabolism. *Nature Reviews Cancer* 11, 85-95 (2011).
- 65 Liedtke, K. R. *et al.* Cold physical plasma selectively elicits apoptosis in murine pancreatic cancer cells in vitro and in ovo. *Anticancer research* 38, 5655-5663 (2018).
- 66 Kerr, J. F., Winterford, C. M. & Harmon, B. V. Apoptosis. Its significance in cancer and cancer therapy. *Cancer* 73, 2013-2026 (1994).
- 67 Albright, C. D., Salganik, R. I. & Van Dyke, T. Dietary depletion of vitamin E and vitamin A inhibits mammary tumor growth and metastasis in transgenic mice. *The Journal of nutrition* 134, 1139-1144 (2004).
- 68 Wlassoff, W. A. *et al.* Hydrogen peroxide overproduced in breast cancer cells can serve as an anticancer prodrug generating apoptosis-stimulating hydroxyl radicals under the effect of tamoxifen-ferrocene conjugate. *Journal of Pharmacy and Pharmacology* 59, 1549-1553 (2007).
- 69 Benhar, M., Engelberg, D. & Levitzki, A. ROS, stress-activated kinases and stress signaling in cancer. *EMBO reports* 3, 420-425 (2002).
- 70 Sladek, R. E., Stoffels, E., Walraven, R., Tielbeek, P. J. & Koolhoven, R. A. Plasma treatment of dental cavities: a feasibility study. *IEEE Transactions on plasma science* 32, 1540-1543 (2004).
- 71 Hogg, N. The biochemistry and physiology of S-nitrosothiols. *Annual review of pharmacology and toxicology* 42, 585-600 (2002).
- 72 Ischiropoulos, H. Biological tyrosine nitration: a pathophysiological function of nitric oxide and reactive oxygen species. *Archives of biochemistry and biophysics* 356, 1-11 (1998).
- 73 Kumar, N., Kaushik, N. K., Park, G., Choi, E. H. & Uhm, H. S. Enhancement of glucose uptake in skeletal muscle L6 cells and insulin secretion in pancreatic hamster-insulinoma-transfected cells by application of non-thermal plasma jet. *Applied Physics Letters* 103, 203701 (2013).
- 74 Locigno, E. J., Zweier, J. L. & Villamena, F. A. Nitric oxide release from the unimolecular decomposition of the superoxide radical anion adduct of cyclic nitrones in aqueous medium. *Organic & biomolecular chemistry* 3, 3220-3227 (2005).
- 75 Villamena, F. A. & Zweier, J. L. Detection of reactive oxygen and nitrogen species by EPR spin trapping. *Antioxidants and redox signaling* 6, 619-629 (2004).
- 76 Forman, H. J. Use and abuse of exogenous H₂O₂ in studies of signal transduction. *Free Radical Biology and Medicine* 42, 926-932 (2007).
- 77 Reth, M. & Dick, T. P. Voltage control for B cell activation. *Nature immunology* 11, 191-192 (2010).
- 78 Holohan, C., Van Schaeybroeck, S., Longley, D. B. & Johnston, P. G. Cancer drug resistance: an evolving paradigm. *Nature Reviews Cancer* 13, 714-726 (2013).

- 79 Bogaerts, A. *et al.* Multi-level molecular modelling for plasma medicine. *Journal of Physics D: Applied Physics* 49, 054002 (2015).
- 80 Maitland, G. C., Maitland, G., Rigby, M., Smith, E. B. & Wakeham, W. *Intermolecular forces: their origin and determination.* (Oxford University Press, USA, 1981).
- 81 Sprik, M. Effective pair potentials and beyond. *Computer simulation in chemical physics*, 211-259 (1993).
- 82 Stone, A. J. (Oxford, 1996).
- 83 Wang, J., Wolf, R. M., Caldwell, J. W., Kollman, P. A. & Case, D. A. Junmei Wang, Romain M. Wolf, James W. Caldwell, Peter A. Kollman, and David A. Case, "Development and testing of a general amber force field" *Journal of Computational Chemistry* (2004) 25 (9) 1157–1174. *Journal of Computational Chemistry* 26, 114-114 (2005).
- 84 Vanommeslaeghe, K. *et al.* CHARMM general force field: A force field for drug-like molecules compatible with the CHARMM all-atom additive biological force fields. *Journal of computational chemistry* 31, 671-690 (2010).
- 85 Jorgensen, W. L., Maxwell, D. S. & Tirado-Rives, J. Development and testing of the OPLS all-atom force field on conformational energetics and properties of organic liquids. *Journal of the American Chemical Society* 118, 11225-11236 (1996).
- 86 Oostenbrink, C., Villa, A., Mark, A. E. & Van Gunsteren, W. F. A biomolecular force field based on the free enthalpy of hydration and solvation: the GROMOS force-field parameter sets 53A5 and 53A6. *Journal of computational chemistry* 25, 1656-1676 (2004).
- 87 Kästner, J. Umbrella sampling. *Wiley Interdisciplinary Reviews: Computational Molecular Science* 1, 932-942 (2011).
- 88 Goodsell, D. S., Morris, G. M. & Olson, A. J. Automated docking of flexible ligands: applications of AutoDock. *Journal of molecular recognition* 9, 1-5 (1996).
- 89 Morris, G. M., Goodsell, D. S., Huey, R. & Olson, A. J. Distributed automated docking of flexible ligands to proteins: parallel applications of AutoDock 2.4. *Journal of computer-aided molecular design* 10, 293-304 (1996).
- 90 De Vries, S. J., Van Dijk, M. & Bonvin, A. M. The HADDOCK web server for data-driven biomolecular docking. *Nature protocols* 5, 883-897 (2010).
- 91 Pierce, B. G., Hourai, Y. & Weng, Z. Accelerating protein docking in ZDOCK using an advanced 3D convolution library. *PloS one* 6, e24657 (2011).
- 92 Pierce, B. G. *et al.* ZDOCK server: interactive docking prediction of protein–protein complexes and symmetric multimers. *Bioinformatics* 30, 1771-1773 (2014).
- 93 Singh, J., Petter, R. & Baillie, T. a. & Whitty, A. The resurgence of covalent drugs. *Nat. Rev. Drug Discov* 10, 307-317 (2011).
- 94 Logie, E. *et al.* Covalent Cysteine Targeting of Bruton’s Tyrosine Kinase (BTK) Family by Withaferin-A Reduces Survival of Glucocorticoid-Resistant Multiple Myeloma MM1 Cells. *Cancers* 13, 1618 (2021).

- 95 Morris, G. M. *et al.* AutoDock4 and AutoDockTools4: Automated docking with selective receptor flexibility. *Journal of computational chemistry* 30, 2785-2791 (2009).
- 96 Hasse, S., Meder, T., Freund, E., von Woedtke, T. & Bekeschus, S. Plasma Treatment Limits Human Melanoma Spheroid Growth and Metastasis Independent of the Ambient Gas Composition. *Cancers* 12, 2570, doi:10.3390/cancers12092570 (2020).
- 97 Privat-Maldonado, A., Gorbanev, Y., Dewilde, S., Smits, E. & Bogaerts, A. Reduction of Human Glioblastoma Spheroids Using Cold Atmospheric Plasma: The Combined Effect of Short- and Long-Lived Reactive Species. *Cancers* 10, 394 (2018).
- 98 Friedrich, J., Ebner, R. & Kunz-Schughart, L. A. Experimental anti-tumor therapy in 3-D: spheroids—old hat or new challenge? *International journal of radiation biology* 83, 849-871 (2007).
- 99 Kunz-Schughart, L. A., Freyer, J. P., Hofstaedter, F. & Ebner, R. The use of 3-D cultures for high-throughput screening: the multicellular spheroid model. *Journal of biomolecular screening* 9, 273-285 (2004).
- 100 Sutherland, R. M., McCredie, J. A. & Inch, W. R. Growth of multicell spheroids in tissue culture as a model of nodular carcinomas. *Journal of the National Cancer Institute* 46, 113-120 (1971).
- 101 Lokman, N. A., Elder, A. S. F., Ricciardelli, C. & Oehler, M. K. Chick Chorioallantoic Membrane (CAM) Assay as an In Vivo Model to Study the Effect of Newly Identified Molecules on Ovarian Cancer Invasion and Metastasis. *International Journal of Molecular Sciences* 13, 9959-9970 (2012).
- 102 Kue, C. S., Tan, K. Y., Lam, M. L. & Lee, H. B. Chick embryo chorioallantoic membrane (CAM): an alternative predictive model in acute toxicological studies for anti-cancer drugs. *Experimental animals* 64, 129-138, doi:10.1538/expanim.14-0059 (2015).
- 103 Ardelean, S., Feflea, S., Ionescu, D., Năstase, V. & Dehelean, C. A. Toxicologic screening of some surfactants using modern in vivo bioassays. *Revista medico-chirurgicala a Societatii de Medici si Naturalisti din Iasi* 115, 251-258 (2011).
- 104 Saw, C. L., Heng, P. W. & Liew, C. V. Chick chorioallantoic membrane as an in situ biological membrane for pharmaceutical formulation development: a review. *Drug development and industrial pharmacy* 34, 1168-1177 (2008).
- 105 Yan, X., Piferski, C. & Nitka, S. Evaluation of the Hen's Egg Test—Chorioallantoic Membrane (CAM) Method in Prediction of the Eye Irritation Potential Formulated Personal Wash Products. *Cutaneous and ocular toxicology* 26, 25-36 (2007).
- 106 Barnes, L. A. *et al.* Mechanical Forces in Cutaneous Wound Healing: Emerging Therapies to Minimize Scar Formation. *Advances in wound care* 7, 47-56, doi:10.1089/wound.2016.0709 (2018).
- 107 Sun, Z., Guo, S. S. & Fässler, R. Integrin-mediated mechanotransduction. *The Journal of cell biology* 215, 445-456, doi:10.1083/jcb.201609037 (2016).

- 108 Zhou, D. W. *et al.* Force-FAK signaling coupling at individual focal adhesions
coordinates mechanosensing and microtissue repair. *Nature Communications*
12, 2359, doi:10.1038/s41467-021-22602-5 (2021).
- 109 Wong, V. W. *et al.* Loss of keratinocyte focal adhesion kinase stimulates
dermal proteolysis through upregulation of MMP9 in wound healing. *Annals of*
surgery 260, 1138-1146, doi:10.1097/sla.000000000000219 (2014).
- 110 Chan, P. Y., Kanner, S. B., Whitney, G. & Aruffo, A. A transmembrane-
anchored chimeric focal adhesion kinase is constitutively activated and
phosphorylated at tyrosine residues identical to pp125FAK. *Journal of*
Biological Chemistry 269, 20567-20574, doi:[https://doi.org/10.1016/S0021-
9258\(17\)32031-8](https://doi.org/10.1016/S0021-9258(17)32031-8) (1994).
- 111 Schlaepfer, D. D., Hanks, S. K., Hunter, T. & van der Geer, P. Integrin-
mediated signal transduction linked to Ras pathway by GRB2 binding to focal
adhesion kinase. *Nature* 372, 786-791, doi:10.1038/372786a0 (1994).
- 112 Schaller, M. D. *et al.* Autophosphorylation of the focal adhesion kinase,
pp125FAK, directs SH2-dependent binding of pp60src. *Molecular and cellular*
biology 14, 1680-1688, doi:10.1128/mcb.14.3.1680-1688.1994 (1994).
- 113 Mitra, S. K. *et al.* Intrinsic FAK activity and Y925 phosphorylation facilitate an
angiogenic switch in tumors. *Oncogene* 25, 5969-5984,
doi:10.1038/sj.onc.1209588 (2006).
- 114 Kolkova, K., Novitskaya, V., Pedersen, N., Berezin, V. & Bock, E. Neural cell
adhesion molecule-stimulated neurite outgrowth depends on activation of
protein kinase C and the Ras-mitogen-activated protein kinase pathway. *The*
Journal of neuroscience : the official journal of the Society for Neuroscience
20, 2238-2246, doi:10.1523/jneurosci.20-06-02238.2000 (2000).
- 115 Turner, C. E. Paxillin interactions. *Journal of cell science* 113 Pt 23, 4139-4140
(2000).
- 116 Klemke, R. L. *et al.* CAS/Crk coupling serves as a "molecular switch" for
induction of cell migration. *The Journal of cell biology* 140, 961-972,
doi:10.1083/jcb.140.4.961 (1998).
- 117 Grädler, U. *et al.* Fragment-based discovery of focal adhesion kinase inhibitors.
Bioorganic & medicinal chemistry letters 23, 5401-5409 (2013).
- 118 Takai, E. *et al.* Chemical modification of amino acids by atmospheric-pressure
cold plasma in aqueous solution. *Journal of Physics D: Applied Physics* 47,
285403 (2014).
- 119 Vermeylen, S. *et al.* Cold atmospheric plasma treatment of melanoma and
glioblastoma cancer cells. *Plasma Processes and Polymers* 13, 1195-1205
(2016).
- 120 Gjika, E. *et al.* Combination therapy of cold atmospheric plasma (CAP) with
temozolomide in the treatment of U87MG glioblastoma cells. *Scientific Reports*
10, 1-13 (2020).
- 121 Hänsch, M. A., Mann, M., Weltmann, K.-D. & Von Woedtke, T. Analysis of
antibacterial efficacy of plasma-treated sodium chloride solutions. *Journal of*
Physics D: Applied Physics 48, 454001 (2015).
- 122 Ke, Z., Chen, Z. & Huang, Q. Effect of chloride on bacterial inactivation by
discharge plasma at the gas-solution interface: Potentiation or attenuation?

- Plasma Processes and Polymers* 15, 1700153, doi:<https://doi.org/10.1002/ppap.201700153> (2018).
- 123 Wiegand, C. Potential of cold atmospheric pressure plasma (CAPP) in wound management.
- 124 Abbi, S. *et al.* Regulation of focal adhesion kinase by a novel protein inhibitor FIP200. *Molecular biology of the cell* 13, 3178-3191, doi:10.1091/mbc.e02-05-0295 (2002).
- 125 Lietha, D. *et al.* Structural basis for the autoinhibition of focal adhesion kinase. *Cell* 129, 1177-1187 (2007).
- 126 Calalb, M. B., Polte, T. R. & Hanks, S. K. Tyrosine phosphorylation of focal adhesion kinase at sites in the catalytic domain regulates kinase activity: a role for Src family kinases. *Molecular and cellular biology* 15, 954-963 (1995).
- 127 Gebäck, T., Schulz, M. M. P., Koumoutsakos, P. & Detmar, M. TScratch: A novel and simple software tool for automated analysis of monolayer wound healing assays: Short Technical Reports. *Biotechniques* 46, 265-274 (2009).
- 128 Berendsen, H., Postma, J., Van Gunsteren, W. & Hermans, J. In Intermolecular forces 331–342. *Dordrecht: Reidel. B. Pullman, ed* (1981).
- 129 Hermans, J., Berendsen, H. J., Van Gunsteren, W. F. & Postma, J. P. A consistent empirical potential for water–protein interactions. *Biopolymers: Original Research on Biomolecules* 23, 1513-1518 (1984).
- 130 Bussi, G., Donadio, D. & Parrinello, M. Canonical sampling through velocity rescaling. *The Journal of chemical physics* 126, 014101 (2007).
- 131 Parrinello, M. Polymorphic Transitions in Single Crystals : A New Molecular Dynamics Method. *Journal of Applied Physics* 52, 7812-7190 (1981).
- 132 Tironi, I. G., Sperb, R., Smith, P. E. & van Gunsteren, W. F. A generalized reaction field method for molecular dynamics simulations. *The Journal of chemical physics* 102, 5451-5459 (1995).
- 133 Zhou, R. *et al.* Interaction of atmospheric-pressure air microplasmas with amino acids as fundamental processes in aqueous solution. *PLoS one* 11, e0155584 (2016).
- 134 Abraham, M. J. *et al.* GROMACS: High performance molecular simulations through multi-level parallelism from laptops to supercomputers. *SoftwareX* 1, 19-25 (2015).
- 135 Schmid, N. *et al.* Definition and testing of the GROMOS force-field versions 54A7 and 54B7. *European biophysics journal* 40, 843-856 (2011).
- 136 Petrov, D., Margreitter, C., Grandits, M., Oostenbrink, C. & Zagrovic, B. A systematic framework for molecular dynamics simulations of protein post-translational modifications. *PLoS Comput Biol* 9, e1003154 (2013).
- 137 Ben Mahdi, M. H., Andrieu, V. & Pasquier, C. Focal adhesion kinase regulation by oxidative stress in different cell types. *IUBMB Life* 50, 291-299, doi:10.1080/713803721 (2000).
- 138 Vepa, S. *et al.* Hydrogen peroxide stimulates tyrosine phosphorylation of focal adhesion kinase in vascular endothelial cells. *Am J Physiol* 277, L150-158, doi:10.1152/ajplung.1999.277.1.L150 (1999).

- 139 Soman, N. R. *et al.* Molecularly targeted nanocarriers deliver the cytolytic peptide melittin specifically to tumor cells in mice, reducing tumor growth. *The Journal of clinical investigation* 119, 2830-2842 (2009).
- 140 Zarrinnahad, H. *et al.* Apoptotic Effect of Melittin Purified from Iranian Honey Bee Venom on Human Cervical Cancer HeLa Cell Line. *International journal of peptide research and therapeutics* 24, 563-570 (2018).
- 141 Jo, M. *et al.* Anti-cancer effect of bee venom toxin and melittin in ovarian cancer cells through induction of death receptors and inhibition of JAK2/STAT3 pathway. *Toxicology and applied pharmacology* 258, 72-81 (2012).
- 142 Moon, D.-O. *et al.* Melittin induces Bcl-2 and caspase-3-dependent apoptosis through downregulation of Akt phosphorylation in human leukemic U937 cells. *Toxicicon* 51, 112-120 (2008).
- 143 Park, M. H. *et al.* Anti-cancer effect of bee venom in prostate cancer cells through activation of caspase pathway via inactivation of NF- κ B. *The Prostate* 71, 801-812 (2011).
- 144 Zhang, S. F. & Chen, Z. Melittin exerts an antitumor effect on nonsmall cell lung cancer cells. *Molecular medicine reports* 16, 3581-3586, doi:10.3892/mmr.2017.6970 (2017).
- 145 Maher, S. & McClean, S. Melittin exhibits necrotic cytotoxicity in gastrointestinal cells which is attenuated by cholesterol. *Biochemical pharmacology* 75, 1104-1114, doi:10.1016/j.bcp.2007.10.029 (2008).
- 146 Gajski, G. & Garaj-Vrhovac, V. Melittin: a lytic peptide with anticancer properties. *Environmental toxicology and pharmacology* 36, 697-705, doi:10.1016/j.etap.2013.06.009 (2013).
- 147 Suttman, H. *et al.* Antimicrobial peptides of the Cecropin-family show potent antitumor activity against bladder cancer cells. *BMC urology* 8, 5, doi:10.1186/1471-2490-8-5 (2008).
- 148 Soman, N. R. *et al.* Molecularly targeted nanocarriers deliver the cytolytic peptide melittin specifically to tumor cells in mice, reducing tumor growth. *J Clin Invest* 119, 2830-2842, doi:10.1172/jci38842 (2009).
- 149 Pan, H., Soman, N. R., Schlesinger, P. H., Lanza, G. M. & Wickline, S. A. Cytolytic peptide nanoparticles ('NanoBees') for cancer therapy. *Wiley interdisciplinary reviews. Nanomedicine and nanobiotechnology* 3, 318-327, doi:10.1002/wnan.126 (2011).
- 150 Bei, C., Bindu, T., Remant, K. C. & Peisheng, X. Dual secured nano-melittin for the safe and effective eradication of cancer cells. *Journal of materials chemistry. B* 3, 25-29, doi:10.1039/c4tb01401d (2015).
- 151 Furuta, R. *et al.* Intracellular responses to reactive oxygen and nitrogen species, and lipid peroxidation in apoptotic cells cultivated in plasma-activated medium. *Plasma Processes and Polymers*. 14, 1700123, doi:10.1002/ppap.201700123 (2017).
- 152 Irani, S., Shahmirani, Z., Atyabi, S. M. & Mirpoor, S. Induction of growth arrest in colorectal cancer cells by cold plasma and gold nanoparticles. *Archives of medical science : AMS* 11, 1286-1295, doi:10.5114/aoms.2015.48221 (2015).

- 153 Reis, A., Domingues, M. R., Amado, F. M., Ferrer-Correia, A. J. & Domingues, P. Separation of peroxidation products of diacyl-phosphatidylcholines by reversed-phase liquid chromatography-mass spectrometry. *Biomedical chromatography : BMC* 19, 129-137, doi:10.1002/bmc.429 (2005).
- 154 Van Der Spoel, D. *et al.* GROMACS: fast, flexible, and free. *Journal of computational chemistry* 26, 1701-1718, doi:10.1002/jcc.20291 (2005).
- 155 Chiu, S.-W., Pandit, S. A., Scott, H. L. & Jakobsson, E. An Improved United Atom Force Field for Simulation of Mixed Lipid Bilayers. *The Journal of Physical Chemistry B* 113, 2748-2763, doi:10.1021/jp807056c (2009).
- 156 Wong-Ekkabut, J. *et al.* Effect of lipid peroxidation on the properties of lipid bilayers: a molecular dynamics study. *Biophys J* 93, 4225-4236, doi:10.1529/biophysj.107.112565 (2007).
- 157 Martinez, L., Andrade, R., Birgin, E. G. & Martinez, J. M. PACKMOL: a package for building initial configurations for molecular dynamics simulations. *Journal of computational chemistry* 30, 2157-2164, doi:10.1002/jcc.21224 (2009).
- 158 Van der Paal, J., Neyts, E. C., Verlackt, C. C. W. & Bogaerts, A. Effect of lipid peroxidation on membrane permeability of cancer and normal cells subjected to oxidative stress. *Chemical science* 7, 489-498, doi:10.1039/c5sc02311d (2016).
- 159 Hoover, W. G. Canonical dynamics: Equilibrium phase-space distributions. *Physical review. A, General physics* 31, 1695-1697 (1985).
- 160 Essmann, U. A Smooth Particle Mesh Ewald Potential. *J. Chem. Phys.* 103, 8577-8592 (1995).
- 161 Yang, L., Harroun, T. A., Weiss, T. M., Ding, L. & Huang, H. W. Barrel-stave model or toroidal model? A case study on melittin pores. *Biophys J* 81, 1475-1485, doi:10.1016/s0006-3495(01)75802-x (2001).
- 162 Kastner, J. Umbrella sampling. *Wiley Interdisciplinary Reviews: Computational Molecular Science* 1, 932-942, doi:10.1002/wcms.66 (2011).
- 163 Hernandez, J. L. *et al.* Therapeutic targeting of tumor growth and angiogenesis with a novel anti-S100A4 monoclonal antibody. *PloS one* 8, e72480, doi:10.1371/journal.pone.0072480 (2013).
- 164 Reynolds, C. P. & Maurer, B. J. Evaluating response to antineoplastic drug combinations in tissue culture models. *Methods in molecular medicine* 110, 173-183, doi:10.1385/1-59259-869-2:173 (2005).
- 165 Tu, W. C., Wu, C. C., Hsieh, H. L., Chen, C. Y. & Hsu, S. L. Honeybee venom induces calcium-dependent but caspase-independent apoptotic cell death in human melanoma A2058 cells. *Toxicon* 52, 318-329, doi:10.1016/j.toxicon.2008.06.007 (2008).
- 166 Rady, I., Siddiqui, I. A., Rady, M. & Mukhtar, H. Melittin, a major peptide component of bee venom, and its conjugates in cancer therapy. *Cancer letters* 402, 16-31, doi:10.1016/j.canlet.2017.05.010 (2017).
- 167 Lunov, O. *et al.* Chemically different non-thermal plasmas target distinct cell death pathways. *Sci Rep* 7, 600, doi:10.1038/s41598-017-00689-5 (2017).
- 168 Yang, W. S. & Stockwell, B. R. Ferroptosis: Death by Lipid Peroxidation. *Trends in cell biology* 26, 165-176, doi:10.1016/j.tcb.2015.10.014 (2016).

- 169 Uchida, K. *et al.* Activation of stress signaling pathways by the end product of lipid peroxidation. 4-hydroxy-2-nonenal is a potential inducer of intracellular peroxide production. *The Journal of biological chemistry* 274, 2234-2242 (1999).
- 170 Boys, B. L., Kuprowski, M. C., Noël, J. J. & Konermann, L. Protein oxidative modifications during electrospray ionization: solution phase electrochemistry or corona discharge-induced radical attack? *Analytical chemistry* 81, 4027-4034 (2009).
- 171 Wong, J. W., Maleknia, S. D. & Downard, K. M. Hydroxyl radical probe of the calmodulin-melittin complex interface by electrospray ionization mass spectrometry. *Journal of the American Society for Mass Spectrometry* 16, 225-233 (2005).
- 172 Lyu, Y., Xiang, N., Zhu, X. & Narsimhan, G. Potential of mean force for insertion of antimicrobial peptide melittin into a pore in mixed DOPC/DOPG lipid bilayer by molecular dynamics simulation. *The Journal of chemical physics* 146, 155101, doi:10.1063/1.4979613 (2017).
- 173 Irudayam, S. J. & Berkowitz, M. L. Binding and reorientation of melittin in a POPC bilayer: Computer simulations. *Biochimica et Biophysica Acta (BBA) - Biomembranes* 1818, 2975-2981, doi:10.1016/j.bbamem.2012.07.026 (2012).
- 174 Leuschner, C. & Hansel, W. Membrane disrupting lytic peptides for cancer treatments. *Current pharmaceutical design* 10, 2299-2310 (2004).
- 175 Hansel, W., Enright, F. & Leuschner, C. Destruction of breast cancers and their metastases by lytic peptide conjugates in vitro and in vivo. *Molecular and cellular endocrinology* 260, 183-189 (2007).
- 176 Zucker, S. N. *et al.* Preferential induction of apoptotic cell death in melanoma cells as compared with normal keratinocytes using a non-thermal plasma torch. *Cancer biology & therapy* 13, 1299-1306 (2012).
- 177 Radi, R., Beckman, J. S., Bush, K. M. & Freeman, B. A. Peroxynitrite-induced membrane lipid peroxidation: the cytotoxic potential of superoxide and nitric oxide. *Archives of biochemistry and biophysics* 288, 481-487 (1991).
- 178 Rawla, P., Sunkara, T. & Gaduputi, V. Epidemiology of Pancreatic Cancer: Global Trends, Etiology and Risk Factors. *World J Oncol* 10, 10-27, doi:10.14740/wjon1166 (2019).
- 179 Holohan, C., Van Schaeybroeck, S., Longley, D. B. & Johnston, P. G. Cancer drug resistance: an evolving paradigm. *Nature reviews. Cancer* 13, 714-726, doi:10.1038/nrc3599 (2013).
- 180 Hassannia, B., Vandenabeele, P. & Vanden Berghe, T. Targeting Ferroptosis to Iron Out Cancer. *Cancer cell* 35, 830-849, doi:10.1016/j.ccell.2019.04.002 (2019).
- 181 Jiang, X., Stockwell, B. R. & Conrad, M. Ferroptosis: mechanisms, biology and role in disease. *Nature Reviews Molecular Cell Biology* 22, 266-282 (2021).
- 182 Shibata, Y., Yasui, H., Higashikawa, K., Miyamoto, N. & Kuge, Y. Erastin, a ferroptosis-inducing agent, sensitized cancer cells to X-ray irradiation via glutathione starvation in vitro and in vivo. *PloS one* 14, e0225931 (2019).
- 183 Privat-Maldonado, A. *et al.* ROS from physical plasmas: Redox chemistry for biomedical therapy. *Oxidative Medicine and Cellular Longevity* 2019 (2019).

- 184 Furuta, T., Shi, L. & Toyokuni, S. Non-thermal plasma as a simple ferroptosis inducer in cancer cells: a 4 possible role of ferritin 5. *Pathol Int (Letter to the Editor)* 2, 3 (2018).
- 185 Furuta, R. *et al.* Intracellular responses to reactive oxygen and nitrogen species, and lipid peroxidation in apoptotic cells cultivated in plasma-activated medium. *Plasma Processes and Polymers* 14, 1700123 (2017).
- 186 Morfill, G. E., Kong, M. G. & Zimmermann, J. L. FOCUS ON PLASMA MEDICINE. *New Journal of Physics* 11, 115011, doi:10.1088/1367-2630/11/11/115011 (2009).
- 187 Magtanong, L., Ko, P. & Dixon, S. Emerging roles for lipids in non-apoptotic cell death. *Cell Death & Differentiation* 23, 1099-1109 (2016).
- 188 Adachi, T. *et al.* Iron stimulates plasma-activated medium-induced A549 cell injury. *Scientific reports* 6, 20928 (2016).
- 189 Chen, Z., Cheng, X., Lin, L. & Keidar, M. Cold atmospheric plasma discharged in water and its potential use in cancer therapy. *Journal of Physics D: Applied Physics* 50, 015208 (2016).
- 190 Shaw, P. *et al.* Bacterial inactivation by plasma treated water enhanced by reactive nitrogen species. *Scientific reports* 8, 1-10 (2018).
- 191 Abraham, M. J. *et al.* GROMACS: High performance molecular simulations through multi-level parallelism from laptops to supercomputers. *SoftwareX* 1-2, 19-25, doi:10.1016/j.softx.2015.06.001 (2015).
- 192 Schmid, N. *et al.* Definition and testing of the GROMOS force-field versions 54A7 and 54B7. *European biophysics journal: EBJ* 40, 843 (2011).
- 193 Scheerer, P. *et al.* Structural basis for catalytic activity and enzyme polymerization of phospholipid hydroperoxide glutathione peroxidase-4 (GPx4). *Biochemistry* 46, 9041-9049 (2007).
- 194 Margreitter, C., Petrov, D. & Zagrovic, B. Vienna-PTM web server: a toolkit for MD simulations of protein post-translational modifications. *Nucleic Acids Research* 41, W422-426 (2013).
- 195 DELANO, W. The PyMOL Molecular Graphics System. <http://pymol.sourceforge.net> (2004).
- 196 Totsuka, K. *et al.* Oxidative stress induces ferroptotic cell death in retinal pigment epithelial cells. *Experimental Eye Research* 181, 316-324 (2019).
- 197 Zarkovic, N., Cipak, A., Jaganjac, M., Borovic, S. & Zarkovic, K. Pathophysiological relevance of aldehydic protein modifications. *Journal of proteomics* 92, 239-247, doi:10.1016/j.jprot.2013.02.004 (2013).
- 198 Eaton, J. K. *et al.* Targeting a therapy-resistant cancer cell state using masked electrophiles as GPX4 inhibitors. *bioRxiv*, 376764 (2018).
- 199 Vanden Berghe, T., Hassannia, B. & Van Coillie, S. Ferroptosis: biological rust of lipid membranes. *Antioxidants and Redox Signaling*.
- 200 Minniti, G., Muni, R., Lanzetta, G., Marchetti, P. & Enrici, R. M. Chemotherapy for glioblastoma: current treatment and future perspectives for cytotoxic and targeted agents. *Anticancer Research* 29, 5171-5184 (2009).
- 201 Lo Dico, A., Martelli, C., Diceglie, C., Lucignani, G. & Ottobrini, L. Hypoxia-inducible factor-1 α activity as a switch for glioblastoma responsiveness to temozolomide. *Frontiers in oncology* 8, 249 (2018).

- 202 Silantsev, A. S. *et al.* Current and future trends on diagnosis and prognosis of
glioblastoma: from molecular biology to proteomics. *Cells* 8, 863 (2019).
- 203 Towner, R. A. *et al.* OKN-007 increases temozolomide (TMZ) sensitivity and
suppresses TMZ-resistant glioblastoma (GBM) tumor growth. *Translational
oncology* 12, 320-335 (2019).
- 204 Sun, Y., Zheng, Y., Wang, C. & Liu, Y. Glutathione depletion induces
ferroptosis, autophagy, and premature cell senescence in retinal pigment
epithelial cells. *Cell Death & Disease* 9, 1-15 (2018).
- 205 Hu, Z. *et al.* A Potential Mechanism of Temozolomide Resistance in Glioma–
Ferroptosis. *Frontiers in Oncology* 10 (2020).
- 206 Dixon, S. J. *et al.* Ferroptosis: an iron-dependent form of nonapoptotic cell
death. *Cell* 149, 1060-1072 (2012).
- 207 Su, L.-J. *et al.* Reactive oxygen species-induced lipid peroxidation in apoptosis,
autophagy, and ferroptosis. *Oxidative medicine and cellular longevity* 2019
(2019).
- 208 Liou, G.-Y. & Storz, P. Reactive oxygen species in cancer. *Free Radic Res* 44,
479-496, doi:10.3109/10715761003667554 (2010).
- 209 Moloney, J. N. & Cotter, T. G. in *Seminars in cell & developmental biology*.
50-64 (Elsevier).
- 210 Takashi, Y. *et al.* Mitochondrial dysfunction promotes aquaporin expression
that controls hydrogen peroxide permeability and ferroptosis. *Free Radical
Biology and Medicine* 161, 60-70 (2020).
- 211 Imai, H., Matsuoka, M., Kumagai, T., Sakamoto, T. & Koumura, T. Lipid
peroxidation-dependent cell death regulated by GPx4 and ferroptosis. *Apoptotic
and Non-apoptotic Cell Death*, 143-170 (2016).
- 212 Yin, H. *et al.* Curcumin sensitizes glioblastoma to temozolomide by
simultaneously generating ROS and disrupting AKT/mTOR signaling. *Oncol
Rep* 32, 1610-1616, doi:10.3892/or.2014.3342 (2014).
- 213 Lee, G. & Han, S. (2018).
- 214 Ribas, V., García-Ruiz, C. & Fernández-Checa, J. C. Glutathione and
mitochondria. *Frontiers in pharmacology* 5, 151 (2014).
- 215 Rocha, C. R. R., Kajitani, G. S., Quinet, A., Fortunato, R. S. & Menck, C. F. M.
NRF2 and glutathione are key resistance mediators to temozolomide in glioma
and melanoma cells. *Oncotarget* 7, 48081 (2016).
- 216 Zhang, L. & Wang, H. FTY720 inhibits the Nrf2/ARE pathway in human
glioblastoma cell lines and sensitizes glioblastoma cells to temozolomide.
Pharmacological Reports 69, 1186-1193 (2017).
- 217 Ye, P. *et al.* Nrf2-and ATF4-dependent upregulation of xCT modulates the
sensitivity of T24 bladder carcinoma cells to proteasome inhibition. *Molecular
and cellular biology* 34, 3421-3434 (2014).
- 218 Bersuker, K. *et al.* The CoQ oxidoreductase FSP1 acts parallel to GPX4 to
inhibit ferroptosis. *Nature* 575, 688-692 (2019).
- 219 Wang, H. *et al.* Characterization of ferroptosis in murine models of
hemochromatosis. *Hepatology* 66, 449-465 (2017).

- 220 Rocha, C. R. R. *et al.* Glutathione depletion sensitizes cisplatin-and
temozolomide-resistant glioma cells in vitro and in vivo. *Cell death & disease*
5, e1505-e1505 (2014).
- 221 Köritzner, J. *et al.* Restoration of sensitivity in chemo—resistant glioma cells by
cold atmospheric plasma. *PloS one* 8, e64498 (2013).
- 222 Privat-Maldonado, A., Gorbanev, Y., Dewilde, S., Smits, E. & Bogaerts, A.
Reduction of human glioblastoma spheroids using cold atmospheric plasma:
The combined effect of short-and long-lived reactive species. *Cancers* 10, 394
(2018).
- 223 Grisetti, E., Merbahi, N. & Golzio, M. Anti-Cancer Potential of Two Plasma-
Activated Liquids: Implication of Long-Lived Reactive Oxygen and Nitrogen
Species. *Cancers* 12, 721 (2020).
- 224 Plewa, J.-M. *et al.* Low-temperature plasma-induced antiproliferative effects on
multi-cellular tumor spheroids. *New Journal of Physics* 16, 043027 (2014).
- 225 Chauvin, J. *et al.* Elucidation of in vitro cellular steps induced by antitumor
treatment with plasma-activated medium. *Scientific reports* 9, 1-11 (2019).
- 226 Hernandez, J. L. *et al.* Therapeutic targeting of tumor growth and angiogenesis
with a novel anti-S100A4 monoclonal antibody. *PloS one* 8, e72480 (2013).
- 227 Reynolds, C. P. & Maurer, B. J. Evaluating response to antineoplastic drug
combinations in tissue culture models. *Chemosensitivity*, 173-183 (2005).
- 228 Longati, P. *et al.* 3D pancreatic carcinoma spheroids induce a matrix-rich,
chemoresistant phenotype offering a better model for drug testing. *BMC cancer*
13, 1-13 (2013).
- 229 Golda, J. *et al.* Concepts and characteristics of the ‘COST Reference
Microplasma Jet’. *Journal of Physics D: Applied Physics* 49, 084003 (2016).
- 230 Gorbanev, Y., Van der Paal, J., Van Boxem, W., Dewilde, S. & Bogaerts, A.
Reaction of chloride anion with atomic oxygen in aqueous solutions: can cold
plasma help in chemistry research? *Physical Chemistry Chemical Physics* 21,
4117-4121, doi:10.1039/C8CP07550F (2019).
- 231 Hefny, M. M., Pattyn, C., Lukes, P. & Benedikt, J. Atmospheric plasma
generates oxygen atoms as oxidizing species in aqueous solutions. *Journal of
Physics D: Applied Physics* 49, 404002 (2016).
- 232 Van Boxem, W. *et al.* Anti-cancer capacity of plasma-treated PBS: effect of
chemical composition on cancer cell cytotoxicity. *Scientific reports* 7, 1-15
(2017).
- 233 Chung, T.-H. *et al.* Cell electroporation enhancement by non-thermal-
plasma-treated pbs. *Cancers* 12, 219 (2020).
- 234 Melamed, J. R. *et al.* Investigating the role of Hedgehog/GLI1 signaling in
glioblastoma cell response to temozolomide. *Oncotarget* 9, 27000 (2018).
- 235 Zhu, Z. *et al.* Glutathione reductase mediates drug resistance in glioblastoma
cells by regulating redox homeostasis. *Journal of neurochemistry* 144, 93-104,
doi:10.1111/jnc.14250 (2018).
- 236 Bao, S. *et al.* Glioma stem cells promote radioresistance by preferential
activation of the DNA damage response. *nature* 444, 756-760 (2006).

- 237 Lathia, J. D., Mack, S. C., Mulkearns-Hubert, E. E., Valentim, C. L. & Rich, J. N. Cancer stem cells in glioblastoma. *Genes & development* 29, 1203-1217 (2015).
- 238 Hassannia, B., Vandenabeele, P. & Berghe, T. V. Targeting ferroptosis to iron out cancer. *Cancer cell* 35, 830-849 (2019).
- 239 Lunov, O. *et al.* Chemically different non-thermal plasmas target distinct cell death pathways. *Sci Rep* 7, 600, doi:10.1038/s41598-017-00689-5 (2017).
- 240 Judée, F. *et al.* Short and long time effects of low temperature Plasma Activated Media on 3D multicellular tumor spheroids. *Sci Rep* 6, 21421, doi:10.1038/srep21421 (2016).
- 241 Griseti, E. *et al.* Pulsed Electric Field Treatment Enhances the Cytotoxicity of Plasma-Activated Liquids in a Three-Dimensional Human Colorectal Cancer Cell Model. *Scientific Reports* 9, 7583, doi:10.1038/s41598-019-44087-5 (2019).
- 242 Freund, E. *et al.* Physical plasma-treated saline promotes an immunogenic phenotype in CT26 colon cancer cells in vitro and in vivo. *Scientific Reports* 9, 634, doi:10.1038/s41598-018-37169-3 (2019).
- 243 Son, B. *et al.* The role of tumor microenvironment in therapeutic resistance. *Oncotarget* 8, 3933-3945, doi:10.18632/oncotarget.13907 (2017).
- 244 Friedrich, J., Seidel, C., Ebner, R. & Kunz-Schughart, L. A. Spheroid-based drug screen: considerations and practical approach. *Nature protocols* 4, 309-324, doi:10.1038/nprot.2008.226 (2009).
- 245 Bauer, G. The synergistic effect between hydrogen peroxide and nitrite, two long-lived molecular species from cold atmospheric plasma, triggers tumor cells to induce their own cell death. *Redox biology* 26, 101291, doi:10.1016/j.redox.2019.101291 (2019).
- 246 Lin, L.-S. *et al.* Cooperation of endogenous and exogenous reactive oxygen species induced by zinc peroxide nanoparticles to enhance oxidative stress-based cancer therapy. *Theranostics* 9, 7200-7209, doi:10.7150/thno.39831 (2019).
- 247 Oliva, C. R., Moellering, D. R., Gillespie, G. Y. & Griguer, C. E. Acquisition of chemoresistance in gliomas is associated with increased mitochondrial coupling and decreased ROS production. *PLoS One* 6, e24665, doi:10.1371/journal.pone.0024665 (2011).
- 248 Yin, H. *et al.* Curcumin sensitizes glioblastoma to temozolomide by simultaneously generating ROS and disrupting AKT/mTOR signaling. *Oncology reports* 32, 1610-1616 (2014).
- 249 Liu, D. S. *et al.* Inhibiting the system x(C)(-)/glutathione axis selectively targets cancers with mutant-p53 accumulation. *Nat Commun* 8, 14844-14844, doi:10.1038/ncomms14844 (2017).

